Development of Magnetic Resonance Spectroscopic Imaging Methods to Assess Tumour Metabolism

Felix Karl Kreis

Cancer Research UK Cambridge Institute.

University of Cambridge.

Clare College, Cambridge.

This dissertation is submitted for the degree of

Doctor of Philosophy

July 2019.

Für meine lieben Eltern.

Declaration

This dissertation is the result of my own work and includes nothing which is the outcome of work done in collaboration except as declared in the Preface and specified in the text.

It is not substantially the same as any that I have submitted, or, is being concurrently submitted for a degree or diploma or other qualification at the University of Cambridge or any other University or similar institution except as declared in the Preface and specified in the text. I further state that no substantial part of my dissertation has already been submitted, or, is being concurrently submitted for any such degree, diploma or other qualification at the University of Cambridge or any other University or similar institution except as declared in the Preface and specified in the text.

This dissertation contains less than 60,000 words including appendices, bibliography, footnotes, tables and equations.

Felix Karl Kreis

July 2019

Summary

DEVELOPMENT OF MAGNETIC RESONANCE SPECTROSCOPIC IMAGING METHODS TO ASSESS TUMOUR METABOLISM

Felix Karl Kreis

Proton detection of hyperpolarized low gamma nuclei. Hyperpolarized molecules labelled with low gamma nuclei such as ^{15}N and ^{13}C have been proposed as magnetic resonance spectroscopic imaging (MRSI) agents for investigating metabolism, perfusion and pH in tumours. However, the sensitivity of direct detection is limited by the low gyromagnetic ratios of these nuclei. Sensitivity can be increased by transferring the hyperpolarization to spin coupled protons provided that there is not significant polarization loss during the transfer. To exploit both the slow relaxation offered by storing the hyperpolarization in the low gamma nucleus and the higher sensitivity of ^{1}H detection, polarization transfer pulse sequences for full and partial transfer of polarization were developed. The possible sensitivity improvement with those MRSI pulse sequences was evaluated in experiments and simulations using hyperpolarized [1-^{13}C]pyruvate, [2-^{13}C]pyruvate, [1-^{13}C]lactate and [$^{15}N_2$]urea.

Glycolytic flux measurements *in vivo* using ^{2}H magnetic resonance spectroscopic imaging. Tumour cells frequently show high rates of aerobic glycolysis, which provides the glycolytic intermediates needed for the increased biosynthetic demands of rapid cell growth and proliferation. These high rates of glycolysis have enabled disease detection and treatment response monitoring using Positron Emission Tomography measurements of 2-([^{18}F]fluoro)-2-deoxy-D-glucose uptake (FDG-PET) and ^{13}C magnetic resonance spectroscopic imaging of hyperpolarized [1-^{13}C]pyruvate metabolism. However, neither of these techniques allows quantitative mapping of metabolic fluxes. A fast 3D deuterium MRSI sequence for dynamic imaging of [6,6'-$^{2}H_2$]glucose metabolism was developed and used to map glycolytic flux in a murine tumour model, demonstrating heterogeneity in glycolytic rate an early decrease following treatment.

Acknowledgements

I am very grateful for the guidance of Prof. Kevin Brindle. He has given the most profound input for this thesis. Besides his scientific support, I am thankful for his mentorship and the unique opportunity I have been given by becoming a member of his research group.

I thank Dr Alan Wright for his superb supervision and mentorship. It is due to him that I found my way into these demanding projects.

I want to express gratitude for my generous funding sources, the European Union's Horizon 2020 initial training network EUROPOL and CRUK.

I would like to express my special appreciation and thanks to my external collaborators. Prof. Malcom Levitt gave the initial impetus for the polarization transfer project and provided essential support. Dr Rachel Katz-Brull shared the protocol for the hyperpolarization of [$^{15}N_2$]urea. Dr Rolf Schulte hosted me in his research group in Munich. Mohammed Albannay visited Cambridge and shared his knowledge about RF coils, and of course, there were all the other brilliant colleagues from the Marie-Curie initial training network who made going to conferences fun. I'm grateful to be part of this scientific community.

Dr De-en Hu did all the mice work and provided essential knowledge for the deuterium study which is very much appreciated, I could not have done this project without him.

Drs Madhu Basetti and Dom McIntyre provided great support for the MR machines.

Vencel Somai was always available for helpful discussions on tricky MR physics. I am looking forward to further collaborate with him. Sarah McGuire, Lynn Asante-Asare, Richard Hesketh, Friederike Hesse, Kerstin Timm and Maria Fala helped with culturing cells. Drs Franz Schilling, Adam Gaunt, Tian Cheng and Irene Marco-Rius are great physicists and shared their knowledge and free time with me. Dr Arnaud Comment gave very useful input as a result of the first-year viva. These are just a few of the people from the Brindle lab who helped me over the years. I feel very grateful for having them around and hope to stay in touch.

Finally, I want to thank my friends and family for always being there for me. Particularly my parents Barbara and Wulff and my sister Eva.

But most of all, thank you Karolina for riding this roller coaster with me.

List of publications

Material in this thesis is published or being prepared for publication in the following papers:

1. Wang J*, **Kreis F***, Wright AJ, Hesketh RL, Levitt MH, Brindle KM. Dynamic ^{1}H imaging of hyperpolarized [1-^{13}C]lactate in vivo using a reverse INEPT experiment. *Magn Reson Med.* 2018;70:741-747. ***contributed equally**

2. **Kreis F**, Wright AJ, Katz-Brull R, Brindle KM. Increasing the sensitivity of hyperpolarized [$^{15}N_2$]urea detection by serial transfer of polarization to spin-coupled protons. *Magn Reson Med.* 2019; under review.

3. **Kreis F**, Wright AJ, Hesse F, Fala M, Hu D, Brindle KM. Measuring tumor glycolytic flux in vivo using fast deuterium magnetic resonance imaging. *Radiology* 2019; in press.

During my PhD I also co-authored the following papers which are not presented in this thesis:

4. Mair R, Wright AJ, Ros S, Hu D, Booth T, **Kreis F**, Rao J, Watts C, Brindle KM. Metabolic imaging detects low levels of glycolytic activity that vary with levels of C-MyC expression in patient-derived xenograft models of glioblastoma. *Cancer Res*. 2018;78(18):5408-5418.

5. Marco-Rius I, Cheng T, Gaunt AP, Patel S, **Kreis F**, Capozzi A, Wright AJ, Brindle KM, Ouari O, Comment A. Photogenerated Radical in Phenylglyoxylic Acid for in Vivo Hyperpolarized 13C MR with Photosensitive Metabolic Substrates. *Journal of the American Chemical Society*. 2018:14455-14463.

6. Shishmarev D, Kuchel PW, Pagès G, Wright AJ, Hesketh RL, **Kreis F**, Brindle KM. Glyoxalase activity in human erythrocytes and mouse lymphoma, liver and brain probed with hyperpolarized 13C-methylglyoxal. *Commun Biol*. 2018;1:232.

Contents

List of figures

List of tables

List of main abbreviations

B_0	Amplitude of static (polarizing) field
B_1	Amplitude of excitation (radio frequency) field
BINEPT	B_1-insensitive nuclear enhancement through polarization transfer
BIR4	B_1-insensitive rotation induced by 4 adiabatic half passage pulses
CSI	Chemical shift imaging
DCA	Dichloroacetate
DMI	Deuterium metabolic imaging
(d)DNP	(dissolution) Dynamic nuclear polarization
EPI	Echo planar imaging
FA	Flip angle
FDG	2-[^{18}F]fluoro-2-deoxy-D-glucose
γ	Gyromagnetic ratio
H or $\widehat{\mathrm{H}}$	Hamiltonian operator
HINDER	Hyperpolarized insensitive nucleus delivers enhancement repeatedly
I (spins)	Insensitive spins
I	Spin quantum number
INEPT	Insensitive nuclei enhanced by polarization transfer
IRRUPT	Imperfection robust partial transfer
J	Spin-spin coupling constant
LDH	Lactate dehydrogenase
M or $\overrightarrow{\mathrm{M}}$	Magnetization
MR(S)I	Magnetic resonance (spectroscopic) imaging
NMR	Nuclear magnetic resonance
P	Polarization
PET	Positron emission tomography
ppm	Parts per million
RF	Radio frequency
S (spins)	Sensitive spins
SNR	Signal-to-noise ratio
T	Tesla
T_1	Spin-lattice relaxation time
T_2	Transversal spin relaxation time
TCA	Tricarboxylic acid

TR	Repetition time
ρ or $\hat{\rho}$	Density operator
σ	Chemical shift

Chapter 1 Introduction

Currently the success of treatment in patients with solid tumours is determined by a measurement of tumour size[1]. Typically, size is calculated from diameters measured in images acquired with conventional Magnetic Resonance Imaging (MRI) or Computer Tomography (CT) scans. This is questionable because it is known that it can take several weeks or even months until a successful treatment leads to a reduction in tumour volume[2–4], while other treatment induced changes in the tumour, such as alterations in metabolism, receptor expression or inhibition of proliferation may be manifest much earlier[4]. The long period of treatment with no feedback about response is particularly problematic because tumours are genetically and phenotypically different[5] and therefore can react differently to the same treatment[6]. In the case of an ineffective treatment valuable time may be lost. Since it is usually not possible to assess a tumour's complete geno-and phenotype in advance, and start the ideal treatment right from the start, it is essential to shorten the period of "blind" treatment. With metabolic imaging the effects of treatment can become visible much earlier than with conventional anatomical imaging with MRI or CT.

1.1 Metabolic imaging in cancer

The most characteristic aspect of the metabolism of cancer cells is their reliance on aerobic glycolysis rather than oxidative phosphorylation under normoxic conditions[7,8]. This was first described by Otto Warburg[7–9]. Aerobic glycolysis is inefficient for the production of energy in the form of adenosine triphosphate (ATP) but is an important source of biosynthetic intermediates, providing metabolites for subsidiary pathways, for example metabolites for protein and DNA synthesis as well as NADPH, via the pentose phosphate pathway, for lipid synthesis. Cancer cells need a good supply of glucose to satisfy these biosynthetic requirements[8,10]. The shift back from this "Warburg metabolism" to normal metabolism is often associated with a positive treatment response[11].

Glucose uptake can be imaged using the glucose analog, 2-[^{18}F]fluoro-2-deoxy-D-glucose and Positron Emission Tomography (FDG-PET). In this technique the radiolabelled FDG is injected into the patient. When a positron emitted by the ^{18}F nucleus hits an electron, two 511 keV γ photons are created that travel in opposite directions. When two photons are detected by a detector ring around the patient at the same time, the inference is made that FDG is present somewhere along a line between the two detector elements. When enough of these coincidences are recorded, an image mapping the FDG distribution can be calculated by back projection reconstruction. However FDG-PET has limitations: In tissues with a naturally high uptake of glucose, such as in the brain or in tissue immediately adjacent to the bladder, quantification of tumour uptake is difficult[12]. It also has a lower sensitivity for slower growing, metabolically less active tumours, such as prostate, thyroid and neuroendocrine tumours[4]. Another big disadvantage, especially when repeated acquisitions are required, is the use of ionizing radiation. Repeated exposure to this radiation increases the probability of DNA damage that could cause mutations leading to cancer.

In 2003, Dynamic Nuclear Polarization MRI (DNP-MRI) was introduced[13] and was quickly implemented as a promising magnetic resonance based method that allows mapping the distribution of ^{13}C-labelled substrates and their metabolic products (Figure 1-1) *in vivo*[14–16]. Ten years later, this method was demonstrated in clinical trials[17]. The technique could potentially overcome some of the shortcomings of FDG-PET. In DNP-MRI the nuclear spins in a ^{13}C-labelled substrate are polarized externally and the labelled substrate is then injected into the patient (the technique is not restricted to ^{13}C, however ^{13}C is the most commonly used nucleus). The polarization, and therefore the available signal from the labelled substrate, is orders of magnitude greater than at thermal equilibrium and can be detected using spectrally resolved imaging pulse sequences. In preclinical[18–21] and clinical[22] studies it has been shown, that this technique can monitor treatment response in tumours. This approach, however, is still in its infancy and there are a lot of problems. One of them is that it detects less sensitive nuclei, such ^{13}C or ^{15}N, instead of protons, as in conventional MRI. This will be discussed within this thesis where the development of methods that enable proton observed ^{13}C (chapter 2 and 5) and ^{15}N (chapter 4) DNP-NMR spectroscopy and spectroscopic imaging will be presented, which can increase the sensitivity of DNP-MRI still further.

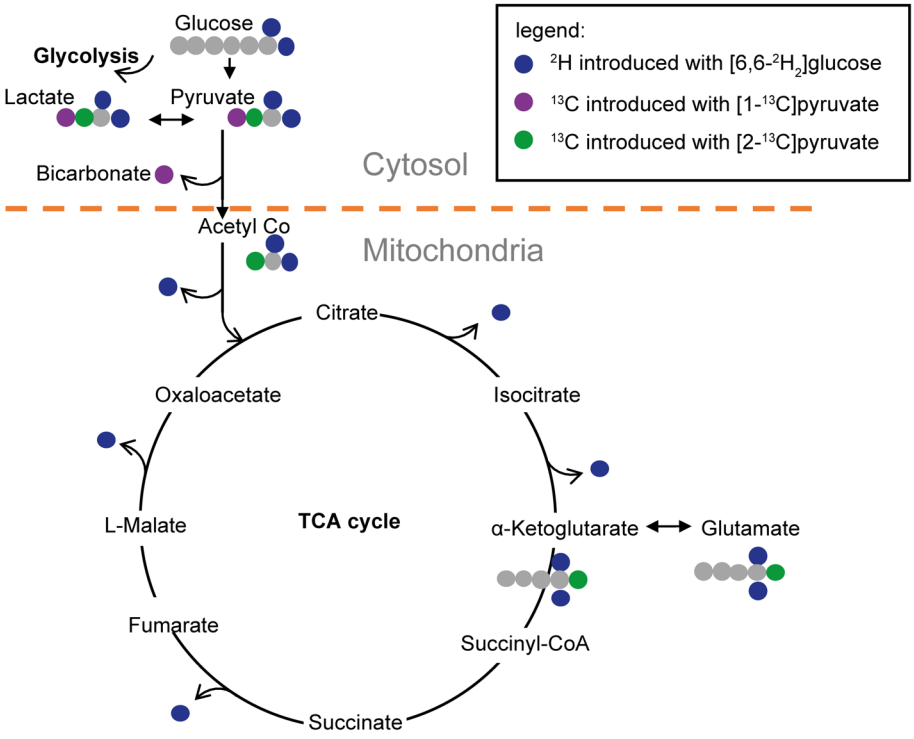

Figure 1-1. When undergoing cellular respiration, isotope labels are enzymatically removed from the introduced substrate molecule or its downstream metabolites. Deuterons are enzymatically removed from [6,6'-$^{2}H_2$]glucose during the indicated steps by the following enzymes: Citrate synthetase[23], aconitase[24], isocitrate dehydrogenase[25], succinate dehydrogenase[26] and malate dehydrogenase[27]. The cleaved off deuterons end up in semi-heavy water (HDO). When [1-^{13}C]pyruvate is used, [1-^{13}C]lactate and [^{13}C]bicarbonate and other (not shown) metabolites can be observed, when [2-^{13}C]pyruvate is used [2-^{13}C]lactate, [5-^{13}C]glutamate and other (not shown) metabolites can be observed [28].

In recent years, parallel to the development of DNP-NMR and MRI, other exciting technologies to monitor treatment response have been proposed. Most noteworthy is the investigation of circulating tumour DNA[29] from liquid biopsies, which could replace imaging based methods[29,30]. Also new MR imaging-based methods have been proposed. The use of fast relaxing tracer molecules or denoising algorithms have enabled metabolic imaging without hyperpolarization. This has been demonstrated with ^{13}C labelled glucose[31] and more noteworthy in 2018 with ^{2}H labelled glucose[23]. In the latter case, in glioma patients, it was shown that oral administration of [6,6′-$^{2}H_2$]glucose resulted in signals from deuterated lactate and glutamate, which report on glycolysis and tricarboxylic acid (TCA) cycle activity

respectively (Figure 1-1). By using natural abundance semi-heavy water as an internal standard, the Deuterium Metabolic Imaging (DMI) ratio maps of the tumours were effectively concentration maps. However, the images presented in this study[23] were static representations of the metabolic state after administration of the deuterated glucose. Chapter 6 of the thesis presents a fast 3D ^{2}H chemical shift imaging (CSI) sequence, that captures dynamically glucose use in a murine tumour model and maps glycolytic flux following a bolus injection of labelled glucose.

The theme of this thesis is the development of magnetic resonance spectroscopic imaging methods to assess tumour metabolism. Chapter 2 introduces proton detection of ^{13}C polarization via spin coupled protons. Chapter 3 describes home-built RF coils used in chapters 4, 5 and 6. Chapters 4 and 5 demonstrate partial polarization transfer imaging in [$^{15}N_2$]urea and [2-^{13}C]pyruvate. In chapter 6 a fast 3D ^{2}H chemical shift imaging (CSI) sequence is used to map glycolytic flux in a murine tumour model.

1.2 Nuclear polarization

1.2.1 MR sensitive nuclei

The basic requirement for every MR experiment is the presence of net magnetization. This net or bulk magnetization is the vector sum of the magnetic moments of the nuclei in the volume of interest. To form a net magnetization vector, nuclei require a non-zero spin. This is the case when the spin orientations of the protons and neutrons making up the nuclei do not cancel each other out. Protons and neutrons build pairs with opposite spin orientations. Therefore, a nucleus with an even number of protons and an even number of neutrons, for example ^{12}C, does not have a nuclear spin, and is therefore NMR invisible. Nuclei with an odd number of protons and/or an odd number of neutrons possess a nuclear spin. In this thesis, ^{2}H,^{13}C,^{15}N and ^{1}H nuclei were studied.

1.2.2 Thermal equilibrium polarization

MR sensitive nuclei *per se* would still not form a net magnetization vector: Each nucleus might have a non-zero spin, however without any preference for the orientation of their associated

magnetic dipole they would be distributed randomly and therefore in any volume containing more than a couple of nuclei the magnetization would average to zero. The situation changes drastically when an external magnetic field B_0 is applied. It is slightly more energetically favourable for the magnetic moments to align parallel, rather than antiparallel, to the external B_0 field. This distribution depends on the temperature T and the gyromagnetic ratio γ in the following way:

$$\frac{N_\uparrow}{N_\downarrow} = e^{-\hbar\gamma B_0/k_b T} \cong 1 - \frac{\hbar\gamma B_0}{k_b T}.$$

$\hbar$ is Planck's constant divided by 2π and k_B is Boltzmann's constant. This population difference ultimately breaks the symmetry and leads to a non-zero net magnetization. At room temperature and 1.5 T around five out of one million protons contribute to the net magnetization. This ratio is called the polarization and is defined by:

$$P = \frac{N_\downarrow - N_\uparrow}{N_\uparrow + N_\downarrow} = \tanh\frac{\hbar\gamma B_0}{2k_B T}. \tag{1.1}$$

The net magnetisation $\vec{M}_0$ and therefore the NMR signal are proportional to this polarization.

1.2.3 Dynamic nuclear polarization

NMR and MRI suffer from a low Signal-to-Noise Ratio (SNR) as a consequence of this intrinsic weak magnetization. Imaging at reasonable spatial and temporal resolutions has so far only been possible using the proton magnetization on water and fat molecules. Here the sheer abundance of water protons in combination with their high gyromagnetic ratio leads to a large net magnetization.

In 2003 it was first shown that the polarization enhanced far beyond thermal equilibrium levels using dynamic nuclear polarization (DNP) could be retained in the liquid state following dissolution of the frozen hyperpolarized substrate in a superheated solvent[13]. The method is based on polarizing nuclear spins in the solid state at low temperatures. To achieve this in a liquid sample, a glass-former (often known as the glassing agent) may be added in order to produce an amorphous solid after freezing. Also, a radical compound is added to the sample to provide unpaired electrons which act as a bath of polarisation that can be transferred to the nuclear spins. The glassing agent prevents a well-defined crystal structure forming and acts to

ensure that the radical compound is randomly distributed about the sample. At high field (approximately 3 T) very low temperatures (~1.2 K), the electron spins, which have a much larger magnetic moment than the nuclear spins, are nearly completely polarized (Figure 1-2).

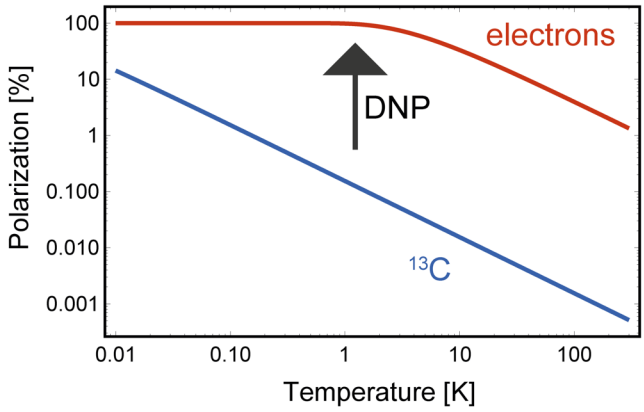

Figure 1-2. Electron and ^{13}C polarizations at different temperatures.

The sample is irradiated at a frequency close to the Electron Spin Resonance (ESR) frequency, which in certain cases causes polarization transfer from the electrons to the nuclei. This transfer is facilitated by a combination of physical effects[32]. While originally the first theoretical proposal[33] and practical implementation[34] of solid state DNP was demonstrated using the Overhauser effect[33], the main contributors in modern dissolution DNP hyperpolarizes are the cross effect, thermal mixing and /or the solid effect[35]. Involving protons as an intermediate carrier of polarization can accelerate the process and improve the maximal achievable polarization[36]. In the context of a clinical DNP experiment, it is necessary before injecting the hyperpolarized substrate into patients, that the potentially toxic radical that provides the free electrons is filtered out[36] or, if a non-persistent radical is used, is annihilated due to the temperature change during the dissolution process[37].

In detail the DNP process works as follows: The sample is brought to liquid helium temperature in a strong magnetic field, in the here presented work a *HyperSense* polarizer with a field strength of 3.35 T was used. Incorporated in the sample are a glassing agent and free radicals, in our case the in the form of OX63 trityl radical. Glassing agents, such as glycerol, are used to prevent crystallisation of the sample. This ensures a uniform distribution of the radicals and the nuclei in the sample. As the electron gyromagnetic ratio is several hundred times higher than the ^{1}H ^{13}C or ^{15}N gyromagnetic ratio, the electrons are almost fully polarized at these low

temperature high magnetic field strength conditions, while the low gamma nuclei are still orders of magnitude away from unity polarization (Equation 1.1 and Figure 1-2).

When the electron Larmor frequency ω_e of two electrons in the sample is separated by the Larmor frequency ω_n of the target nuclei (^{13}C or ^{15}N) and the two electrons are dipolar coupled, a microwave irradiation at $\omega_{MW} = \omega_e \pm \omega_n$ can induce a single quantum (SQ) transition of the electron spin that leads to the polarization of the nuclei (cross effect) through nuclear spin flip-flops[38]. The fast relaxation of the electron compared to the nuclear spin means that the polarisation can build up over time by continuous irradiation of this electronic SQ transition. In order for some of the electrons and nuclei to match the condition $\omega_e \pm \omega_n = \omega_{MW}$ it is necessary to have a broad EPR linewidth. Hovav *et al.* showed that the polarisation achieved on the nuclear spins is directly proportional to the polarisation gradient created in the ESR line between the two electrons involved in the cross effect mechanism[39].

If more electrons per nuclei are involved in the process this hyperpolarization mechanism is called thermal mixing. Thermal mixing requires high concentration of electrons with an inhomogeneously broadened ESR line. Traditionally this mechanism was described with classical thermodynamic methods by introducing the concept of heat loads that are associated with each of the spin baths within the system (i.e. the electron Zeeman spin bath, Hyperfine spin bath and nuclear Zeeman spin bath). However, recently Karabanov *et al*. have introduced a quantum mechanical method for describing the thermal mixing process[40].

A more elaborate mechanism that relies on second order effects is the solid effect: In a scenario where one electron and one nuclear spin Hamiltonian is a sum of the Zeeman interaction and the hyperfine interaction, electron single quantum transitions induced by irradiation at ω_e lead to loss of electron polarization. At the same time, electron-nuclear zero or double quantum coherence transitions are induced at the frequency $\omega_e \pm \omega_n$. Irradiation of one of these can lead to polarization transfer from electrons to nuclei[41].

In all cases, the nuclear hyperpolarization is distributed via the dipolar coupling network to all the nuclei in the sample via a process known as spin diffusion[42]. An effective dipolar coupling network is given by the glassy matrix. In reality the DNP process is driven by a combination of the described effects, whereby thermal mixing is the predominate effect at temperatures below 4.2K [43].

Dissolution DNP has enabled a whole new field of MRI research. Nuclei that conventionally gave very low signal in MRI, because of both low abundance and low polarization, most notably ^{13}C, could now be used for imaging. This is remarkable, because unlike traditional proton MRI, that mostly shows water proton density, T_1 or T_2 dependent contrast, and therefore anatomical features, DNP-MRI can be used to generate images where the signal describes the abundance of a molecule of interest and can be used to monitor its biochemical conversion in real time[44].

1.3 A classical description of MRI

1.3.1 Excitation

Initially the net magnetization $\vec{M}_0$ is aligned with the direction of the polarizing field B_0 ,which defines the z-axis $\vec{e}_z$. To generate precessing magnetization that can be observed as an electromotive force induced in the RF coils, $\vec{M}_0$ must be tipped into the transversal plane. This is achieved with Radio Frequency (RF) pulses oscillating at the Larmor frequency $\omega_L = 2\pi\nu = \gamma B_0$. In a rotating frame where the observer rotates with ω_L around $\vec{e}_z$, the magnetic $\vec{e}_x$ and $\vec{e}_y$ components of these pulses are usually described as the external field $\vec{B}_1(t)$. A constant phase RF pulse with constant amplitude B_1 applied for a time t_p causes the net magnetization to tilt by a flip angle of $\gamma B_1 t_p$ radians into the transversal plane. Such a simple pulse is called hard pulse. Varying the amplitude and phase of $\vec{B}_1(t)$ gives endless possibilities for generating specialized pulses, such as adiabatic pulses. During adiabatic pulses the net magnetization is forced to follow an effective field vector in the rotating frame generated by a frequency sweep of $\vec{B}_1(t)$[45,46]. Combinations of these frequency sweeps can be used to induce arbitrary flip angle over spatial inhomogeneities in the excitation field or off-resonances (Figure 1-3).

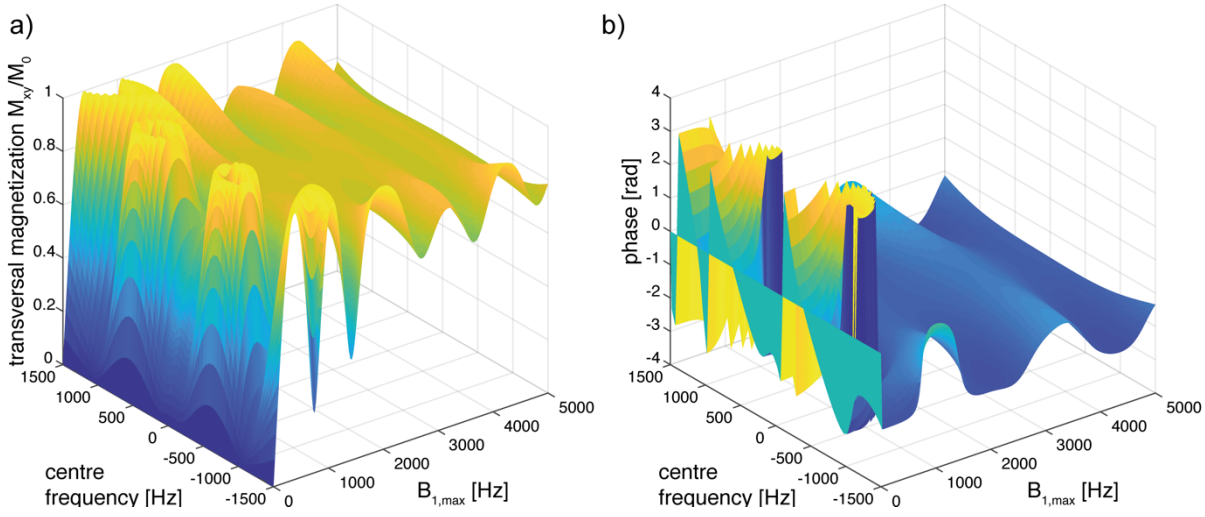

Figure 1-3. Simulated a) excitation and b) phase profile of an B_1-insensitive rotation (BIR4) pulse. The pulse is designed to induce a flip angel of 50° for a range of B_1 and centre frequency offsets. This shaped pulse is used in chapter 6 to induce homogenous excitation over the region of interest *in vivo* with a surface coil. The 2 ms long BIR4 pulse was designed as described in Garwood *et al.* [47].

Spectrally selective pulses use amplitude modulations that result in excitation of only certain resonances while leaving others in the initial state. Sinc modulated pulses have a rectangular spectral excitation profile, gaussian shaped pulses excite a gaussian shaped profile. When such a pulse is applied during a magnetic field gradient, the spectral bandwidth of the pulse can be used to selectively excite a spatial slice orthogonal to the gradient direction[48]. More complicated pulse and gradient designs can be used to selectively excite in the spectral and in the spatial domain at the same time[49]. In hyperpolarized MRI it is often necessary to probe several resonances while storing the hyperpolarization in a different resonance, therefore specialized RF pulses have been developed[50,51].

1.3.2 Relaxation

When perturbed from its thermal equilibrium state $\vec{M}_0 = \vec{e}_z M_0$, relaxation drives the net magnetization back to this state. In the equilibrium state the net magnetization is aligned with the B_0 field (z-axis) and has a polarization described by the Boltzmann distribution (equation 1.1). On a faster timescale, it also drives the transverse magnetization to zero.

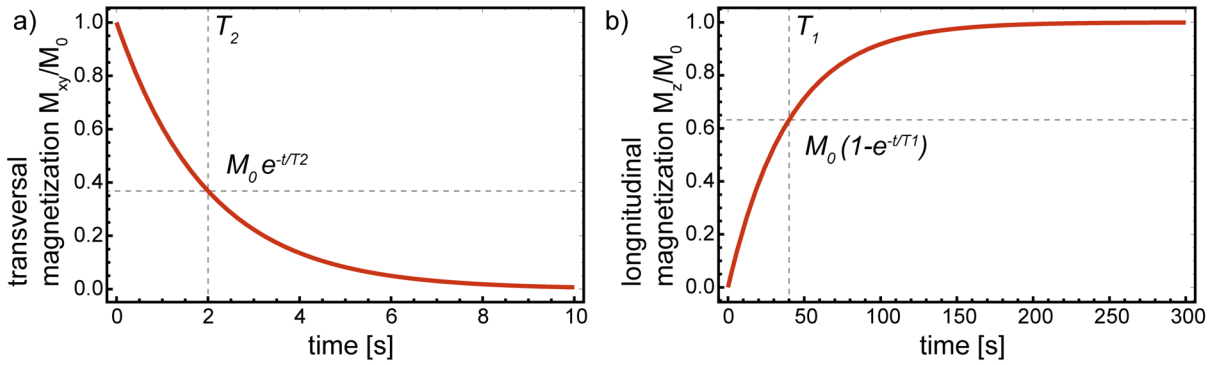

Figure 1-4. a) T_2 decay drives magnetization towards zero. b) T_1 relaxation restores thermal equilibrium polarization.

1.3.2.1 Local fields

Each magnetic moment is influenced by the magnetic field created by nearby magnetic dipoles. These fields are localized and vary in magnitude and orientation due to thermal motion. When the local field variation is in the range of the Larmor frequency it will have an effect on nearby magnetic moments. The biggest contributor to the power spectrum of this field are dipolar coupling and molecular tumbling. While in reality the local fields induced by dipolar coupling are not uncorrelated, analysis of the effects of relaxation is often performed with the assumption that they are randomly fluctuating uncorrelated fields.

1.3.2.2 Transverse relaxation: T_2 and T_2* decay

The longitudinal components of the local field cause the net magnetization to dephase in the transverse plane. This happens due to the random distribution of the local fields in this direction. The part of the bulk magnetization that is dephased by static local fields can be recovered by reverting the time evolution of the dephasing with a spin echo[52]. The part that is dephased by fluctuating local fields cannot be restored. The decay describing transverse relaxation that includes both effects is known as T_2^* decay. The decay describing only the influence of changing local fields is called T_2 decay, where T_2^* and T_2 are the time constants describing the first order rate of decay of the net transverse magnetization (Figure 1-4a).

1.3.2.3 Spin-lattice relaxation towards thermal equilibrium: T_1 decay

Relaxation in the longitudinal direction is also due to randomly fluctuating local fields. However, magnetization does not decay to zero but to its thermal equilibrium value (Figure 1-4b). As mentioned before, each spin sees the magnetic field generated by neighbouring spins,

which varies in magnitude and orientation with thermal motion. If, by chance, the oscillation of a local field is in the range of the Larmor frequency it will affect the reorientation of the magnetic moment. Longitudinal magnetization does not decay to zero because the reservoir of spin energy is coupled to the reservoir of thermal motion[53]. When the polarization is artificially enhanced, the energy of the spin energy reservoir is increased. Two cases of interaction with the thermal motion reservoir can take place:

a) The local field results in an alignment towards the z-axis, the energy of the interaction between the spin and the field is reduced, and energy flows into the surroundings (into the thermal motion reservoir).
b) When turned away from the z-axis, surrounding energy flows into the spin reservoir.

Because the thermal motion reservoir is in equilibrium, higher energy states of this reservoir will be more likely available. That makes case a) more probable. Hence more often magnetic moments are rotated towards z than away from z. Eventually, thermal equilibrium is restored when the population of the energy levels in both reservoirs corresponds to the Boltzmann distribution (equation 1.1).

To summarize, during relaxation the lattice provides random time varying fields that restore the magnetization to thermal equilibrium. The fact that this happens relatively slowly (milliseconds to seconds) is one of the reasons why NMR and MRI are so successful, because it allows time for manipulation and subsequent observation of the non-equilibrium state. Electron Spin Resonance relaxation times, for example, are only micro to nano seconds long[54].

1.3.3 Bloch equations

The consequences of the two relaxation mechanisms for net magnetization $\vec{M}$ can be summarized as

$$\frac{\mathrm{d}}{\mathrm{dt}} M_z = \frac{M_0 - M_z}{T_1}$$

$$\frac{\mathrm{d}}{\mathrm{dt}} M_x = -\frac{M_x}{T_2}$$

$$\frac{\mathrm{d}}{\mathrm{dt}}M_y = -\frac{M_y}{T_2}.$$

Combining this with the effect of an external field $\vec{B}$ on the magnetization $\vec{M}$

$$\frac{\mathrm{d}}{\mathrm{dt}}\vec{M} = \gamma\vec{M} \times \vec{B}$$

gives the Bloch equations[55]

$$\frac{\mathrm{d}}{\mathrm{dt}}M_z = \gamma\left(\vec{M} \times \vec{B}\right)_z + \frac{M_0 - M_z}{T_1}$$
$$\frac{\mathrm{d}}{\mathrm{dt}}M_x = \gamma\left(\vec{M} \times \vec{B}\right)_x - \frac{M_x}{T_2}$$
$$\frac{\mathrm{d}}{\mathrm{dt}}M_y = \gamma\left(\vec{M} \times \vec{B}\right)_y - \frac{M_y}{T_2}$$

which can be used to calculate the magnetization vector under the influence of an external field and relaxation.

1.3.4 Signal-to-noise ratio (SNR)

Polarization is one of the factors that can influence the signal in an MR experiment. Another is the precession frequency, which depends on the field strength and the gyromagnetic ratio. Signal *S* is proportional to the frequency ν_L: $S \propto \nu_L M_{xy}$. If a steady state signal is observed, where the repetition time *TR* is so short that full relaxation is not possible, then another parameter needs to be taken into account, which is the T_1 relaxation time. Using a flip angle θ, the signal then becomes proportional to [56]

$$S(\theta, TR, T_1) \propto \sin\theta \frac{1 - e^{-TR/T_1}}{1 - e^{-TR/T_1}\cos\theta}.$$

When *n* averages are acquired with a repetition time *TR* over a time *t*, the signal to noise ratio (SNR) of the summed spectrum grows with $\sqrt{n} = \sqrt{t/TR}$. Therefore

$$SNR(\theta, \mathrm{TR}, T_1) \propto \frac{1}{\sqrt{\mathrm{TR}}}\sin\theta \frac{1 - e^{-TR/T_1}}{1 - e^{-TR/T_1}\cos\theta}.$$

The largest SNR is achieved when the flip angle θ fulfils the Ernst angle[57] condition, where $\theta = \arccos e^{-TR/T_1}$. Combining this expression with that from Callaghan[58]

$$SNR \propto \gamma^{(11/4)} I(I+1)$$

which approximates the SNR for different thermally polarized nuclei with spin quantum number I and gyromagnetic ratio γ at the same polarizing field, allows a comparison of the SNR for different nuclei at thermal polarization with different T_1 relaxation time constants

$$SNR \propto \frac{1}{\sqrt{T_1}} \gamma^{(11/4)} I(I+1)\,. \tag{1.2}$$

This explains why, at thermal equilibrium, observation of ^{2}H glucose (I = 1, T_1 = 0.064 s [23], γ = 6.536 MHz/T) is more SNR efficient than observation of ^{13}C labelled glucose (I = 1/2, T_1 = 8.9 s [12], γ = 10.7084 MHz/T). The implications this has for the SNR of ^{1}H, ^{2}H and ^{13}C labelled substrates is illustrated in Figure 1-5.

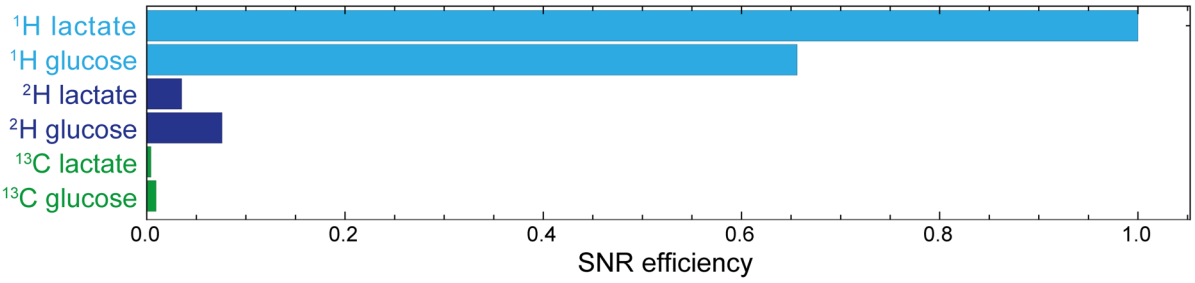

Figure 1-5. SNR efficiency according to equation 1.2. The T_1 times are taken from the literature. For [U-^{2}H, U-^{13}C]glucose T_1 = 8.9 s [12], for [1-^{13}C]lactate T_1 = 45 s [59], for [3,3,3-$^{1}H_3$]lactate T_1 = 1.55 s [60], for glucose ^{1}H T_1 = 3.6 s (the average of $^{1}H_2$ – $^{1}H_6$ and $^{1}H_{6'}$ from Wang *et al.*[61]), for [6,6-$^{2}H_2$]glucose T_1 = 0.064 s [23] and for [3,3-$^{2}H_2$]lactate T_1 = 0.297 s [23]. The literature values were measured at different field strength and in different environments, therefore this is not a quantitative comparison but an illustration of how short T_1 times can compensate for low gyromagnetic ratios.

1.3.5 Chemical shift

MR sensitive nuclei in molecules are exposed to an external B_0 field that is modulated by their chemical environment. This is because the B_0 field causes orbital electrons to circle around the B_0 vector. This induced circular movement of the electrons is effectively a current and therefore causes a small magnetic field with opposite orientation to the B_0 field. Nuclei within

this electron could therefore experience a field weakened by their characteristic electronic surroundings. Consequently, the respective resonance in the spectrum is shifted by a factor $(1+\sigma(\text{ppm})\times 10^{-6})$, where σ is the chemical shift of the nucleus. The chemical shift when expressed relative to a reference frequency (typically Tetramethylsilane - TMS)

$$\delta(\text{ppm}) = 10^6 \times \frac{\upsilon - \upsilon_{ref}}{\upsilon_{ref}}$$

is independent of the B_0 field. This makes chemical shifts, expressed in ppm, comparable regardless of the field strength.

1.3.6 Magnetic field gradients

Key to all MRI experiments is the encoding of physical space by manipulation of the local magnetization precession frequencies. This is done with magnetic field gradients.

1.3.6.1 Phase encoding

A gradient *G(t)* influences the local precessional frequency $\omega = 2\pi\nu$ as follows:

$$\omega(y,t) = \gamma G_y(t)\mathrm{y}\,.$$

If the gradient is applied for a duration *T*, the accumulated phase ϕ of a magnetization vector at position *y* is

$$\phi(y) = \int_0^T \omega(y,t)\mathrm{dt} = \gamma\,\mathrm{y}\int_0^T \mathrm{G_y}\,\mathrm{dt} = 2\pi\mathrm{y}k_y\,,$$

where k_y is the k-space offset, which is proportional to the gradient area. The k-space signal can be written in continuous form as:

$$S(k_y) = \int M_{xy}(y)e^{-i\phi(y)}\,\mathrm{dy}\,.$$

This integral can be discretized to:

$$\mathrm{S}(k_y) = \sum_{n=0}^{N-1} M_{xy}(n\Delta y)e^{-2\pi\mathrm{i}(n\Delta y)k_y}$$

where $M_{xy}=M_x+iM_y$ and $\mathrm{y} = \mathrm{n}\Delta y$ and $\Delta \mathrm{y}$ and n are the pixel size and number of pixels, respectively. Repeating the phase encoding N times for N different values of G_y produces N different sets of phase-encoding twists, or k_y values. This provides sufficient information for $M(n\,\Delta y)$ to be reconstructed by means of inverse Fourier Transformation[48].

1.3.6.2 Frequency encoding

Instead of applying a gradient before the signal acquisition, the gradient can also be used during acquisition, which leads to a decoding of the physical space with frequency instead of accumulated phase. This as well as phase encoding are explained in greater detail in the literature[48].

1.3.6.3 Slice selection

The third application of gradients to encode physical space is the use of gradients during the RF pulses. This allows selection of spins that contribute to the net magnetization by defining the spatial excitation profile with a gradient and a pulse, shaped in such a way that it only acts on the spins resonating on the frequencies defined by the gradient.

1.3.6.4 Alternative form of signal localization

Another important option for localization of MR signal that does not involve gradients is the strategic use of coils with limited receive and/or excitation profiles. The signal acquired with such coils will only originate from a region close to the coil.

1.4 Quantum mechanical description of NMR

Most of magnetic resonance imaging can be explained with the classical description of the NMR experiment and the principles presented in the previous section. In this classical picture evolution of the local net magnetization formed by the magnetic moments is described with the Bloch equations. However, if one uses magnetic resonance methods to manipulate and observe a system of interacting spins, the classical description is no longer suitable. To develop useful pulse sequences and understand the resulting spectra and images, the spectroscopist needs tools

from quantum mechanics. As a foundation for the work presented in chapters 2, 4 and 5 these tools will be introduced here.

This brief introduction is based on the book Spin Dynamics[62] and on Prof. Spielman's Lecture[63].

In quantum mechanics, the trajectory is replaced with the wave function $|\psi(t)\rangle$ that follows the Schrödinger equation

$$\frac{\partial}{\partial t}|\psi(t)\rangle = -i\,\hat{H}(t)|\psi(t)\rangle. \tag{1.3}$$

Where on the right hand side of the equation a factor $\hbar$ (Planck's constant divided by 2π) can be added to change from atomic units to SI units. The Hamiltonian operator $\hat{H}(t)$ is associated with the energy of the system and the wavefunction $|\psi(t)\rangle$ describes the current state of the system in terms of probabilities.

1.4.1 The magnetic moment

Unlike classical physics, quantum mechanics involves two types of angular momentum: the orbital angular momentum, which is associated with the classical angular momentum of orbital revolution, and spin angular momentum. Spin angular momentum is a strictly quantum mechanical and intrinsic property of certain particles that has no classical equivalent. It was first inferred from experiments by Stern and Gerlach[64]. A consequence of spin angular momentum is that certain nuclei have a magnetic moment. The magnetic moment operator $\hat{\mu}$ can be derived from the spin angular magnetic moment operator $\hat{I}$:

$$\hat{\mu} = \gamma\hbar\hat{I}$$

where $\hbar$ is Planck's constant divided by 2π . The value and sign of the gyromagnetic ratio γ depends on the nucleus. If $\gamma > 0$, the magnetic moment is parallel to the spin angular momentum (as in ^{1}H, ^{2}H, ^{13}C, …). If $\gamma < 0$, the magnetic moment and the spin angular momentum are antiparallel (as in ^{15}N). The spin angular momentum projection onto the axis of a strong magnetic field $\vec{B}_0$, is the spin angular projection quantum number m. The magnetic moment for each spin in a state m is

$$\mu_m = m\hbar\gamma\,.$$

Net magnetization arises from the contributions of many magnetic moments. As in the classical description, this magnetization can be detected with RF coils.

1.4.2 Energy, eigenvalues and eigenstates

The energy levels of a spin system can only take a characteristic number of discrete values. There are *I(I+1)* possible values, where *I* is the spin quantum number. To each energy level corresponds a projection quantum number *m.* In the absence of a magnetic field, the states are indistinguishable. When a magnetic field B_0 is applied, the energy levels spread and are distinguishable (Zeeman splitting). In this thesis we will encounter nuclei with spin ½ (^{1}H, ^{13}C, ^{15}N) and nuclei with spin 1 (^{2}H). For the nuclei with spin $I = ½$, $m = -½$ or $+½$. For nuclei with spin $I = 1$, $m = -1$, 0 or $+1$. The energy of each spin in state *m* is

$$E_m = -\mu_m B_0\,.$$

In a spin ½ system, the eigenstate $|\alpha\rangle$ (m = +½) has energy $E_\alpha = -\frac{1}{2}\hbar\gamma B_0$. This state represents the case of *parallel* alignment with B_0 and is energetically favourable. The high energy state $|\beta\rangle$ (m = -½) has energy $E_\beta = +\frac{1}{2}\hbar\gamma B_0$. This state represents the case of *antiparallel* alignment with B_0 and is less favourable. While the energies are eigenvalues of time independent Schrödinger equation

$$\widehat{H}_{Zeeman}\,|A_m\rangle = E_m|A_m\rangle\,,$$

the states are eigenstates of same equation. In a spin ½ system only two eigenstates are possible. A spin 1 system, in contrast, has three eigenstates $-\hbar\gamma B_0$, 0 and $\hbar\gamma B_0$.

For a spin ½ nucleus the superposition of its eigenstates is

$$|\psi\rangle = a|\alpha\rangle + b|\beta\rangle\,.$$

The complex coefficients a and b dictate probabilities for the system to be in either configuration $|\alpha\rangle = \left|\frac{1}{2}, +\frac{1}{2}\right\rangle$ or $|\beta\rangle = \left|\frac{1}{2}, -\frac{1}{2}\right\rangle$. The probabilities, which add up to 1, are:

$$p_\alpha = |a|^2$$
$$p_\beta = |b|^2.$$

Any spin state may be represented as a superposition of the *2I+1* corresponding Zeeman eigenstates. The spin operator of a nucleus with quantum number *I* may therefore be represented as matrices with dimension *(2I+1)*. For example, the matrix representations of the angular momentum operators for a spin ½ nucleus, in the Zeemann eigenbasis $|\alpha\rangle = \left|\frac{1}{2}, +\frac{1}{2}\right\rangle$ and $|\beta\rangle = \left|\frac{1}{2}, -\frac{1}{2}\right\rangle$ are given by

$$\underline{I_x} = \frac{1}{2}\begin{pmatrix}0 & 1\\ 1 & 0\end{pmatrix}, \quad \underline{I_y} = \frac{1}{2i}\begin{pmatrix}0 & 1\\ -1 & 0\end{pmatrix}, \quad \underline{I_z} = \frac{1}{2}\begin{pmatrix}1 & 0\\ 0 & -1\end{pmatrix}.$$

The matrix representations of the angular momentum operators for a spin 1 system, in the Zeemann eigenbasis $\{|1,+1\rangle, |1,0\rangle, |1,-1\rangle\}$ is given by

$$\underline{I_x} = \frac{1}{\sqrt{2}}\begin{pmatrix}0 & 1 & 0\\ 1 & 0 & 1\\ 0 & 1 & 0\end{pmatrix}, \quad \underline{I_y} = \frac{1}{\sqrt{2}}\begin{pmatrix}0 & -i & 0\\ i & 0 & -i\\ 0 & i & 0\end{pmatrix}, \quad \underline{I_z} = \frac{1}{2}\begin{pmatrix}1 & 0 & 0\\ 0 & 0 & 0\\ 0 & 0 & -1\end{pmatrix}.$$

These operators have one very important property, which is cyclic commutation:

$$\left[\hat{I}_i, \hat{I}_j\right] = \mathrm{i}\epsilon_{\mathrm{ijk}}\hat{I}_k \,. \tag{1.4}$$

This will allow us later on to use an intuitive formalism to examine the time development of these operators. The cyclical commutation gives a first hint to the importance of the concept of rotation when evaluating the time evolution of these operators. In the context of this work, no deeper understanding of the states is necessary.

"Remarkably, it appears to be possible to exploit and manipulate these spin states, without ever acquiring a deeper understanding of what these states actually are. Maybe the spin states are their mathematical properties- nothing more, and nothing less."

Malcom Levitt[62]

1.4.3 The Hamiltonian operator

The operator that extracts the possible energy states of a system as eigenvalues when acting on the wavefunction is the Hamiltonian operator $\hat{H}$. In NMR, the Hamiltonian can be independent of time, for example the terms describing the molecular structure or the permanent magnetic field. It can be periodic in time, for example an RF excitation with constant frequency and amplitude. It can also be a function of time, for example a shaped RF pulse. Or it can be random in time as in the case of certain types of relaxation.

If the state of a system is known, the Hamiltonian operators will describe its state at any time in the future. Measurements of the system also imply the application of Hamiltonian operators. In quantum mechanical calculations and simulations, we therefore aim to describe the world and our observation of it (measurements) in terms of Hamiltonian operators.

1.4.3.1 Zeeman Hamiltonian

We can express energy in the units of rad s^{-1} and can therefore remove the factor $\hbar$ when expressing the magnetic moment in terms of the spin angular magnetic moment $\vec{\mu} = \gamma\vec{I}$. The interaction energy between the magnetic field, $\vec{B}$, and the magnetic moment is given by the Zeeman Hamiltonian

$$\hat{H}_{zeeman} = -\gamma\vec{B} \times \hat{\vec{I}}.$$

A chemical shift σ of a nucleus relative to the rotating frame frequency in an external magnetic field $\vec{B}_0 = \vec{e}_z B_0$ leads to the Zeeman Hamiltonian

$$\hat{H}_{zeeman} = -\gamma(1-\sigma)\mathrm{B}_0\hat{I}_z = \Omega_0\,\hat{I}_z\,. \tag{1.5}$$

1.4.3.2 External Magnetic Field Hamiltonian

An on-resonance RF excitation with an amplitude B_1 and a phase ϕ relative to the rotating reference frame can be expressed with the Hamiltonian

$$\hat{H}_{RF} = \gamma\mathrm{B}_1\left(\hat{I}_x\cos\phi + \hat{I}_y\sin\phi\right).$$

A hard pulse around the rotating frame x-axis is expressed as:

$$\hat{H}_{RF} = \omega_1 \hat{I}_x, \tag{1.6}$$

where $\omega_1 = \gamma B_1$ is the amplitude of the B_1 field in rad s^{-1}.

1.4.3.3 The Interaction Hamiltonian

In the most general case, the interaction Hamiltonian describes all interactions between different spins. It has an application in relaxation theory where it describes the intramolecular through space interaction of dipole or quadrupole fields[65]. The most important interaction mechanism is the through-bond or *J*-coupling interaction (also known as scalar, spin-spin or indirect coupling). This interaction of spins is mediated by electrons.

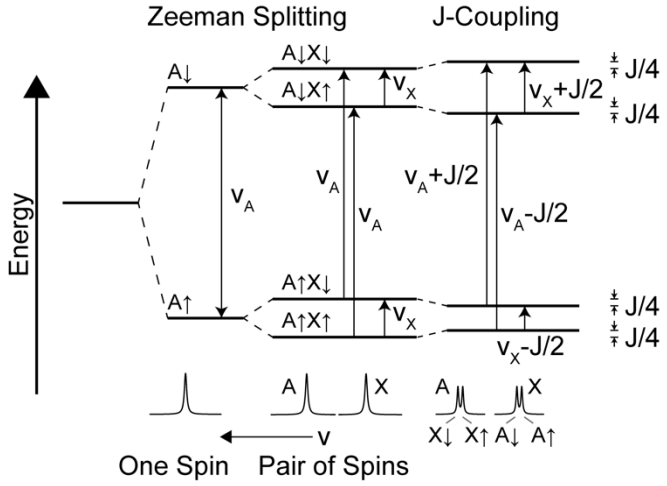

Figure 1-6. Energy levels of spin systems. From left to right: Zeeman splitting in a one spin system, Zeeman splitting in a two-spin system and Zeeman splitting with additional *J*-coupling in a two-spin system.

For illustration, consider a simple system of two nuclei and two electrons. The nuclear spin of the first nucleus will polarize a nearby electron spin antiparallel to its own state. Because of Pauli's exclusion principle another electron in the same bond can then no longer be in the same antiparallel state and will have to go into the parallel state. This parallel state electron will polarize the second nuclear spin in its proximity to be antiparallel. Thereby a coupling is generated that connects nuclear spins at distant sites in the same molecule. The relevant mechanisms are Fermi contact interaction (nucleus - electron interaction), Pauli's exclusion

principle (electron – electron interaction) and a second Fermi contact interaction (electron - nucleus interaction). The splitting (Figure 1-6) in the spectra caused by this interaction is expressed in Hertz and described by the letter *J*, hence *J*-coupling. The value of *J* doesn't depend on the B_0 field strength. Unlike through space couplings, the *J*-coupling is not averaged out by motion in isotropic liquid substrates and is therefore an extremely important mechanism to determine structure and manipulate spin population levels in liquid state NMR. The Hamiltonian describing a heteronuclear coupling in an isotropic liquid is

$$\hat{H}_{indirect\ coupling} = \pi J\ 2\hat{I}_z\hat{S}_z\,. \tag{1.7}$$

1.4.4 NMR in Liouville space

It is convenient to describe NMR in Liouville space where the density operator $\hat{\rho}$ is a probability weighted sum over the individual state densities. The diagonal elements are the populations, their difference indicates polarization. The off-diagonal elements are coherences, which indicate transverse magnetization or more complicated states like singlet states.

The density matrix of a spin ½ ensemble is:

$$\hat{\rho} = \overline{|\varphi\rangle\langle\varphi|} = \begin{pmatrix} \rho_{\alpha\alpha} & \rho_{\alpha\beta} \\ \rho_{\beta\alpha} & \rho_{\beta\beta} \end{pmatrix}.$$

The time evolution of a system in Liouville space is described by the Liouville-von Neumann equation

$$\frac{\partial}{\partial t}\hat{\rho} = -i\left[\hat{H}, \hat{\rho}\right] \tag{1.8}$$

$$= -i\hat{\hat{H}}\hat{\rho}. \tag{1.9}$$

The double hat indicates a super operator, in this case the commutator of the Hamiltonian operator $\hat{\hat{H}}\ x\ = \left[\hat{H}, \mathrm{x}\right]$. Observables of the statistical ensemble can be calculated as:

$$\overline{\langle\hat{A}\rangle} = Tr\{\hat{\rho}\hat{A}\}\,.$$

The evolution under the influence of a *time independent* Hamiltonian can be calculated as:

$$\hat{\rho}(t) = e^{-i\hat{\hat{H}}t}\hat{\rho}(0) = e^{-i\hat{H}t}\hat{\rho}(0)e^{i\hat{H}t}\,. \tag{1.10}$$

Evolution under the influence of a *time dependent* Hamiltonian can be approximated by rewriting the *time dependent* Hamiltonian with piecewise *time independent* (constant) Hamiltonians and applying them sequentially:

$$\hat{\rho}(t = t_1 + t_2 \ldots) = \cdots e^{-i\hat{\hat{H}}_2 t_2} e^{-i\hat{\hat{H}}_1 t_1} \hat{\rho}(0)\,.$$

1.4.5 Product operator formalism

The effect of an NMR pulse sequence on the density operator can be calculated with a formalism that illustrates transitions of the operator as rotations around axes defined by the acting Hamiltonian. This formalism is called the product operator formalism. Key to this formalism is the identity:

$$e^{-i\theta\hat{\hat{\mathrm{A}}}}\hat{\mathrm{B}} = \hat{\mathrm{B}}\cos\theta + \mathrm{i}\left[\hat{\mathrm{A}}, \hat{\mathrm{B}}\right]\sin\theta\,. \tag{1.11}$$

Which is true for all cyclically commuting operators. As stated in equation (1.4), the spin operators $\hat{I}_x$, $\hat{I}_y$ and $\hat{I}_z$ cyclically commute. Their commutations $\left[\hat{I}_i, \hat{I}_j\right] = i\epsilon_{ijk}\hat{I}_k$ are

$$\left[\hat{I}_x, \hat{I}_y\right] = \mathrm{i}\hat{I}_z, \quad \left[\hat{I}_y, \hat{I}_z\right] = \mathrm{i}\hat{I}_x \text{ and } \quad \left[\hat{I}_z, \hat{I}_x\right] = \mathrm{i}\hat{I}_y\,. \tag{1.12}$$

The product operator for two spin systems have similar properties:

$$\left[\hat{S}_x, 2\hat{S}_y\hat{I}_z\right] = i2\hat{S}_z\hat{I}_z\,, \quad \left[2\hat{S}_x\hat{I}_z, \hat{S}_y\right] = i2\hat{S}_z\hat{I}_z\,. \tag{1.13}$$

Comparing equations (1.11) to (1.13) reveals that the time evolution of $\hat{\rho}$ under the influence of a time independent $\hat{H}$ that cyclically commutes with $\hat{\rho}$ can be described as a rotation away from the initial $\hat{\rho}$ into the state defined by the commutation. These rotations have to be evaluated sequentially for the components that cyclically commute, i.e. $\hat{I}_x$, $\hat{I}_y$, $\hat{I}_z$, $2\hat{S}_x\hat{I}_z$… with the respective parts of the acting Hamiltonian. The angle of that rotation is described by parameters of the Hamiltonian (Figure 1-7).

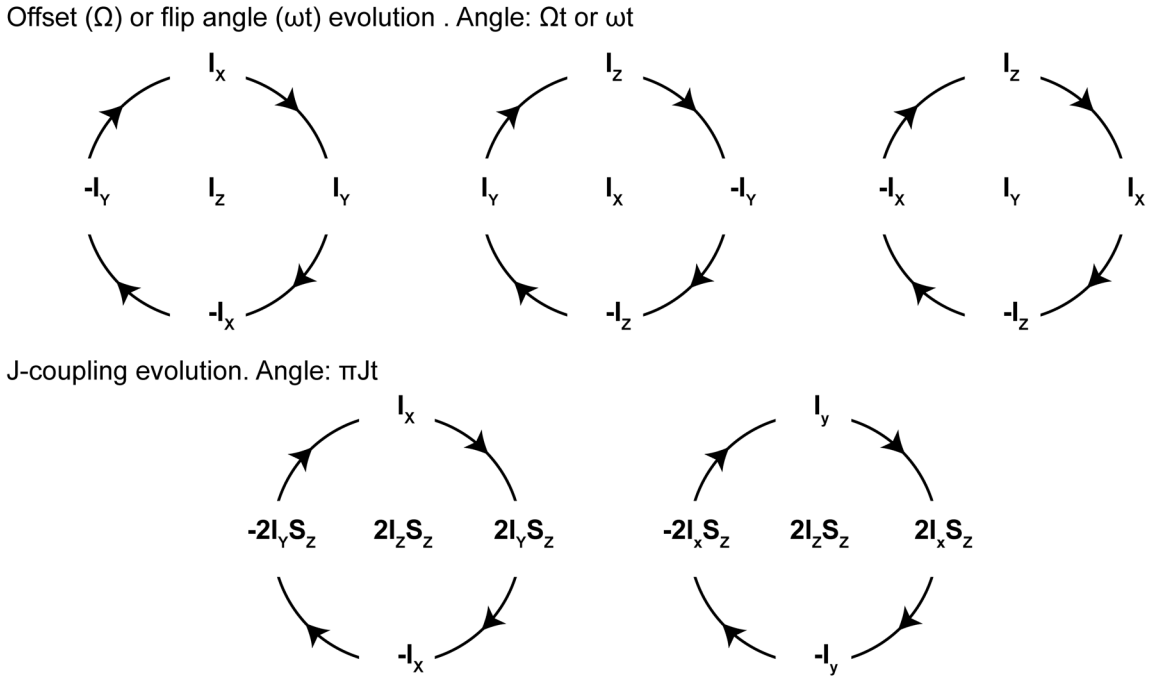

Figure 1-7. In the product operator formalism, time evolution can be understood as rotations away from the initial state into a new state defined by the commutator of the Hamiltonian and the initial state. The angle of rotation is defined by the duration of the applied Hamiltonian and, dependent on the type of evolution, the offset, the RF field strength or the coupling constant.

1.4.5.1 Evolution under a constant on resonance RF field

A fixed amplitude RF pulse around the rotating frame x-axis can be written as $\widehat{H}_{RF} = \omega_1 \hat{I}_x$ (equation 1.6). The time evolution of $\hat{I}_z$ for an interval τ according to equation (1.10) is:

$$\hat{\rho}(\tau) = e^{-i\omega_1 \hat{I}_x} \hat{I}_z \, .$$

Using equations (1.11) and (1.12) yields

$$\hat{\rho}(\tau) = \hat{I}_z \cos \omega_1 \, \tau - \hat{I}_y \sin \omega_1 \, .$$

This is exactly what we would expect in the classical picture when $\vec{M}_z$ is rotated by an angle $\omega_1 \tau$ around the x-axis of the rotating frame. Similar relations can be deduced for all angular momentum operators.

1.4.5.2 Offset evolution

A spin with an offset Ω_0 relative to the rotating frame frequency experiences a Hamiltonian $\widehat{H}_{zeeman} = \Omega_0 \hat{I}_z$. Using equations (1.11) and (1.12) shows for $\hat{\rho}(0) = \hat{I}_x$:

$$\hat{\rho}(\tau) = e^{-i\Omega_0 \hat{\hat{I}}_z} \hat{I}_x = \hat{I}_x \cos \Omega_0 \tau + \hat{I}_y \sin \Omega_0 \tau .$$

The evolution for $\hat{\rho}(0) = \hat{I}_y$ can be derived the same way.

1.4.5.3 *J*-coupling evolution

Even though we lose the classical analogy of rotating magnetization in three-dimensional space, evolution under the *J*-coupling Hamiltonian (equation 1.7) is mathematically no more complicated than the previous rotations. Using the definition (1.11) and the identities (1.13), the result is still a rotation, but now the axes are defined by coherences corresponding to in-phase and anti-phase terms instead of just in-phase terms. For $\hat{\rho}(0) = \hat{I}_x$ the result of evolution for a time τ is:

$$\hat{\rho}(\tau) = \mathrm{e}^{-\mathrm{i}\pi \mathrm{J} 2\widehat{\hat{I}_z \hat{S}_z}} \hat{\mathrm{I}}_\mathrm{x} = \hat{\mathrm{I}}_\mathrm{x} \cos \pi \mathrm{J}\tau + 2\hat{\mathrm{I}}_\mathrm{y}\hat{\mathrm{S}}_\mathrm{z} \sin \pi \mathrm{J}\tau .$$

Similarly, the evolution for $\hat{\rho}(0) = \hat{I}_y$ is

$$\hat{\rho}(\tau) = \mathrm{e}^{-\mathrm{i}\pi \mathrm{J} 2\widehat{\hat{I}_z \hat{S}_z}} \hat{\mathrm{I}}_\mathrm{y} = \hat{\mathrm{I}}_\mathrm{y} \cos \pi \mathrm{J}\tau - 2\hat{\mathrm{I}}_\mathrm{x}\hat{\mathrm{S}}_\mathrm{z} \sin \pi \mathrm{J}\tau .$$

1.4.5.4 Evolution of higher order spin systems

The evolution of every spin system of the form IS_N or I_NS under the influence of evolving offsets, *J*-couplings or pulses can be evaluated by applying sequentially the relevant rotations for each spin. This works, because rotations of a spin do not affect operators of other spins as operators corresponding to different spins commute with each other.[53]

1.4.6 Relaxation

A shortcoming of the product operator approach is that it does not include the influence of relaxation in its predictions of the density operator. Relaxation is the process by which phase coherence among spins returns to its equilibrium value (as given by the Boltzmann distribution). As introduced in section 1.3.2, the basic principle in relaxation theory is that spatial and temporal magnetic field variations of the surroundings couple the spin system to the lattice structure and thereby allow it to return to thermal equilibrium. In other words, the lattice structure acts as a heat sink for the spin temperature. The magnetic field variations can have different origins, but they always average to zero for a large number of spins.

For a full description including relaxation, the Liouville-von Neumann equation (1.8) needs to be extended by an additional term to the Hamiltonian representing all the fluctuating interactions that average to zero for large numbers of spin systems. These additional terms are also called incoherent contributions. The part that is the same for all spins is, in this context, called the coherent part of the Hamiltonian. Combining the two parts of the Hamiltonian gives the new expression for the Liouville-von Neumann equation

$$\frac{\partial}{\partial t}\hat{\rho} = -\mathrm{i}\left[\widehat{H}_{\mathrm{coh}} + \widehat{H}_{\mathrm{incoh}}, \hat{\rho}\right].$$

The incoherent or fluctuating Hamiltonians describe all the processes relevant for relaxation such as dipolar and quadrupolar couplings and chemical-shift anisotropy. Introducing the thermal equilibrium density operator $\hat{\rho}_{eq}$ and assuming that the incoherent Hamiltonian is random (bias-free perturbation) and that the time scale of random fluctuations is much shorter than changes in the density operator (weak collision or Redfield limit)[66]. The master equation with relaxation can be written as [67]

$$\frac{\partial}{\partial \mathrm{t}}\hat{\rho} = -\mathrm{i}\widehat{\widehat{H}}_0\hat{\rho} - \hat{\hat{\Gamma}}\{\hat{\rho} - \hat{\rho}_{\mathrm{eq}}\}.$$

There are sophisticated ways of solving this equation under general conditions, however they require precise knowledge of relaxation pathways far beyond the simple relaxation time constants T_1 and T_2. We will therefore consider only the simplest cases that can be described with these parameters, which are borrowed from simpler descriptions of NMR and MRI. In

this semi-classical approximation, relaxation is assumed to be simply caused by randomly fluctuating fields. We can straightforwardly assign measured relaxation values T_1 to the I_z operators and T_2 to I_x and I_y operators. The relaxation rates $R=1/T$ of the anti-phase magnetization operators of multi spin systems ($I_x S_z$ etc.) are the sum of the relaxation rates of the operators building the coherence, for example $R_{I_x S_z} = \frac{1}{T_{2,I}} + \frac{1}{T_{1,S}}$.

1.4.7 Simulations

The multi spin system simulations presented in chapters 2, 4 and 5 were performed in *SpinDynamica*[68], which is a package for Mathematica (Wolfram Research, Inc., Champaign, Illinois, USA). The aim of *SpinDynamica* is to simulate an experiment by entering the Hamiltonian and relaxation superoperator of a spin system[68].

1.4.7.1 Hamiltonian operator in SpinDynamica

For a simulation, first the number of spins making up the spin system is defined, then the Hamiltonian describing the time independent part, usually the structure and the chemical shifts for the molecule are specified. The code excerpt:

```
SetSpinsystem[2];
H0= 2 pi (-90) opI[1,"z"]. opI[2,"z"]
```

for example, describes a two-spin system in the rotating reference frame where spins #1 and #2 are J-coupled with J = -90Hz. To evaluate the time development of spin #1 I_y under a 90° x pulse followed by an interval $1/J$ of free evolution, a sequence of events is described as

```
pulseSequence={RotationSuperoperator[{1},{pi/2,"x"}],{None,1/J}}
```

Time development of the spin system is then evaluated using the *Trajectory[]* function:

```
Trajectory[opI[1,"z"]→ opI[1,"y"], pulseSequence , BackgroundGenerator→H0]
```

To simulate shaped pulses the *ShapeFunction[]* instruction is used to let time dependent Hamiltonians act on the spin system. The simulation of an adiabatic BIR4 pulse[47] and its effect on two spins coupled to a third spin is illustrated in Figure 1-8.

```
In[85]:= Needs["SpinDynamica`"];
         SetSpinSystem[3];
         J = -90;
         H0 = 2 π J opI[1, "z"].opI[3, "z"] + 2 π J opI[2, "z"].opI[3, "z"];
         obsSpin = {1, 2};
         decSpin = {3};
         ζ = 10;
         κ = ArcTan[20];
         tp = 0.0005;
         Δωmax = 2 π 45 / (4 tp);
         ω1maxDec = 2 π 2500;
         ω1maxObs = 2 π 4000;
         Δϕ1 = 3 π / 2;
         Δϕ2 = -Δϕ1;
         ϖmax = -Δωmax tp Log[Cos[κ]] / (κ Tan[κ]);
         Δϕ1ex = ((π / 2) / 2) + π;
         Δϕ1ex = -Δϕ1ex;

         SetSpinSystem: the spin system has been set to {{1, 1/2}, {2, 1/2}, {3, 1/2}}

In[102]:= AHP[t_] := Tanh[ζ (t / tp)] * Exp[I (ϖmax - (Δωmax tp / (κ Tan[κ])) Log[Cos[κ (tp - t) / tp] / Cos[κ]])];
         BIR4exc = {
            {ShapeFunction[{τ, 1}, ω1maxObs (Re[AHP[-τ]] opI[obsSpin, "x"] + Im[AHP[-τ]] opI[obsSpin, "y"])], tp},
            {ShapeFunction[{τ, 0}, ω1maxObs (Re[Exp[I Δϕ1ex] AHP[τ]] opI[obsSpin, "x"] + Im[Exp[I Δϕ1ex] AHP[τ]] opI[obsSpin, "y"])], tp},
            {ShapeFunction[{τ, 1}, ω1maxObs (Re[Exp[I Δϕ1ex] AHP[-τ]] opI[obsSpin, "x"] + Im[Exp[I Δϕ1ex] AHP[-τ]] opI[obsSpin, "y"])], tp},
            {ShapeFunction[{τ, 0}, ω1maxObs (Re[AHP[τ]] opI[obsSpin, "x"] + Im[AHP[τ]] opI[obsSpin, "y"])], tp}
           };

In[104]:= {X, Y, Z} = Trajectory[opI[obsSpin, "z"] → {opI[{1, 2}, "x"], opI[{1, 2}, "y"], opI[{1, 2}, "z"]}, {BIR4exc, {None, Abs[0.5 / J]}}, BackgroundGenerator → H0];
         Plot[{X[t], Y[t], Z[t]}, {t, 0, EventDuration[{BIR4exc, {None, Abs[0.5 / J]}}]}, PlotRange → {All, All}, FrameLabel → {"time [s]", "Magnetization"},
          PlotLegends -> "Expressions"]

Out[105]=
```

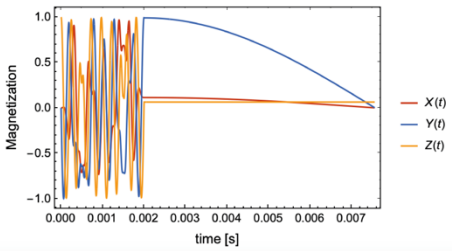

Figure 1-8. *SpinDynamica* code for simulation of a BIR4 90° pulse on a 3-spin system where spin #1 and #2 are coupled to spin #3 with *J=-90* Hz.

1.4.7.2 Relaxation in SpinDynamica

Spin relaxation is incorporated into spin dynamical simulations by including a relaxation superoperator $\hat{\Gamma}$ as the incoherent part of the Hamiltonian. While *SpinDynamica* can handle relaxation superoperators with non-diagonal entries for specific relaxation mechanisms we focus on the use of the semi classical model using only two parameters (T_1 and T_2) per spin, the longitudinal and transversal relaxation times. This is implemented in *SpinDynamica* with the instruction

PhenomenologicalRelaxationSuperoperator[{{1,$T_{1,\text{spin\#1}}$,$T_{2,\text{spin\#1}}$},{2,$T_{1,\text{spin\#2}}$,$T_{2,\text{spin\#2}}$},…}]

This superoperator is added to the *BackgroundGenerator* to be included in simulations.

Chapter 2 Measuring lactate dehydrogenase activity with proton detected [1-^{13}C]lactate hyperpolarization

---

Some paragraphs and figures in this chapter have been adapted from my first-year report. The in vivo work presented at the end of this chapter has been published in

Wang J, Kreis F, Wright AJ, Hesketh RL, Levitt MH, Brindle K. Dynamic ^{1}H imaging of hyperpolarized [1-^{13}C]lactate in vivo using a reverse INEPT experiment. *Magn Reson Med.* 2018;70:741-747.

My contribution to the publication were the NMR spectroscopic experiments, simulation of the pulse sequence under the influence of relaxation and defining the parameters for the delays in the reverse INEPT sequence.

The *J*-couplings introduced in the previous chapter can be used to transfer polarization from one spin to another coupled spin. Since the detection sensitivity of an NMR experiment depends on the polarization, this can be very useful when observing nuclei with low polarization.

Historically the motivation for transferring polarization from one nucleus to a coupled nucleus of another kind came from the differences in the sensitivity to detection of nuclei with different gyromagnetic ratios (γ). Nuclei with high γ are generally easier to observe than nuclei with low γ for the following reasons[62]:

1. Nuclear magnetic moment is proportional to γ; hence a higher γ nucleus gives higher signal.

2. The nuclear Larmor frequency is proportional to γ. The induced voltage in the receiver coil is proportional to the rate of change of the magnetic moment. Higher frequencies therefore give a stronger signal.
3. At thermal equilibrium the Boltzmann polarization of the spins is proportional to γ. Hence with high γ species more spins contribute to the signal.
4. Since high γ nuclei are strongly magnetic, they tend to couple strongly to the molecular environment and therefore have shorter T_1 times. This allows for faster repetition times (TR) and yields a higher SNR per unit time. However, there are exceptions to this rule, for example ^{2}H nuclei, which are quadrupolar, have very short T_1 relaxation times.

In classical (thermally polarized) NMR efforts have been made to transfer polarization from high γ nuclei to low γ nuclei. This allows observation of low γ nuclei with an enhanced signal due to points 3 and 4. When 100% of the polarization from the high γ nucleus is transferred to the low γ nucleus, detection sensitivity of the low γ nucleus is enhanced by a factor corresponding to the ratio of their gyromagnetic ratios. In this way the sensitivity of a ^{13}C nucleus bound to a proton can be enhanced four-fold assuming that all the polarization is transferred.

2.1 Polarization transfer in dissolution DNP-NMR and MRI

With DNP ^{13}C polarization is enhanced by 4 -5 orders of magnitude and therefore it is possible to image this polarization directly. However, there are good reasons to transfer the hyperpolarization to protons and then detect the polarization in this higher γ nucleus:

In hyperpolarized samples, the polarization no longer depends on the Boltzmann distribution; therefore, the effect of the difference in thermal polarization levels of ^{1}H and ^{13}C is irrelevant. Hence, no polarization is gained from the transfer, but when observing high ɣ nuclei a gain in sensitivity is obtained from the larger nuclear magnetic moment and higher Larmor frequency.

Both give an advantage in the form of a higher SNR. When noise is considered as well, the overall increase in the SNR as a function of the detection frequency, ν, is given by[69]:

$$SNR \propto \frac{\nu^2}{(\alpha a^2 \nu^{1/2} + \beta \nu^2 b^5)^{1/2}}$$

where a and b are coil geometry parameters and α and β are weightings for the two sources of noise, where α represents coil noise and β sample noise.

Another advantage of proton detection is that in proton imaging just ¼ of the gradient strength is needed compared to that need for ^{13}C imaging. The fact that MRI is generally performed with protons has as a consequence that much better proton coils are available than for x-nuclei. The scanner industry has developed advanced ^{1}H coil systems, optimized for imaging at high resolution. In contrast, ^{13}C coils are a niche product mostly used for spectroscopy. Another benefit of observing hyperpolarized protons is that it is relatively easy to get a localized thermal ^{1}H spectrum[60,70,71]. This thermal acquisition could, for example, be incorporated into a kinetic model of an observed reaction.

Given all the benefits of proton imaging, it is tempting to try polarizing protons directly, and in fact a few studies have reported hyperpolarized water, in which protons are hyperpolarized, as a contrast agent for imaging perfusion[72,73]. The main reason why it is not feasible to investigate metabolism with directly hyperpolarized protons is the very short proton relaxation time. A typical *in vivo* value (human brain at 3 T) for the lactate methyl protons is T_1 = 1.550 s and T_2 = 1.2 s [60]. Other values in the literature include: T_1 = 360.9 ms, 580.9 ms and 634.1 ms (T_2 = 31.7 ms, 33.5 ms, 31.4 ms) in rat brain at 4.0 T, 9.4 T and 11.7 T respectively [74]. In contrast, [1-^{13}C]pyruvate has a T_1 of 40 s at 9.4 T [18] and [1-^{13}C]lactate a T_1 of 45 s at 3 T [59] .

2.1.1 The I_3S spin system

The aim of the project was to transfer polarization from [1-^{13}C] to [3,3,3-$^{1}H_3$] in [1-^{13}C]lactate produced from hyperpolarized [1-^{13}C]pyruvate (Figure 2-1). In order to describe the outcome of such a polarization transfer experiment we use the product operator formalism introduced earlier. The four-spin system, which describes the coupling between 1-^{13}C and 3,3,3-$^{1}H_3$ in [1-^{13}C]lactate, is given by:

$$\hat{\rho} = \mathbb{B}_S \hat{S}_{1z} + \mathbb{B}_I \left(\hat{I}_{2z} + \hat{I}_{3z} + \hat{I}_{4z} \right)$$

At thermal equilibrium, the Boltzmann factors describing the polarization are $\mathbb{B}_I = \hbar\gamma_I B_0 / k_B T$ and $\mathbb{B}_S = \hbar\gamma_S B_0 / k_B T$.

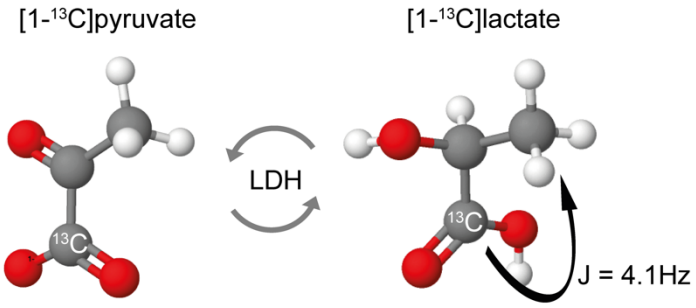

Figure 2-1. Lactate dehydrogenase (LDH) catalyses exchange of hyperpolarized ^{13}C label between injected hyperpolarized [1-^{13}C]pyruvate and the endogenous lactate pool. Hyperpolarized [1-^{13}C]lactate is detected by transferring hyperpolarization from the C1 carbon to the spin-coupled (J = 4.1Hz) methyl protons.

2.1.2 Insensitive Nuclei Enhanced by Polarization Transfer (INEPT)

The original motivation for an experiment that transfers polarization from one nucleus to another, was to benefit from the higher thermal polarization in a high γ nucleus, such as proton ($\gamma/2\pi$=42.576 MHz/T) while observing a low γ nucleus, such as ^{13}C ($\gamma/2\pi$=10.705 MHz/T). The most common example of a pulse sequence used for this purpose is the refocused INEPT sequence [75].

This sequence (Figure 2-2a) applied to a two-spin system, with one high γ (I) and one low γ (S) nucleus, is best understood when divided into two parts with durations τ_1 and τ_2. During τ_1, the $-\mathbb{B}_I \hat{I}_y$ magnetization evolves over a time of 1/(2J) into $-\mathbb{B}_I 2\hat{I}_x\hat{S}_z$ anti-phase magnetization. The 90°pulses transfer the anti-phase state from the I spins to the S spins, the state is then $-\mathbb{B}_I 2\hat{I}_z\hat{S}_x$. The second spin echo sandwich with duration τ_2=1/(2J) in Figure 2-2a allows the anti-phase state to evolve into the in-phase state $\mathbb{B}_I \hat{S}_y$. The spin echoes refocus any accumulated phase offset due to B_0 field inhomogeneity and invert the coupling term $\hat{I}_z\hat{S}_z$ twice so it remains invariant.

The purpose of this sequence is to produces a state where the polarization of the S spins is proportional to the Boltzmann factor of the I spin. Since the Boltzmann factor in thermally polarized spins is proportional to the gyromagnetic ratio of the respective nuclei, the polarization in thermal acquisitions is enhanced by the ratio of the gyromagnetic ratios of the nuclei involved. Compared to a 90° pulse acquisition this leads to a signal increase of γ_I/γ_S if relaxation during the INEPT sequence is neglected.

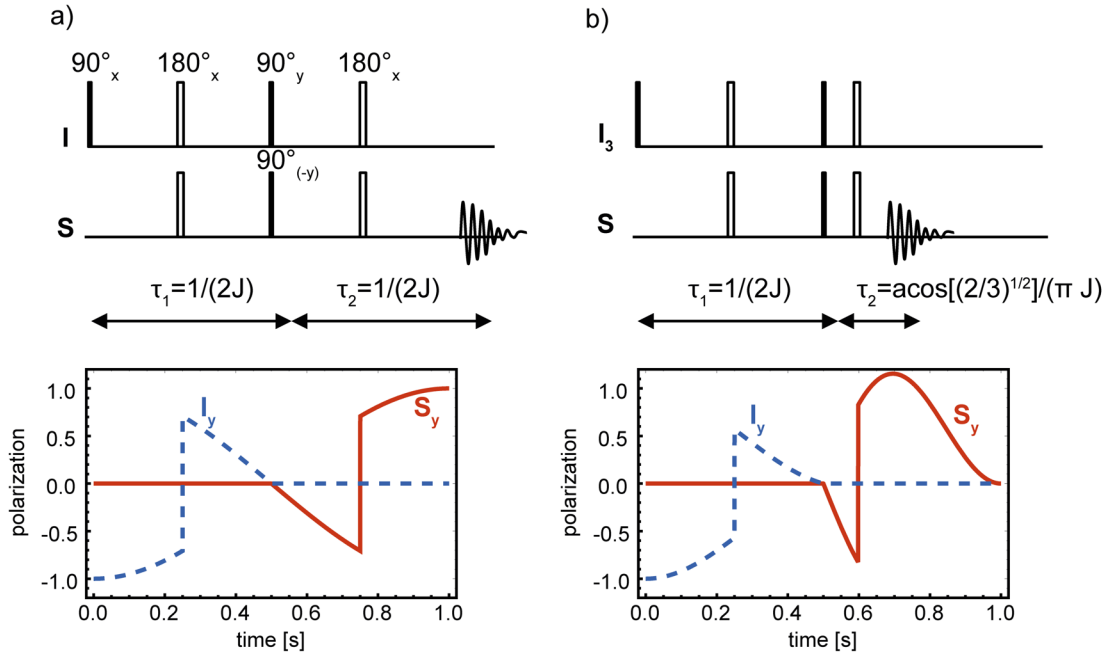

Figure 2-2. Layout of the a) IS and b) I_3S I→S INEPT experiment and the time evolution of the I_y and S_y magnetizations. Simulated for $J = 1$ Hz.

2.1.2.1 INEPT in I_3S systems with I to S transfer

When an S spin is coupled to three magnetically equivalent I spins in an I_3S system the INEPT sequence can still be used, but some modifications have to be made. While in an IS system the in-phase transverse magnetization evolves during τ_2 as $\mathbb{B}_I \sin \pi J t$, in a I_3S system it is proportional to $3\mathbb{B}_I \sin \pi J t \cos^2 \pi J t$. Because the later term reaches its maximum faster, the second spin echo sandwich has to be shortened accordingly (Figure 2-2b). Optimal transfer in this system is reached for $\tau_2 = \left(\cos^{-1}\sqrt{2/3}\right)/(\pi J)$ and an enhancement of $\left(2/\sqrt{3}\right)(\gamma_I/\gamma_S)$ can be achieved [53,62].

2.1.3 History of INEPT in hyperpolarized experiments

The above examples of the refocused INEPT experiment for I to S transfer in IS and I_3S spin systems are very well known, however little has been published about polarization transfer in the reverse direction, from S to I in four spin I_3S systems. This direction of transfer, from low γ to high γ nuclei is only beneficial, when the S spins are hyperpolarized to a far greater extent than the thermally polarized I spins. There have been a limited number of studies where hyperpolarization has been transferred to protons using INEPT sequences:

Mishkovsky *et al.* transferred hyperpolarization in sodium [1,2-$^{13}C_2$] and sodium [1-^{13}C] acetate using a non-refocused INEPT, without discussing the details of the influence of the spin topology on the evolution delays[76]. Harris *et al.* showed transfer of polarization from hyperpolarized ^{15}N to 2-CH_2 protons in choline. They used an un-refocused INEPT (only the first delay, τ_1, and the 90° pulses in Figure 2-2a). The duration of the spin echo sandwich was $\tau_1 = 1/2J$, which is the timing appropriate for a two spin INEPT even though they were working with a three-spin system. They observed the anti-phase state in the protons[77]. Sarkar *et al.* also used choline and transferred polarization from ^{15}N to the 2-CH_2, 3-CH_2 and $N(CH_3)_3$ protons. They worked with a refocused INEPT sequence but did not disclose the timings of the sequence. However, their proton spectrum suggests, that it was not ideal: the 2-CH_2 protons did not give any signal, the 3-CH_2 proton resonances seem to be in an anti-phase state, and only the $N(CH_3)_3$ group gave an in phase peak [78]. Chekmenev *et al.* [79] used hyperpolarization generated by PASADENA (PArahydrogen and Synthesis Allow Dramatically Enhanced Nuclear Alignment) [80,81] . They used 1-^{13}C-succinate-d2, where one proton per CH_2 group was exchanged for a deuteron, and 2,2,3,3-tetrafluoropyl 1-^{13}C-propionate-d3 (TFPP), with two deuterated CH_2 groups and one un-deuterated CH_2 group. They observed strong enhancement in the groups where just one proton was present[79]. Dzien *et al.* worked with hyperpolarized [U-$^2H_3$,2-^{13}C]pyruvate added to yeast pyruvate Decarboxylase and observed the product of the reaction, [1- ^{1}H, 2,2,2-$^2H_3$,1-^{13}C]acetaldehyde with an INEPT sequence. Due to the deuteration the system is effectively a two spin IS system[82].

Summarizing, refocused INEPT has been used to transfer hyperpolarization in IS spin systems, from the S to the I spins. In an I_2S spin system hyperpolarization has been transferred from S

to I using a non-refocused INEPT sequence. The theory of transferring polarization from S to I spins in an I_2S or I_3S system has not been discussed. In the studies mentioned, either the system was deuterated to such an extent that an IS system was created [79,82] or anti-phase states were observed [77,78].

My goal was therefore to develop a reverse refocused INEPT sequence for an I_3S spin system and observe in-phase magnetization in the I spins. It is necessary to aim for a state that corresponds to an in-phase spectrum, because otherwise problems would arise when combining the transfer block with imaging readout or heteronuclear decoupling blocks. Such a sequence would then be used to transfer hyperpolarization from C1 position to the three magnetically equivalent [3,3,3-$^1H_3$]protons in [1-^{13}C]lactate, which is produced from hyperpolarized [1-^{13}C]pyruvate in the reaction catalysed by lactate dehydrogenase (LDH) (Figure 2-1).

2.2 Pulse sequence development

2.2.1 Simulations

All simulations were performed using *SpinDynamica*[68] as described in the previous chapter. The Hamiltonian of the I_3S system describing [1-^{13}C]lactate is

$$\hat{H}_0 = 2\pi \mathrm{J}\hat{S}_{1z}\hat{I}_{2z} + 2\pi \mathrm{J}\hat{S}_{1z}\hat{I}_{3z} + 2\pi \mathrm{J}\hat{S}_{1z}\hat{I}_{4z}.$$

The coupling constant between the C1 carbon and the methyl protons is J = 4.1 Hz in [1-^{13}C]lactate.

2.2.2 Adaption for S → I transfer in I_3S system

To find the optimal inter pulse delays, a product operator calculation was used. Levitt showed, that when only the evolution of the couplings and not the evolution of the offsets is of interest, an "equivalent pulse sequence design", as shown in Figure 2-3, can be used for the calculations [62]. In this equivalent sequence the 180° pulses are shifted to be directly after the 90° pulses. In this way only two blocks of free evolution have to be calculated.

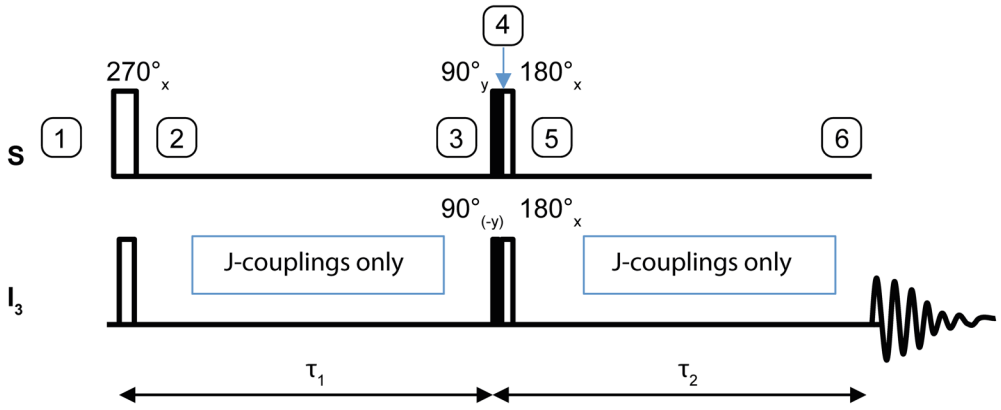

Figure 2-3. Equivalent pulse sequence describing evolution of the couplings during the refocused INEPT. Sequence modified from the book Spin Dynamics [62].

The development of the spin density operator $\hat{\rho}$ was calculated piece-by-piece. $\hat{\rho}_1, \hat{\rho}_2, \hat{\rho}_3$ ... refers to the operator at time points 1,2,3… as indicated in Figure 2-3:

$$\hat{\rho}_1 = \frac{1}{16}\hat{1} + \frac{1}{16}\mathbb{B}_S\hat{S}_{1z} + \frac{1}{16}\mathbb{B}_I\left(\hat{I}_{2z} + \hat{I}_{3z} + \hat{I}_{4z}\right)$$

$$\downarrow \pi_x^I + \left(\frac{3\pi}{2}\right)_x^S$$

$$\hat{\rho}_2 = \cdots + \frac{1}{16}\mathbb{B}_S\hat{S}_{1y} - \frac{1}{16}\mathbb{B}_I\left(\hat{I}_{2z} + \hat{I}_{3z} + \hat{I}_{4z}\right)$$

$$\downarrow \pi J_{12}\tau_1$$

$$\downarrow \pi J_{13}\tau_1$$

$$\downarrow \pi J_{14}\tau_1$$

At this point the $\hat{I}$ terms will be dropped as they describe direct excitation in the observe channel and will not contribute to the transferred signal. In the NMR experiments they will either not be observable (because phase cycling eliminates the effects of direct excitation) or negligible compared to the hyperpolarized transferred signal, which is orders of magnitude stronger.

The free evolution period changes the $\hat{S}_{1y}$ density operator to

$$\begin{aligned}\hat{\rho}_3 = \cdots + \frac{1}{16}\mathbb{B}_S\{&\big[\big(\hat{S}_{1y}\cos\pi J_{14}\tau_1 - 2\hat{S}_{1x}\hat{I}_{4z}\sin\pi J_{14}\tau_1\big)\cos\pi J_{13}\tau_1 \\ &- 2\big(\hat{S}_{1x}\cos\pi J_{14}\tau_1 + 2\hat{S}_{1y}\hat{I}_{4z}\sin\pi J_{14}\tau_1\big)\hat{I}_{3z}\sin\pi J_{13}\tau_1\big]\cos\pi J_{13}\tau_1 \\ &- 2\big[\big(\hat{S}_{1x}\cos\pi J_{14}\tau_1 + 2\hat{S}_{1y}\hat{I}_{4z}\sin\pi J_{14}\tau_1\big)\cos\pi J_{13}\tau_1 \\ &+ 2\big(\hat{S}_{1y}\cos\pi J_{14}\tau_1 - 2\hat{S}_{1x}\hat{I}_{4z}\sin\pi J_{14}\tau_1\big)\hat{I}_{3z}\sin\pi J_{13}\tau_1\big]\hat{I}_{2z}\sin\pi J_{12}\tau_1\,\} + \cdots\end{aligned}$$

Using $J_{12} = J_{13} = J_{14} = J$ and ordering the terms yields

$$\begin{aligned}\hat{\rho}_3 = \cdots + \frac{1}{16}\mathbb{B}_S\big(&\hat{S}_{1y}\cos^3\pi J\tau_1 - 2\hat{S}_{1x}\hat{I}_{4z}\sin\pi J\tau_1\cos^2\pi J\tau_1 - 2\hat{S}_{1x}\hat{I}_{3z}\sin\pi J\tau_1\cos^2\pi J\tau_1 \\ &- 4\hat{S}_{1y}\hat{I}_{3z}\hat{I}_{4z}\sin^2\pi J\tau_1\cos\pi J\tau_1 - 2\hat{S}_{1x}\hat{I}_{2z}\sin\pi J\tau_1\cos^2\pi J\tau_1 \\ &- 4\hat{S}_{1y}\hat{I}_{2z}\hat{I}_{4z}\sin^2\pi J\tau_1\cos\pi J\tau_1 - 4\hat{S}_{1y}\hat{I}_{2z}\hat{I}_{3z}\sin^2\pi J\tau_1\cos\pi J\tau_1 \\ &+ 8\hat{S}_{1x}\hat{I}_{2z}\hat{I}_{3z}\hat{I}_{4z}\sin^3\pi J\tau_1\big) + \cdots\end{aligned}$$

Only $\hat{S}_{1x}\hat{I}_{\mathrm{n}z}$ terms can evolve into observable in phase $\hat{I}$ terms. These terms of interest have a maximum of $\frac{2}{3\sqrt{3}}$ for $\tau_1 = \left(\cos^{-1}\sqrt{2/3}\right)/(\pi\mathrm{J})$. We will set τ_1 to this optimal value and drop the unobservable terms.

$$\hat{\rho}_3 = \cdots - \frac{1}{16}\mathbb{B}_S\frac{2}{3\sqrt{3}}\big(2\hat{S}_{1x}\hat{I}_{2z} + 2\hat{S}_{1x}\hat{I}_{3z} + 2\hat{S}_{1x}\hat{I}_{4z}\big) + \cdots$$

$$\downarrow \left(\frac{\pi}{2}\right)_{-y}^{I} + \left(\frac{\pi}{2}\right)_{y}^{S}$$

$$\hat{\rho}_4 = \cdots - \frac{1}{16}\mathbb{B}_S\frac{2}{3\sqrt{3}}\big(2\hat{S}_{1z}\hat{I}_{2x} + 2\hat{S}_{1z}\hat{I}_{3x} + 2\hat{S}_{1z}\hat{I}_{4x}\big) + \cdots$$

$$\downarrow \pi_x^I + \pi_x^S$$

$$\hat{\rho}_5 = \cdots \frac{1}{16}\mathbb{B}_S\frac{2}{3\sqrt{3}}\big(2\hat{S}_{1z}\hat{I}_{2x} + 2\hat{S}_{1z}\hat{I}_{3x} + 2\hat{S}_{1z}\hat{I}_{4x}\big) + \cdots$$

The anti-phase terms evolve over $\tau_2 = \frac{1}{2J}$ into in phase $\hat{I}$ terms.

$$\downarrow \pi J_{12}\tau_2$$

$$\downarrow \pi J_{13}\tau_2$$

$$\downarrow \pi J_{14}\tau_2$$

$$\hat{\rho}_6 = \cdots \frac{1}{16}\mathbb{B}_S \frac{2}{3\sqrt{3}}\left(\hat{I}_{2x} + \hat{I}_{3x} + \hat{I}_{4x}\right) + \cdots$$

Comparing $\hat{\rho}_6$ with $\hat{\rho}_1$ shows, that the polarization of each I spin is now proportional to the S spins Boltzmann factor times a factor $\frac{2}{3\sqrt{3}} \cong 0.385$. This is remarkable, since it is more than 1/3 of the original S spin polarization. Hence, under thermal conditions, transfer from the S spins gives an I spins polarization corresponding to $\frac{2}{3\sqrt{3}}\frac{\mathbb{B}_S}{\mathbb{B}_I}$ times their original intensity. This result was confirmed with a simulation where the maximum appeared, as predicted, at $\tau_1 = \left(\cos^{-1}\sqrt{2/3}\right)/(\pi \mathrm{J})$. When relaxation was included in the simulations, the optimal τ_1 is slightly (<5 ms) shorter (Figure 2-4). Finally, a reverse INEPT sequence was simulated with the optimal delays, without taking relaxation into account (Figure 2-5).

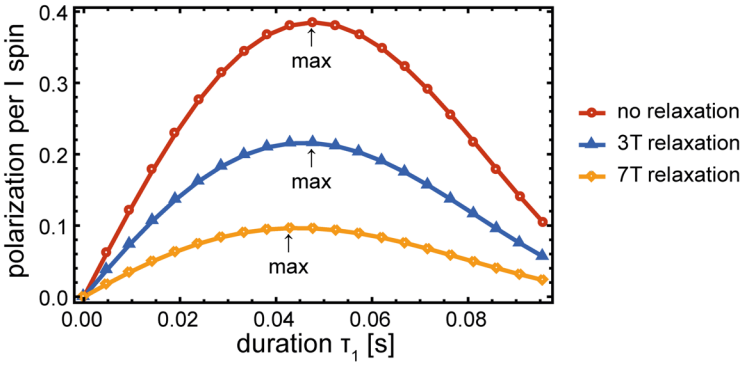

Figure 2-4. I$_3$S S→I INEPT transfer for different τ_1 (J = 4.1 Hz). The maximum occurs at $\tau_1 = \left(\cos^{-1}\sqrt{2/3}\right)/(\pi \mathrm{J})$. The simulations that included relaxation were performed using the following published values for T_1 and T_2 at 3T and 7T: T_2^{13C} (7T)=300 ms [83], T_2^{13C} (3T)=520 ms [21], T_2^{1H}(7T)=100 ms [84], T_2^{1H} (3T)=256 ms [85], T_1^{13C} (3T)=45 s [59] and T_1^{1H} (4.7T)=1.73 s [86]. The optimal value for τ_1 does not seem to change.

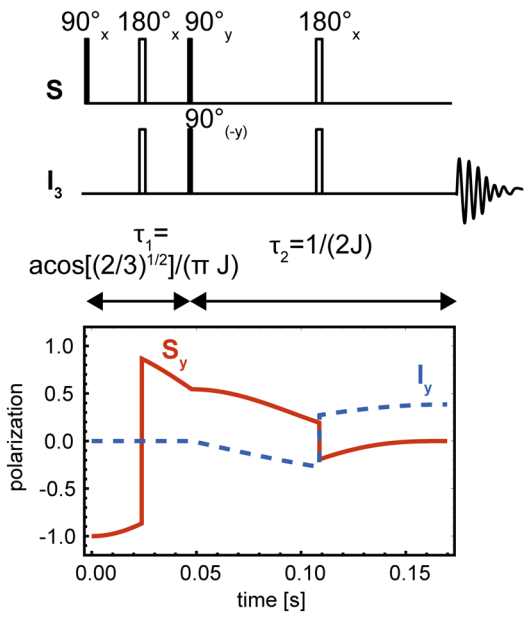

Figure 2-5. Adjusted timing in the I_3S S→I INEPT. Polarization from one S spin is transferred into the three magnetically equivalent I spins. Each I spin receives ~38.5 % of the initial S spin polarization.

2.2.3 Measuring enzyme kinetics using INEPT

Since the aim of this work was to get information about the kinetics of pyruvate to lactate conversion from repeated polarization transfer acquisitions, rather than just acquiring one snapshot of the reaction, it was important to develop a strategy for dynamic acquisition.

The INEPT sequence uses several 90° and 180° pulses. If hard pulses were used, the sequence would destroy the hyperpolarization in one shot. The sequence was therefore made frequency selective. In this way the hyperpolarization of only the targeted nuclei is disturbed, while the polarization of nuclei with significantly different chemical shift will be unaffected.

During the conversion of hyperpolarized [1-^{13}C]pyruvate to [1-^{13}C]lactate, only the [1-^{13}C]lactate resonance is excited and the [1-^{13}C]pyruvate polarization left undisturbed. Since lactate is formed continuously from pyruvate, each repeated acquisition gives a signal of the lactate newly formed since the last excitation. With such a spectrally selective reverse INEPT one could therefore get a lactate signal that corresponds to $\frac{\Delta M_L}{\Delta t}$, where Δt is the time between excitations. Such a pulse sequence could not be used for saturation-recovery [87] or other popular

fitting methods[88,89], because all these methods depend on measurement of the pyruvate as well as the lactate signal.

As an alternative I suggest fitting the general solution

$$S_L \propto \frac{\Delta M_L}{\Delta t} \cong \frac{\mathrm{d}M_L(t)}{\mathrm{dt}} = k_{PL} M_P(t=0) \mathrm{e}^{-(k_{PL}+1/T_{1P})\mathrm{t}}$$

of the saturation-recovery exchange model[87]

$$\frac{\mathrm{d}M_L(t)}{\mathrm{dt}} = k_{PL} M_P(t)$$
$$\frac{\mathrm{d}M_P(t)}{\mathrm{dt}} = -\left(k_{PL} + \frac{1}{T_{1P}}\right) M_P(t)\,.$$

to the time development of the lactate peak integral of the acquired spectra.

In contrast to using the pyruvate/lactate ratio this method relies purely on lactate signal acquisition. The decay of the signal over time depends on the first order rate constant and the relaxation time of the pyruvate pool T_{1P}. On a logarithmic scale the slope gives the sum of the rate constant and pyruvate relaxation rate, $1/T_{1P}$. The rate constant is expected to be lowered if the enzymatic activity decreases, while the T_{1P} time is expected to remain the same. Therefore, the slope in a logarithmic plot should be decreased as a result of a reduced enzymatic activity, induced for example by successful treatment. As a first indicator, the half-life of the lactate signal could be used to compare two datasets.

2.2.4 Pulse design

The [1-^{13}C] resonances of pyruvate and lactate at 14.1 T are 1850 Hz apart. This is enough to excite one of them without disturbing the other using a spectrally selective pulse. For the 90° excitation a 7.1 ms Gaussian shaped pulse was used. For inversion a 10 ms HS8 adiabatic inversion pulse with a bandwidth of 1000 Hz was used, as described by Garwood *et al.* [46]. The pulses were preinstalled on the spectrometer.

2.3 Experimental methods

2.3.1 Model systems

To demonstrate the suitability of the proposed polarization transfer pulse sequences for observing [1-^{13}C]pyruvate and NADH to [1-^{13}C]lactate and NAD+ conversion, different model systems were used. We went from a simple system to more complex models:

1. NMR spectroscopy on [1-^{13}C]lactate at thermal polarization levels,
2. Time resolved NMR spectroscopy with hyperpolarized [1-^{13}C]pyruvate in a solution of LDH and the coenzyme, NADH,
3. Dynamic *in vivo* MRI measurements in an animal tumour model (work performed by Jiazheng Wang).

2.3.2 The spectrometer

All NMR experiments were performed using a 600 MHz spectrometer with a 10 mm BBO probe (both from BRUKER). The inner coil of this probe was tuned to ^{13}C. The outer coil is optimized for ^{1}H excitation and observation. In the work shown here the temperature was set to 37 ^{o}C.

2.3.3 Non-hyperpolarized NMR

To demonstrate feasibility, experiments with a thermally polarized [1-^{13}C]lactate sample were performed (37 ^{o}C). Transfer of polarization was demonstrated from proton to carbon resonances in acquisitions with two averages, with phase cycling, and a repetition time TR = 300 s to allow full relaxation. Transfer from carbon to proton was demonstrated in acquisitions of 32 averages with TR = 300 s. The ^{1}H to ^{13}C as well as the ^{13}C to ^{1}H spectra were acquired into 16284 points with a sweep width of 6009 Hz. In each case a reference 90° pulse-acquire spectrum was recorded with the same settings and the same number of averages in order to quantify the transferred polarization. For the first demonstration of the pulse sequences developed here, a 10 mm NMR tube was prepared with 4 ml of 40 mM [1-^{13}C]lactate, 5% D_2O was added to allow automatic shimming and locking. The spectra observed with the reverse

INEPT sequence show signal originating from direct excitation of the observed nuclei. When used in thermal acquisitions, where the transferred signal in ^{13}C to ^{1}H experiments is small, especially when compared to the water signal, the INEPT sequence was performed with phase cycling, where in every other acquisition the phase of the initial 90° pulse and receiver phase were shifted by 180°. This cancels signal from direct excitation when averaging the signal from an even number of scans.

2.3.4 Hyperpolarized NMR

To 5 g of [1-^{13}C]pyruvic acid, 83.5 mg of the radical OX063 were added. This corresponds to a concentration of 15 mM OX063. Before each experiment a sample for polarization was prepared from this solution. To 44 mg of the solution (~36 µl), 1 µl of 1:10 Dotarem solution was added. The solution was vortexed and centrifuged. The molar concentration of pyruvate in the sample was 14 M. For a final pyruvate concentration of 75 mM, in each experiment 6 ml of the following dissolution buffer (pH 7.2) was used: 40 mM Hepes, 94 mM NaOH, 30 mM NaCl and 100 mg/L EDTA.

The pyruvate sample was inserted into a *HyperSense* polarizer (Oxford Instruments, Abingdon, UK), where it was exposed to very low temperature (~1.2 K) and a high magnetic field of 3.35 T. Microwave irradiation was performed at 94.12 GHz. For pyruvate, the time to build up the polarization was 45 min or more. The pyruvic acid sample was then dissolved in 6 ml of the dissolution buffer described above, which had been heated to ~180ºC at ~10 bar.

The plastic tube delivering the hyperpolarized sample was mounted on a rail with several permanent magnets attached to preserve the polarization during substrate delivery. At the end of the delivery system the substrate was collected in a sample tube. A 2 ml portion of the solution was then loaded into a syringe and injected via a 0.58 mm inner-diameter plastic tube into the NMR tube with the cell suspension or enzyme solution residing in the spectrometer magnet. Acquisition of spectra (16284 points, sweep width = 6009 Hz, TR = 2 s) was started and then the substrate was injected.

To evaluate the kinetic model, experiments with known amounts of purified Lactate dehydrogenase (LDH) enzyme were performed. Varying the amount of enzyme influences the rate constant and could be used to evaluate the kinetic model, as in Daniels *et al.*[89].

For these experiments a buffer (pH 7.2) was prepared with 120 mM Tris, 100 mM nicotinamide adenine dinucleotide in the reduced form (NADH) to facilitate the pyruvate to lactate conversion, and 10 mM Tetramethylsilane (TMS) as internal standard. Shortly before the experiments were started, the desired amount of enzyme was added to the buffer in the NMR tube. A stock enzyme solution had been prepared containing 2000 U LDH from rabbit muscle (Sigma Aldrich, Gillingham, UK), 1 ml glycerol and 1 ml solution (pH 7.0) containing 20 mM Hepes, 200 mM KCl, 0.1 mM EDTA. The total volume (LDH stock solution plus buffer) per NMR experiment was 4 ml.

2.4 Experimental results

2.4.1 Thermal polarization transfer

The efficiency of the spectrally selective INEPT sequence was evaluated by comparing the thermal INEPT spectra to spectra acquired using a simple pulse and acquire sequence. For the I to S (3,3,3-$^{1}H_3$→1-^{13}C) transfer the sequence described in section 2.1.2 and Figure 2-2b was executed with τ_1=121.951 ms and τ_2= 47.7837ms. For the S to I (1-^{13}C → 3,3,3-$^{1}H_3$) transfer τ_1 and τ_2 were swapped, as described in section 2.2.2 and Figure 2-5.

The peak integrals in these spectra are summarized in Table 2-1. The spectra are shown in Figure 2-6 and in Figure 2-7. The measured INEPT signal for 1-^{13}C → 3,3,3-$^{1}H_3$ transfer was 0.068 times the intensity of the signal acquired using a 90° pulse acquire acquisition, which corresponds to 70% of the theoretical maximum possible polarization transfer. The 30% loss is caused by relaxation during the total echo time of 141.42 ms.

Table 2-1. Peak integral values (*Int*) from the spectra shown in Figure 2-6 and in Figure 2-7 relative to 90° pulse acquire acquisitions for INEPT transfer at thermal equilibrium.

	(3,3,3-$^{1}H_3$→1-^{13}C)	(1-^{13}C → 3,3,3-$^{1}H_3$)
$(Int/ Int_{90°})_{meas}$	2.473	0.068
$(Int/ Int_{90°})_{theo}$	4.592	0.097
$\frac{(Int/Int_{90°})_{meas}}{(Int/Int_{90°})_{theo}}$	53.9%	70.3%

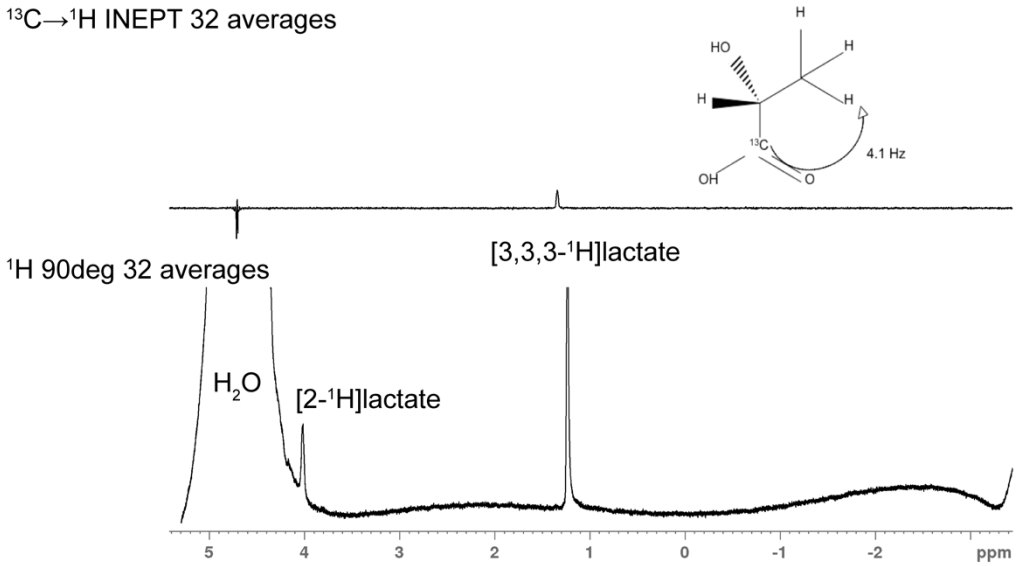

Figure 2-6. Polarization transfer spectrum from [1-^{13}C]lactate compared to a 90° pulse acquire spectrum. Top: 1-^{13}C→3,3,3-$^{1}H_3$ transfer using I_3S S→I INEPT. Bottom: 90° pulse acquire ^{1}H reference spectrum.

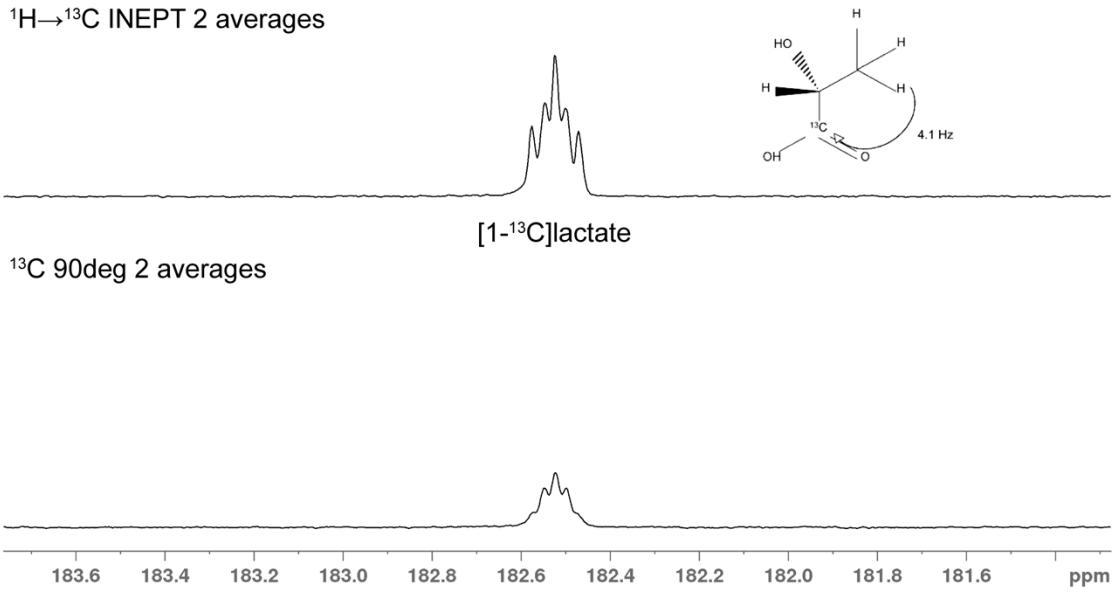

Figure 2-7. Polarization transfer spectrum of [1-^{13}C]lactate compared to a 90° pulse acquire spectrum. Top: 3,3,3-$^{1}H_3$→1-^{13}C transfer using I_3S I→S INEPT. Bottom: 90° pulse acquire ^{13}C reference spectrum.

2.4.2 Hyperpolarized [1-^{13}C]pyruvate in a solution containing LDH and the coenzyme

Two 10 mm NMR tubes were prepared containing 600 U and 900 U LDH. The I_3S S→I INEPT experiment was tuned for 1-^{13}C → 3,3,3-$^{1}H_3$ transfer in [1-^{13}C]lactate. Acquisitions with *TR* = 2 s were started shortly before injecting the hyperpolarized [1-^{13}C]pyruvate. The build-up of hyperpolarized lactate could clearly be observed (Figure 2-8). When the injection had finished, the lactate signal shows a simple exponential decay (Figure 2-9).

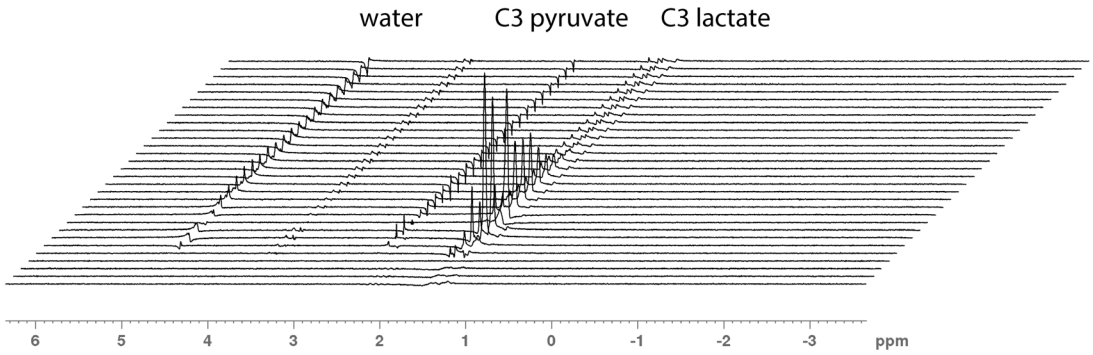

Figure 2-8. Spectra acquired every 2 s with the I_3S S→I INEPT sequence tuned for 1-^{13}C → 3,3,3-$^{1}H_3$ transfer in lactate following the addition of hyperpolarized [1-^{13}C]pyruvate to a solution containing 600 U LDH.

2.4.3 Calculation of reaction kinetics from transferred signal

To compare the decay rate for different amounts of enzyme the signal intensities corresponding to a specific enzyme concentration have been scaled in such a way that the first point of the exponential decay (start of linear decrease in a log plot) corresponds to 1 (Figure 2-9). For the two different enzyme concentrations the slopes of the decay were:

$$\log(S_L^{600\ U\ LDH})/t = 0.026 \pm 0.001\ s^{-1}$$

$$\log(S_L^{900\ U\ LDH})/t = 0.038 \pm 0.003\ s^{-1}.$$

The stated error is the error of the fit.

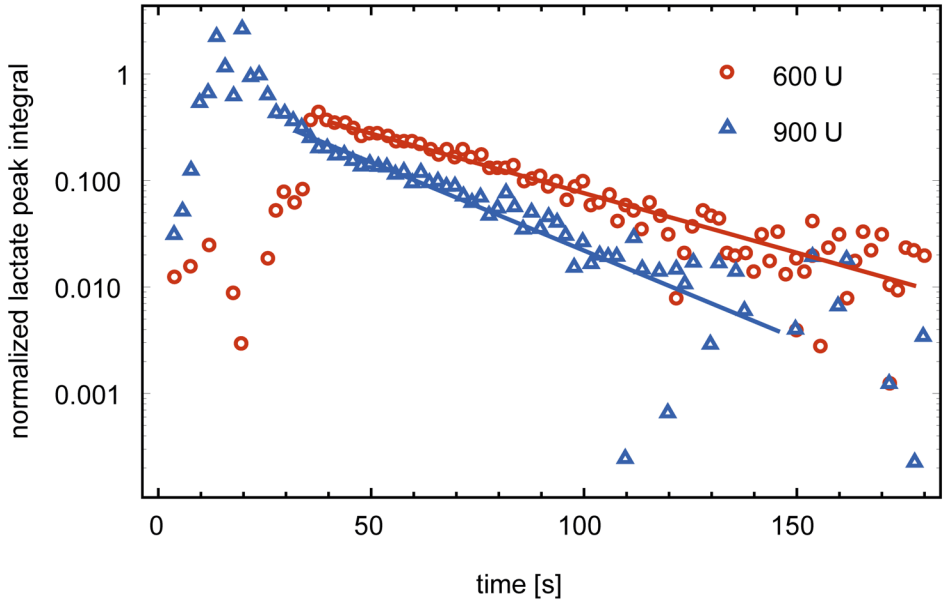

Figure 2-9. The decay rate of the repetitively transferred lactate signal depends on the amount of LDH. The data sets have been scaled to set the start of the exponential decay to one. An exponential decay with an offset ($f(t)=A\ exp(-k\ t)+B$) was fitted to the data points acquired after the dissolution had settled and before the signal had vanished in the noise.

These results for the transfer using the spectrally selective I_3S S→I INEPT and a solution of the enzyme (Figure 2-8 and Figure 2-9) show that it is possible to use proton detected hyperpolarized ^{13}C to compare enzymatic activities. The expected ratio of the rates was 0.67 (600/900) which is matched by the observed ratio of 0.67 ± 0.06. The error is the propagated error of the fits.

Since the rate of the decay of the lactate signal (slope in logarithmic representation) correlates with the enzymatic activity, also the half-life of the lactate signal (the time it takes for the lactate peak integral value to reduce to 50% of its maximal value) must correlate with the enzyme concentration. This value could be used as a simple indication of changes in enzymatic activity, which is similar to the time-to-peak value used in ^{13}C acquisitions as a simple metric to avoid complicated curve fitting[89]. However, this will only work, when T_1 times in experiments to be compared are similar and the pyruvate input function *in vivo* does not interfere with the model's assumptions.

2.5 Conclusion

The theory of proton detected hyperpolarized ^{13}C NMR has been expanded for four spin systems with three magnetically equivalent spins. A spectrally selective inverse INEPT sequence was used to detect the methyl protons of [1-^{13}C]lactate in a hyperpolarized state without overlap from the water peak and without destroying the majority of the ^{13}C hyperpolarization, which was stored in [1-^{13}C]pyruvate.

Experiments have shown, that transfer close to the theoretically predicted values is achievable in NMR spectroscopic measurements with the adapted INEPT sequence. Ultimately a comparison of a ^{1}H spectrum after the transfer of ^{13}C hyperpolarization to a thermal ^{1}H spectrum of the same sample after the decay of the hyperpolarization would be worthwhile to definitely prove the enhancement by experiment. But owing to technical limitations this was not possible so far.

The proton detected changes in hyperpolarized [1-^{13}C]lactate concentration were correlated with enzyme concentration. If this dependency on enzyme activity is observable under *in vivo* conditions, a pre/post treatment comparison of a tumour model could be carried out and the clinical relevance of this method could be evaluated in the future.

2.6 Outlook

Jiazheng Wang[90], with my help, adapted the spectrally selective 4-spin reverse INEPT sequence for *in vivo* imaging (Figure 2-10). He implemented a reverse INEPT sequence with non-simultaneous pulses, which has consequently led to a long duration of the transfer block and resulted in poor efficiency of polarization transfer. Following our work, von Morze *et al.* have demonstrated polarization transfer using a clinical scanner[91]. While Wang *et al*. and Morze *et al.* have demonstrated implementation on pre-clinical and clinical scanners, an experimental gain in sensitivity has not yet been demonstrated. The spectrally selective reverse INEPT sequence can give information on the reaction kinetics, by storing the majority of the polarization in the pyruvate while repetitively probing the lactate that is produced from the pyruvate. However, it cannot transfer parts of the polarization. In chapter 4 a sequence will be introduced that can do true partial hyperpolarization transfer. This sequence will also be used to demonstrate experimentally that indirect detection has a sensitivity advantage when detecting hyperpolarized low gamma nuclei.

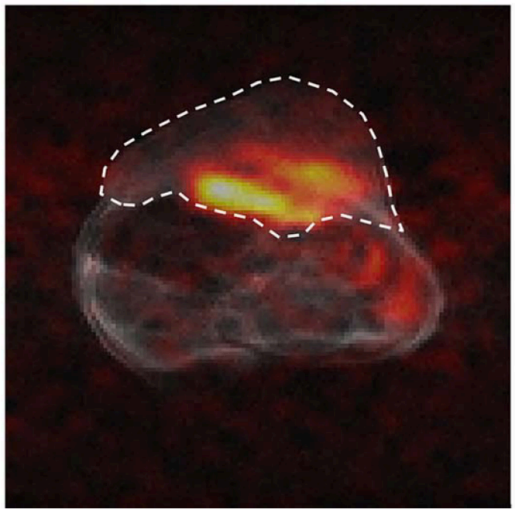

Figure 2-10. Proton detection of ^{13}C lactate in vivo. The first of a series of dynamic ^{1}H images of the lactate methyl protons acquired using the reverse INEPT sequence following injection of hyperpolarized [1-13C]pyruvate into a EL4 tumour-bearing mouse. The image was acquired 2 s after completion of the injection. The lactate image is rendered in false colour overlaid on a fast spin echo ^{1}H image of tissue water, which is in grayscale. The tumour is outlined. The figure is adopted from Wang et al. [90].

Chapter 3 RF coil development

Pulsing simultaneously on two channels, as is necessary for INEPT and similar sequences, is challenging for many popular MRI coil configurations, since they don't provide sufficient isolation between the two channels. These must be strongly decoupled in transmission mode in order to avoid damaging the low noise amplifiers or receivers. Most commercial coils provide this isolation by active detuning, but this solution renders simultaneous pulsing impossible.

The pre-clinical scanner used for the polarization transfer experiments presented in this thesis (chapter 4), was an Agilent 7 T scanner equipped with coils that could not support simultaneous pulsing at two different frequencies. I therefore constructed two dual-tuned RF coils that were tuned to protons and another lower frequency (either the resonant frequency of ^{13}C or ^{15}N). By allowing simultaneous pulsing these coils allowed implementation of more efficient polarization transfer sequences.

I also constructed a single loop ^{2}H surface coil for use on an Agilent 9.4 T system for deuterium metabolic imaging (DMI), as described in chapter 6. The development of this coil is also described here.

3.1 Introduction to RF coils

Mispelter *et al.* summarize the properties of a good RF coil as follows[92]:

"The NMR probe simply represents a fine interface along the border separating two different worlds: the macroscopic one and the world of tiny precessing nuclear spins. The probe should be able to accommodate different samples, from very small quantities to the entire human body, while being able to capture the spin's signals. It should produce a specific Radio Frequency (RF) magnetic field, as intense as possible, while being homogeneous over the largest possible

sample volume. It should simultaneously capture the signal from several types of spins, without any interference, and above all, it should be sensitive. These are, only in part, the general demands a user expects from an NMR head probe."

3.1.1 The resonator

In the simplest case, when observing a single nuclear spin population (i.e. a single isotope) in a small physical region, where coil inhomogeneities can be considered negligible, a single loop surface coil is sufficient to meet most expectations. The accessible region can be expanded by using adiabatic RF pulses[46].

The elements constituting this simple coil are a circular conductor (usually copper) resulting in an inductance (L) and a capacitor (C), in series with the loop. This simple LC-circuit (Figure 3-1) resonates at a frequency *f*, where $f = \frac{1}{2\pi\sqrt{LC}}$.

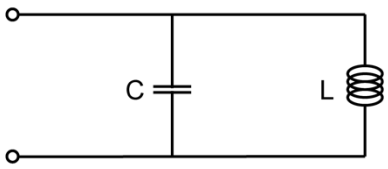

Figure 3-1. Simple LC-circuit.

In transmit mode, an alternating voltage is applied to the circuit terminals, causing an alternating magnetic field $\vec{B}_1(\vec{r}, t)$. In the classical picture, this field manipulates the magnetic moments of the nuclear spins. In the quantum mechanical picture, the field excites states of the spin system. In receive mode, the time-varying electromagnetic field generated by the precessing magnetization induces an electromotive force in the coil, which can be measured in the form of a voltage at the terminals of the resonant circuit. This signal is called the free induction decay (FID). The FID is quantized using an analogue-to-digital converter (ADC) and subsequently processed to produce spectra or images.

3.1.2 Tuning and matching

The magnitude of the $\vec{B}_1$ field is determined by the power of the RF amplifier and the characteristics of the RF coil. To maximize power transfer, a tuning and matching circuit, also called an impedance transformer, is inserted between the resonator and the cable coupling the coil to the amplifier. The purpose of this circuit is to match the impedance of the coil at the resonance frequency to the transmission line and amplifier, which have an impedance of 50 Ω. Satisfying this condition ensures the greatest transfer of power from the amplifier to the coil, thereby resulting in the highest possible B_1 field[93]. In an unmatched condition, a fraction of the power is reflected to the amplifier leading to decreased efficiency and in severe cases damage to the amplifier. When the resonator is loaded, it's input impedance changes. The load can be approximated as a resistance (R_d) and capacitance (C_d) in parallel to the coil's inductance (L). To accommodate different loads, the impedance transformer must be adjustable depending on the coil load. Practically, this is achieved using variable capacitors that can be trimmed to satisfy the matching condition for maximum power transfer. Changing the load as well as the value of the matching capacitor will also affect the coil's resonant frequency. As a consequence, the tuning capacitor is adjusted to ensure the coil resonates at the desired frequency. The simplest circuit that achieves tuning and matching for different loads is shown in Figure 3-2a.

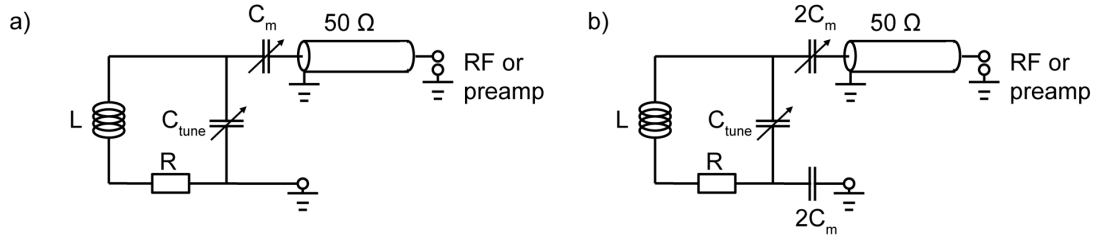

Figure 3-2. a) Simple RF coil circuit with tuning and matching capability. b) Balanced matching to reduce coil-to-ground losses.

A coil is prone to losses due to the paths of the electric fields that penetrate the sample. A large proportion of these losses can be described in a lumped model approximation with R_d and C_d in parallel to the coil (Figure 3-3). The influence of C_d is corrected for with the tuning capacitor (Figure 3-2a), while R_d causes irrecoverable losses.

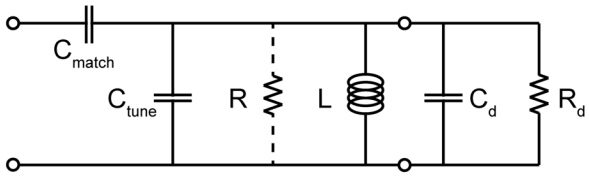

Figure 3-3. A probe circuit with standard tuning and matching and a lumped elements approximation of losses generated between the terminals of the coil (coil-to-coil losses). L is the inductance of the sample coil, C_{tune} and C_{match}, are the tuning and matching capacitors and R models the coil resistance. C_d, and R_d model the coil-to-coil parasitics. Figure adapted from Murphy-Boesch & Koretsky[94].

In addition to this, the electric field paths from the coil via the sample to the ground cause additional electric losses. By modifying the resonance circuit with an additional matching capacitor between the resonator and the ground (shielding) the current distribution across the terminals is balanced (Figure 3-2b). Consequently, the voltage between circuit elements is reduced, causing a reduction in the electric field while leaving the B_1 field unchanged. Thereby less E field penetrates the samples leading to reduced losses[94]. Furthermore, in multi-element coils, matching reduces common mode currents[95].

3.1.3 Sensitivity of RF coils

At room temperature, the RF coil is a significant source of thermal noise. The source of this noise can be summarized by the coil resistance R_{coil}. The task of the RF engineer is to minimize R_{coil} and thereby keep the overall resistance of the setup

$$R_{eff} = R_{sample} + R_{coil}$$

to a minimum.

A measure of coil sensitivity can be the determined by observing the resonator resistance in the unloaded state compared to the loaded state. A large change in resistance indicates a highly sensitive coil since this means that a large proportion of the total resistance originates from the sample and not from the coil. However, it is hard to measure that complex resistance directly, so instead one measures a value called the Q-factor. This Q-factor is the ratio of RF energy stored in the coil (W) and the energy lost (P_{loss}) over one period (T) of oscillation. It can be expressed in terms of other parameters involving the current (I), and coil specific parameters:

$$Q = \frac{W}{TP_{loss}} = 2\pi f \frac{W}{P_{loss}} = \omega \frac{LI^2/2}{RI^2/2} = \frac{\omega L}{R}.$$

In other words, the Q-factor characterizes the rate of energy dissipation in the resonance system. It is also related to the bandwidth of the frequency response:

$$Q = \frac{f}{\Delta f}.$$

This ratio of the resonance frequency *f* and the bandwidth of the reflected power at full width half maximum (3 dB attenuation), (Δf), can be measured with a network analyser. Since $Q=\omega L/R$, the ratio of the unloaded Q-factor to the loaded Q-factor is an indicator of the composition of the total resistance of the coil/sample combination. It is therefore also an indicator of coil sensitivity:

$$Q_{ratio} = \frac{Q_{unloaded}}{Q_{loaded}} = \frac{R_{Coil} + R_{Sample}}{R_{Coil}}.$$

The higher the Q_{ratio} the more sensitive the coil. When $Q_{ratio}>2$ sample noise dominates the overall noise and further improvements in the coil will have little influence on the overall noise.

3.2 Building a ²H surface coil for 9.4 T

The deuterium magnetic resonance frequency at 9.4 T is 61.44 MHz. For the project presented in chapter 6 it was necessary to build a coil that acquires ^{2}H signal from a subcutaneous EL4 tumour in a mouse. The tumour takes the form of a hemispherical lump on the back of the animal with a diameter of up to 14 mm. In order to obtain a high filling factor, a surface coil with a matching diameter is ideal. Such a coil was built using copper wire with a thickness of 1.25 mm, two variable non-magnetic capacitors (model NMAP40HVE, Voltronic) and non-magnetic chip capacitors (American-Technical-Ceramics) mounted on a matrix board. The circuit was laid out with copper tape. The variable matching capacitor was balanced with a non-variable chip capacitor against the shielding of the cable, which was assumed to be grounded. The circuit is equivalent to the one shown in Figure 3-2b. Tuning on the bench was achieved by iteratively changing capacitors until the desired frequency was reached. Tuning

and matching in the magnet was achieved with plastic rods mechanically coupled to the variable capacitors and accessed via the magnet bore.

The Q_{ratio} of this resonator was measured on the bench. The loading caused by a tumour bearing mouse was mimicked with a 2 ml saline phantom. The average and standard error of three independent measurements with a network analyser (DG8SAQ USB-Controlled VNWA 3EC, SDR-Kits) were

$$Q_{ratio} = (1.1 \pm 0.2)\,.$$

This value indicates, that coil noise is dominant in this coil/sample combination. For low frequencies and small coils, this is not a surprise. Kumar *et al.* have simulated the noise of single loop coils as a function of frequency and loop size. They calculated the noise figure corresponding to a Q_{ratio} of 2.0 for a 30 mm diameter single loop 64 MHz resonator.[96] They also found a strong trend towards a higher noise figure and therefore lower Q_{ratio} when reducing the coil diameter, which suggests that we should get a Q_{ratio} lower than 2.0 for our coil.

3.3 Building double-resonant $^{1}H/^{13}C$ and $^{1}H/^{15}N$ surface coils for 7 T

To implement INEPT-type polarization transfer sequences with simultaneous pulses new RF coils were required. The coils were designed to operate at the proton frequency at 7T (~299 MHz) and one lower frequency, which was either the ^{13}C frequency (~75 MHz) or the ^{15}N frequency (30 MHz). Two double-tuned coils were built one for $^{1}H/^{13}C$ and one for $^{1}H/^{15}N$.

Initially the Adriany-Gruetter coil design[97] was preferred. This is the most popular design for dual-tuned surface coils and has many applications in multinuclear *in vivo* NMR[76,98–100]. It consists of two outer coils in quadrature mode tuned to the proton frequency and one coil closer to the sample tuned to the lower frequency. This coil provides excellent isolation between the channels via geometric decoupling. It is also relatively easy to build since essentially it consists of three simple surface coils arranged in a specific spatial configuration. However, the excitation profile at the x-nuclei and proton frequencies are very different due to the different positions of the loops. After a few initial trials, this design was rejected. For polarization

transfer, the low and high frequency B_1-fields need to be similar in shape and strength. This is not the case for the Adriany-Gruetter coil because it uses different resonators at different relative positions. Instead, a coil that uses only a single resonator to excite the two frequencies was chosen. Such designs are possible when frequency dependent current paths are exploited to make a single structure resonate at different frequencies. The publication by Wetterling *et al.*[101] describes the construction of such a coil.

The construction and working principle of the $^{1}H/^{15}N$ coil is described in the following. The $^{1}H/^{13}C$ coil was built in exactly the same way but with different capacitors.

To understand the double-tuning capability of the circuit, one must find the frequency-dependent current paths determined by the capacitive and inductive impedances at 30 MHz and at 300 MHz, which correspond to the ^{15}N and ^{1}H frequencies at 7 T, respectively. In the circuit sketched in Figure 3-4a, at 300 MHz, the impedance of the ^{15}N capacitor ($C_{15N} = (C_{15N1}{}^{-1} + C_{15N2}{}^{-1})^{-1} = 80$ pF) is $j6.6\ \Omega$ compared to $j113\ \Omega$ for C_{Tr} (4.7 pF) and $j(38\text{-}113)\ \Omega$ for L_{Tr} (estimated at 20 to 60 nH). That means that at this high frequency, the capacitor C_{15N} which defines the lower resonant frequency can be neglected. Therefore, the circuit at 300 MHz (Figure 3-4a) can be simplified to a circuit where only L_{Det}, L_{Tr}, $C_H = (C_{H1}{}^{-1} + C_{H2}{}^{-1})^{-1}$ and C_{Tr} contribute. The resonance condition at 300 MHz of this simplified circuit is:

$$f_{300MHz} = \frac{1}{2\pi\sqrt{(L_{Det} \| L_{Tr})(C_H \| C_{Tr})}}$$

At the ^{15}N resonance frequency, 30 MHz, the impedance of $C_H = (C_{H1}{}^{-1} + C_{H2}{}^{-1})^{-1} = 5$ pF and $C_{Tr} = 4.7$ pF are each over $j\ 1000\ \Omega$. The impedance of the trap circuit however is only $j\ 4$ to $j\ 11\ \Omega$ ($L_{Tr} \sim 20$ to 60 nH). Therefore, C_H and C_{Tr} remain effectively open at the low frequency. The resonance condition of the circuit at 30 MHz can thus be approximated as

$$f_{30MHz} = \frac{1}{2\pi\sqrt{(L_{Det} + L_{Tr})C_{15N}}}.$$

The next challenge is to connect the amplifiers/receivers in such a way that there is minimal interference between the channels. In this coil design this achieved by connecting to frequency-specific null spots, also known as virtual grounds.

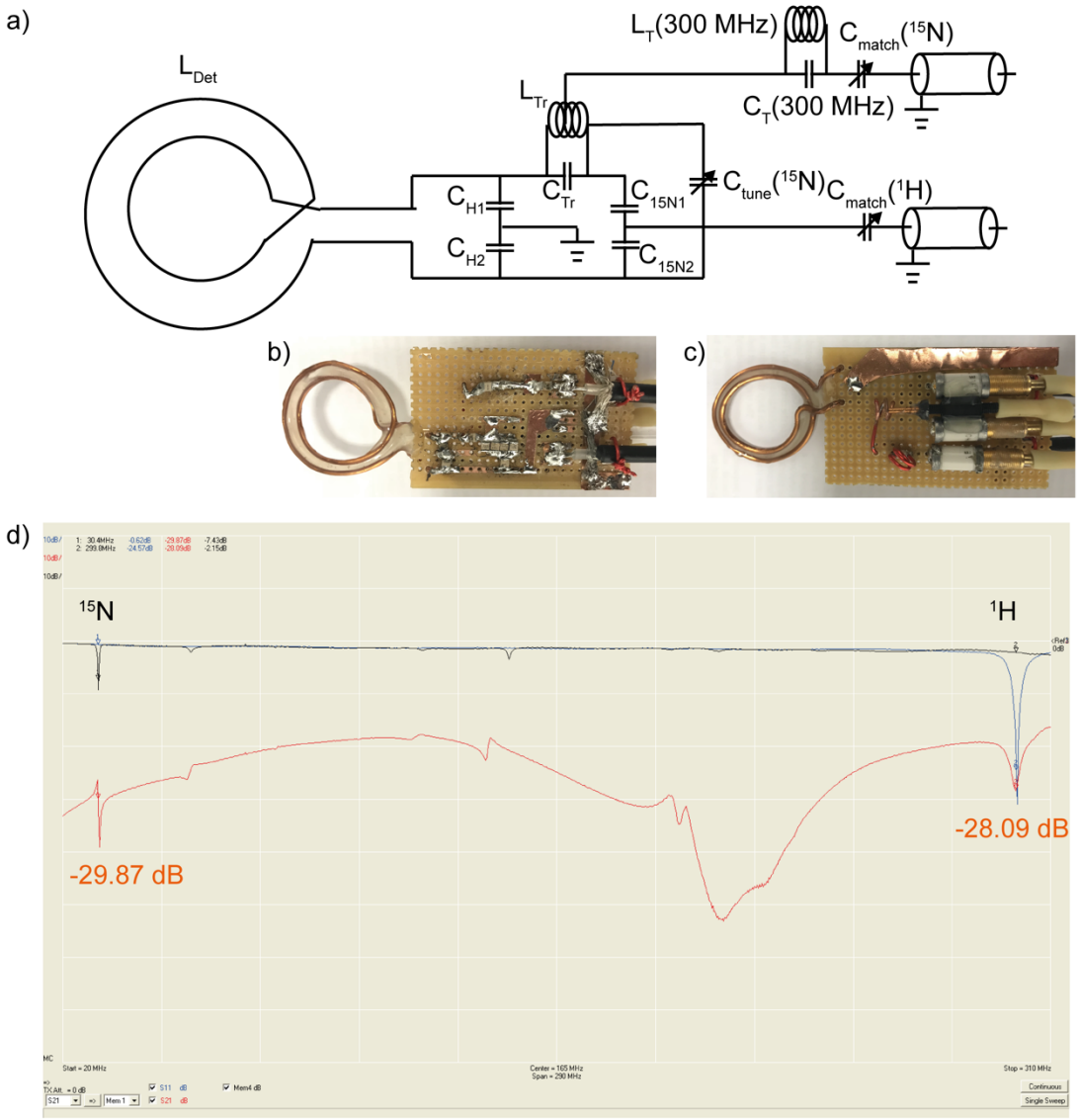

Figure 3-4. a) Circuit design for the double-tuned $^{15}N/^{1}H$ transceiver surface coil described by Wetterling *et al.*[101]. The capacitors had values of C_{H1} = 10 pF, C_{H2} = 10 pF, C_{Tr} = 4.7 pF, C_{15N} = 400 pF, C_{15N} = 200 pF, C_T (300 MHz) = 22 pF, $C_{Tune}(^{15}N)/C_{Match}(^{1}H)$ = 1.5…40 pF, $C_{Match}(^{15}N)$ = 20 pF+(1.5…40) pF. b) bottom side of the coil. This is the side facing the subject in MR experiments. c) Top side with connected tuning rods. d) Network analyser measurements of the coil loaded with a saline phantom. Black line: S_{11} reflected power ratio measured on the ^{15}N connector; blue line: S_{22} reflected power ratio measured on the ^{1}H connector; red line: S_{12} (transferred power) measured between the ^{15}N and the ^{1}H connector.

The complete $^{1}H/^{15}N$ coil circuit design is shown in Figure 3-4a and a photograph of the finished coil is shown in Figure 3-4b and c. The good isolation between the channels at the

two frequencies can be seen in the network analyser measurement (Figure 3-4d). With an attenuation of over 25 dB between the channels, this coil is suitable for simultaneous pulsing at the low and high frequencies without damaging the amplifiers. The next chapter shows that this coil as well as the $^{1}H/^{13}C$ coil built following the same principles[101] were very useful for polarization transfer experiments.

Chapter 4 Increasing the sensitivity of hyperpolarized [$^{15}N_2$]urea detection by serial transfer of polarization to spin-coupled protons

---

The text and figures in this chapter have been submitted for publication in a similar or identical form in

Kreis F, Wright AJ, Katz-Brull R, Brindle KM. Increasing the sensitivity of hyperpolarized [$^{15}N_2$]urea detection by serial transfer of polarization to spin-coupled protons. *Magn Reson Med.* under review.

My contribution to this publication was the design of the study, developing and simulating the pulse sequence, performing the experiments, analysing the data and writing the manuscript.

In chapter 2 we used the most popular molecule for hyperpolarization experiments, [1-^{13}C]pyruvate to demonstrate proton detection via polarization transfer. However, there are many other isotopes and molecules that can be polarized and in which this technique could be demonstrated. The following text presents work using hyperpolarized [$^{15}N_2$]urea. The ^{15}N nucleus has a very low γ (2.5 times lower than ^{13}C). Polarization transfer experiments, where the sensitivity is not defined by the γ of the hyperpolarized ^{15}N but by the γ of the spin-coupled protons, could increase the sensitivity of detection of the nucleus by an order of magnitude.

4.1 Introduction

Magnetic resonance imaging of hyperpolarized isotopically-labelled substrates has enabled measurements of metabolic fluxes, pH and tissue perfusion *in vivo*. The most commonly used label has been ^{13}C because of its relatively long polarization lifetime and the availability of ^{13}C-labelled substrates suitable for investigating metabolism[102]. Hyperpolarized ^{15}N-labelled substrates have also been investigated, as agents for assessing tissue perfusion (urea[103] and glutamine[104]) and as pH probes (pyridine derivatives)[105]. ^{15}N-labelled substrates have the advantage of very long hyperpolarization lifetimes, up to 200 s [103], and more when kept in $^{2}H_2O$. However, the 2.5-fold lower gyromagnetic ratio when compared to ^{13}C (10-fold lower when compared to ^{1}H) results in lower magnetization and precession frequency, and therefore lower sensitivity of detection. For imaging there is also the requirement for larger gradients.

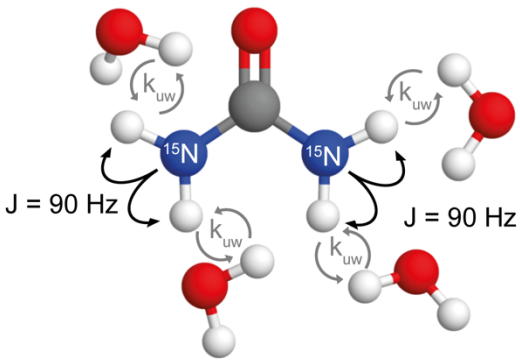

Figure 4-1. Structure of [$^{15}N_2$]urea. The coupling constant between ^{15}N and the directly bonded protons is -90 Hz. These protons are in exchange with solvent water.

Detection sensitivity can be improved, while still benefiting from the long ^{15}N polarization lifetime, by transferring the hyperpolarization from ^{15}N to ^{1}H immediately before signal acquisition using sequences such as INEPT[75]. Reverse INEPT-type sequences have been used previously with hyperpolarized ^{13}C-labelled substrates to produce hyperpolarized proton spectra[76,79,82,91] and images[90,106] and with hyperpolarized ^{15}N labelled substrates to produce spectra[77,78,107]. In all of these INEPT-based experiments 100% of the available polarization

was used in a single acquisition. To obtain dynamic information the hyperpolarization of the low γ nucleus must be sampled in discrete packets. Harris *et al.*[77] used spatially selective coherence transfer to probe different regions of the sample at different times. Barb *et al.* exploited chemical exchange of deuterons in hyperpolarized $^{15}ND_2$-amido-glutamine with solvent protons to acquire a series of proton spectra from the protonated isotopologue[107]. Dzien *et al.*[82] utilized spontaneous $^{13}C \rightarrow {}^{1}H$ cross-relaxation to detect, in a series of dynamically acquired proton spectra, the production of acetaldehyde from hyperpolarized [U-$^{2}H_3$,2-^{13}C]pyruvic acid, in the reaction catalysed by pyruvate decarboxylase. We have previously described a spectrally-selective reverse INEPT sequence in which ^{13}C hyperpolarization in lactate, which had been produced in a tumour from injected hyperpolarized [1-^{13}C]pyruvate, was transferred to the methyl protons and imaged[90]. The fully depleted [1-^{13}C]lactate hyperpolarization was replenished after each transfer by further lactate production from the injected pyruvate. However, to the best of our knowledge, no one has yet demonstrated experimentally partial transfer of hyperpolarization from a low γ to a high γ nucleus, while maintaining the majority of the hyperpolarization in the low γ nucleus. I demonstrate here partial transfer of ^{15}N hyperpolarization in [$^{15}N_2$]urea to urea protons, in consecutive acquisitions, and subsequent imaging of these protons.

4.2 Methods

4.2.1 Solvent exchange of the urea protons

The exchange rate in a 100 mM [$^{15}N_2$]urea solution was measured at neutral pH using a 14.1 T NMR spectrometer equipped with a 5 mm BBI probe (Bruker Spectrospin Ltd.). The water proton resonance was saturated for between 0.1 to 2.6 s and then spectra acquired using a 90° pulse and a bandwidth of 6000 Hz into 8192 complex points. The exchange rate was calculated as described in[108].

4.2.2 Relaxation times

Relaxation times were measured on an Agilent 7 T pre-clinical scanner (Agilent, Palo Alto, California, USA) using a home-built single turn double-tuned $^{1}H/^{15}N$ transmit/receive surface

coil[101] with an inner diameter of 14 mm. The same coil was used for polarization transfer experiments. The sample contained 3 ml of 1 M [$^{15}N_2$]urea in phosphate-buffered saline (PBS) and 300 µl ^2H_2O at 20 °C. T_1 relaxation times were measured with an inversion recovery sequence (n = 1, TR_{1H} = 10 s, TR_{15N} = 100 s). The time between the 90° and 180° pulses was varied between 0.25 s and 8 s for the ^{1}H measurements and between 2.5 s and 80 s for the ^{15}N measurements. T_2 relaxation times were measured with a Carr-Purcell-Meiboom-Gill (CPMG) sequence (n = 1, TR_{1H} = 10 s, TR_{15N} = 100 s). The minimum echo time for the ^{1}H measurements was 0.0125 s, which was increased by iteratively adding more spin echo sandwiches while leaving the inter echo spacing the same until, over six acquisitions, the maximum TE of 0.4 s was reached. For ^{15}N T_2 measurements the TE was varied between 0.0624 s and 2 s.

4.2.3 Dynamic nuclear polarization

Samples were prepared from 45.9 mg [$^{15}N_2$]urea, 2.31 mg OXO63 radical, 62.8 mg ^2H_2O and 55.4 mg glycerol. The mixture (37.5 mg) was polarized for at least 3 h in a *HyperSense* polarizer (Oxford Instruments) using microwave irradiation at 94.110 GHz. Dissolution was performed in 6 ml ^2H_2O. [^{13}C]urea was hyperpolarized as described by von Morze *et al.*[14]. The [^{13}C]urea preparation contained 6.4 M [^{13}C]urea and 23 mM OXO63 trityl radical in glycerol. The preparation (29.4 mg) was polarized at 94.095 GHz and dissolved in 6 ml PBS to give the same [^{13}C]urea concentration as in the [^{15}N]urea dissolution.

4.2.4 Polarization measurements

Spectra were acquired using a 90° pulse and a sweep width of 20 kHz into 16384 complex points from 4 ml of hyperpolarized urea using a 14.1 T NMR spectrometer and a 10 mm BBO probe (Bruker Spectrospin Ltd.) at room temperature. The SNR was compared to that of spectra of the same solution after decay of the hyperpolarization. For these experiments, measurements at thermal equilibrium from [^{13}C]urea were acquired with a TR of 225 s and were the sum of 237 averages. For [^{15}N]urea the TR was 1000 s and 32 averages were acquired. The thermal polarization:

$$P_{thermal} = \tanh\left(\frac{\hbar\gamma B_0}{2k_B T}\right) \tag{4.1}$$

was calculated to be $4.87 \cdot 10^{-6}$ for ^{15}N and $12.08 \cdot 10^{-6}$ for ^{13}C, assuming a temperature of 300 K, where $\hbar$ is the reduced Planck's constant, γ the gyromagnetic ratio, k_B Boltzmann's constant and B_0=14.1 T. The hyperpolarization, P_{hyp}, was calculated from the SNRs of the hyperpolarized and thermal measurements using:

$$P_{hyp} = P_{thermal}\sqrt{n_{avg}}\frac{SNR_{hyp}}{SNR_{thermal}} \tag{4.2}$$

4.2.5 Measurement of coil performance

A cylindrical phantom containing 2 ml of 4 M [$^{15}N_2$]urea was placed through the loop of the double-tuned resonator and ^{1}H and ^{15}N spectra acquired with a sweep width of 10 kHz into 2048 complex points with one average using a 2 ms BIR4 90° pulse, with pulse shape parameters as described by Garwood *et al.*[47]. Coil performance at the ^{1}H and ^{15}N frequencies was assessed by comparing the SNRs of the two spectra.

4.2.6 A pulse sequence for partial hyperpolarization transfer

This was based on the BINEPT (B_1 insensitive nuclear enhancement through polarization transfer) sequence[109], which uses BIR4 adiabatic pulses[47]. A BIR4 pulse is composed of three sections; adiabatic half-passage in reverse, adiabatic inversion, and adiabatic half-passage. The flip angle is controlled by two phase jumps $\Delta\phi_1$ and $\Delta\phi_2$=-$\Delta\phi_1$ before and after the adiabatic inversion segment respectively. The transformation induced by a BIR4 pulse can be described using a composite pulse analogy, where ($90°_y 180°_{(y+\pi+\theta/2)} 90°_y$) is analogous to a BIR4 pulse with phase jumps $\Delta\phi_1$= -$\Delta\phi_2$= $\pi+\theta/2$. Both the BIR4 pulse and this composite pulse execute a rotation of θ rad about the x-axis, although a composite pulse requires a considerably more uniform B_1 field to achieve this transformation. With this simplification, the BINEPT sequence can be written as:

S:[$90°_y$-τ_1-$180°_{(y+\pi+\delta/2)}$-τ_2-$90°_y$]-τ_3-[$90°_y 180°_{(y+3\pi/2)} 90°_y$]-$\tau_4$-

I:[$90°_y$-τ_1-$180°_{(y+\pi)}$-τ_2-$90°_y$]-τ_3-[$90°_y 180°_{(y+3\pi/2)} 90°_y$]- τ_4- Acq .

where the I spin is proton and the S spin ^{15}N. This is analogous to the BINEPT sequence in terms of net rotations, but the paths taken by the magnetization vectors differ. In this simplified sequence, the phase offset δ of the first 180° pulse on the S spin must be 90° and $\tau_{1\text{-}4}$ must be 1/(4 J) in order to fully transfer polarization from the S to the I spin in a two spin system. When τ_1 and τ_2 are shortened and the phase offset δ adjusted, some of the magnetization can be returned to the z-axis while still transferring some of the polarization. For a simple IS spin system the transferred polarization (P_I) is equal to $\sin(\delta)\sin(\pi J \tau)P_0$ and the polarization returned to the z-axis (P_S) is equal to $-\cos(\delta)\cos(\pi J \tau)P_0$, where P_0 is the original polarization, J is the coupling constant between the I and S spins and $\tau=2\tau_1=2\tau_2$ (see product operator analysis in section 4.2.7). In all cases, $\tau_3=\tau_4=1/(4\ J)$. For an I_NS spin system these terms are: $P_I=N\ \sin(\delta)\sin(\pi J \tau)$ and $P_S=-\cos(\delta)[\cos(\pi J \tau)]^N$. A similar approach has been described previously in the HINDER sequence (*h*yperpolarized *i*nsensitive *n*ucleus *d*elivers *e*nhancement *r*epeatedly)[110], where spin order is divided between I or S spin polarization by changing the phase, δ, of the second 90° pulse on the S spin and shortening the inter pulse delays in a classical INEPT sequence.

To summarize, we have combined the BINEPT and HINDER sequences to give an ImpeRfection RobUst Partial Transfer (IRRUPT) sequence, where δ and τ_1 and τ_2 in the BINEPT sequence can be adjusted to achieve partial polarization transfer. An additional 180° was added to δ *to* return the remaining magnetization to the positive instead of the negative axis (making $P_I=-\cos(\delta)[\cos(\pi J \tau)]^N$ positive). The delays between the pulses ($\tau_{1\text{-}4}$) and the additional phase offset δ in the segmented BIR4 pulse on the S spin were chosen as described for the HINDER sequence[110]. For two protons coupled with a 90 Hz coupling constant (J) to one low γ nucleus: $\tau_1 + \tau_2 = 0.442/(2\ \pi J) = 782\ \mu s$, $\tau_3 + \tau_4 = 1/(2\ J) = 5555\ \mu s$, $\delta = 18.050°$. The delays were not corrected for the fact that relatively long adiabatic pulses were used instead of hard pulses. With adiabatic pulses in the simulations the IRRUPT sequence transferred ~20% of the ^{15}N hyperpolarization to coupled (J_{NH} = -90 Hz) protons (Figure 4-2).

Each adiabatic half passage segment in the BIR4 pulse was 500 μs, giving a total pulse duration of 2 ms. The last BIR4 pulse in the sequence flips the proton magnetization onto the z-axis. Then, either a simple excitation pulse or a slice-selective 2D-single-shot echo-planar imaging (EPI) sequence was used for proton acquisition.

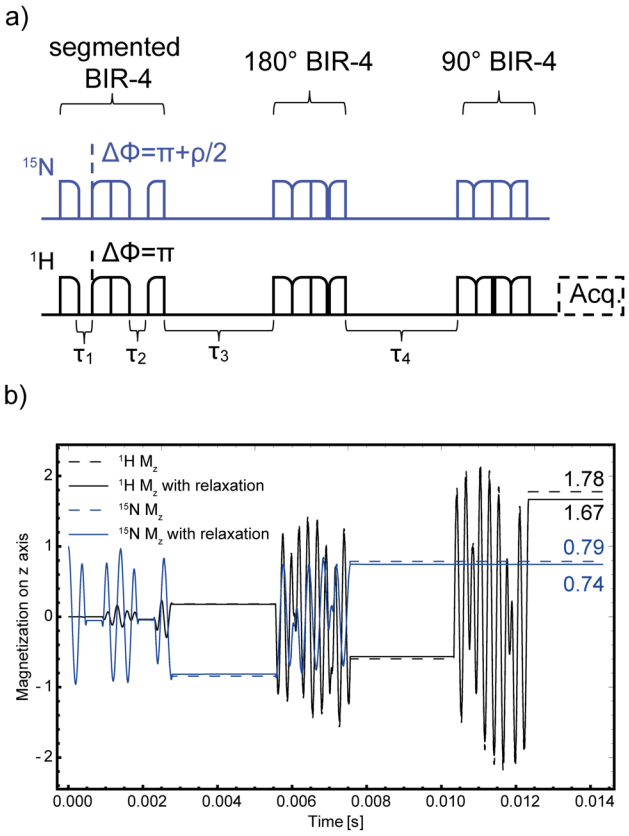

Figure 4-2. a) IRRUPT pulse sequence. b) Simulation of the IRRUPT polarization transfer pulse sequence, which is based on the BINEPT[109] and HINDER[110] sequences, with $\tau_1 + \tau_2 = 0.442/(2\,\pi\,J_{NH}) = 782$ µs, $\tau_3 + \tau_4 = 1/(2\,J_{NH}) = 5555$ µs, $\delta = 18.050°$. The sequence was simulated with a maximum B_1 amplitude of 2500 Hz for ^{15}N and 4000 Hz for ^{1}H.

4.2.7 Calculating the outcome of the IRRUPT sequence

The density operator $\hat{\rho}$ is calculated step by step in a composite pulse analog of the IRRUPT pulse sequence:

S: $[90°_y\text{-}\tau_1\text{-}180°_{(y+\pi+\delta/2)}\text{-}\tau_2\text{-}90°_y]\text{-}\tau_3\text{-}[90°_y 180°_{(y+\,3\pi/2)} 90°_y]\text{-}\tau_4\text{-}$

I: $[90°_y\text{-}\tau_1\text{-}180°_{(y+\pi)}\text{-}\tau_2\text{-}90°_y]\text{-}\tau_3\text{-}[90°_y 180°_{(y+3\pi/2)} 90°_y]\text{-}\,\tau_4\text{-}$ Acq

A two spin IS system with the Hamiltonian $\widehat{H} = 2\pi J\hat{I}_z\hat{S}_z$ was assumed for illustration. The calculations can be generalized to any I_NS system.

$$\hat{\rho}_1 = \mathbb{B}_I\hat{I}_z + \mathbb{B}_S\hat{S}_z$$

The polarization in the nuclei receiving the polarization is assumed to be zero ($\mathbb{B}_I = 0$) before the beginning of the pulse sequence, leading to

$$\hat{\rho}_1 = \mathbb{B}_S\hat{S}_z$$

$$\downarrow \left(\frac{\pi}{2}\right)_y^I + \left(\frac{\pi}{2}\right)_y^S$$

$$\hat{\rho}_2 = \mathbb{B}_S\hat{S}_x$$

$$\downarrow \pi J\tau/2$$

$$\hat{\rho}_3 = \mathbb{B}_S \cos\left(\pi J\frac{\tau}{2}\right)\hat{S}_x + 2\mathbb{B}_S \sin\left(\pi J\frac{\tau}{2}\right)\hat{S}_y\hat{I}_z$$

$$\downarrow (\pi)_{-y}^I + (\pi)_{y+\varphi/2}^S$$

$$\hat{\rho}_4 = -\mathbb{B}_S \cos(\Phi)\cos\left(\pi J\frac{\tau}{2}\right)\hat{S}_x + \mathbb{B}_S \sin(\Phi)\cos\left(\pi J\frac{\tau}{2}\right)\hat{S}_y - 2\mathbb{B}_S \sin(\Phi)\sin\left(\pi J\frac{\tau}{2}\right)\hat{S}_x\hat{I}_z - 2\mathbb{B}_S \cos(\Phi)\sin\left(\pi J\frac{\tau}{2}\right)\hat{S}_y\hat{I}_z$$

$$\downarrow \pi J\tau/2$$

$$\hat{\rho}_5 = -\mathbb{B}_S \cos(\Phi)\cos(\pi J\tau)\hat{S}_x + \mathbb{B}_S \sin(\Phi)\cos(\pi J\tau)\hat{S}_y - 2\mathbb{B}_S \sin(\Phi)\sin(\pi J\tau)\hat{S}_x\hat{I}_z - 2\mathbb{B}_S \cos(\Phi)\sin(\pi J\tau)\hat{S}_y\hat{I}_z$$

$$\downarrow \left(\frac{\pi}{2}\right)_y^I + \left(\frac{\pi}{2}\right)_y^S$$

$$\hat{\rho}_6 = \mathbb{B}_S \cos(\Phi)\cos(\pi J\tau)\hat{S}_z + \mathbb{B}_S \sin(\Phi)\cos(\pi J\tau)\hat{S}_y + 2\mathbb{B}_S \sin(\Phi)\sin(\pi J\tau)\hat{I}_x\hat{S}_z - 2\mathbb{B}_S \cos(\Phi)\sin(\pi J\tau)\hat{S}_y\hat{I}_y$$

From here we use the following abbreviations:

$$\iota = \cos(\Phi)\cos(\pi J\tau)$$

$$\kappa = \sin(\Phi)\cos(\pi J\tau)$$

$$\lambda = \sin(\Phi)\sin(\pi J\tau)$$

$$\mu = \cos(\Phi)\sin(\pi J\tau)$$

The next step is then:

$$\downarrow \pi J\ 1/(4\ J)$$

$$\hat{\rho}_7 = \mathbb{B}_S\iota\hat{S}_z + \mathbb{B}_S\kappa\frac{1}{\sqrt{2}}\hat{S}_y - 2\mathbb{B}_S\kappa\frac{1}{\sqrt{2}}\hat{S}_x\hat{I}_z + 2\mathbb{B}_S\lambda\frac{1}{\sqrt{2}}\hat{I}_x\hat{S}_z + \mathbb{B}_S\lambda\frac{1}{\sqrt{2}}\hat{I}_y - 2\mathbb{B}_S\mu\hat{S}_y\hat{I}_y$$

$$\downarrow \left(\frac{\pi}{2}\right)_y^I + \left(\frac{\pi}{2}\right)_y^S$$

$$\downarrow (\pi)_x^I + (\pi)_x^S$$

$$\downarrow \left(\frac{\pi}{2}\right)_y^I + \left(\frac{\pi}{2}\right)_y^S$$

$$\hat{\rho}_8 = -\mathbb{B}_S\iota\hat{S}_z - \mathbb{B}_S\kappa\frac{1}{\sqrt{2}}\hat{S}_y + 2\mathbb{B}_S\kappa\frac{1}{\sqrt{2}}\hat{S}_x\hat{I}_z - 2\mathbb{B}_S\lambda\frac{1}{\sqrt{2}}\hat{I}_x\hat{S}_z - \mathbb{B}_S\lambda\frac{1}{\sqrt{2}}\hat{I}_y - 2\mathbb{B}_S\mu\hat{S}_y\hat{I}_y$$

$$\downarrow \pi J\ 1/(4\ J)$$

$$\hat{\rho}_9 = -\mathbb{B}_S\iota\hat{S}_z + 2\mathbb{B}_S\kappa\hat{S}_x\hat{I}_z - \mathbb{B}_S\lambda\hat{I}_y - 2\mathbb{B}_S\mu\hat{S}_y\hat{I}_y$$

Resolving ι, κ, λ and μ gives:

$$\hat{\rho}_9 = -\mathbb{B}_S\cos(\Phi)\cos(\pi J\tau)\,\hat{S}_z + 2\mathbb{B}_S\sin(\Phi)\cos(\pi J\tau)\,\hat{S}_x\hat{I}_z - \mathbb{B}_S\sin(\Phi)\sin(\pi J\tau)\,\hat{I}_y - 2\mathbb{B}_S\cos(\Phi)\sin(\pi J\tau)\,\hat{S}_y\hat{I}_y$$

Hence, the remaining hyperpolarization on the S spins is described by $-B_S\cos(\Phi)\cos(\pi J\tau)$ while the transferred polarization on the I spins is described by $-B_S\sin(\Phi)\sin(\pi J\tau)$. For I_NS spin systems the remaining hyperpolarization on the S spins can be described by

$-\mathbb{B}_S \cos(\Phi)\cos(\pi J\tau)^N$ while the transferred polarization on the I spins in the higher order spin system is described by $-\mathbb{B}_S\, N \sin(\Phi)\sin(\pi J\tau)$.

4.2.8 Simulations

Evolution of the ^{15}N and ^{1}H magnetizations were simulated using *SpinDynamica*[68] (www.spindynamica.soton.ac.uk) in Wolfram Mathematica (version 11; Wolfram Research, Inc., Champaign, Illinois, USA). The Hamiltonian describing the [$^{15}N_2$]urea spin system is:

$$\hat{H}_0 = 2\pi J_{NH}\left(\hat{S}_z\hat{I}_{z,1} + \hat{S}_z\hat{I}_{z,2}\right) \tag{4.3}$$

where J_{NH} is the negative[111] heteronuclear coupling constant, $\hat{S}$ is the product operator for the ^{15}N spin and $\hat{I}_1$ and $\hat{I}_2$ the operators for the two equivalent protons. To simulate the effect of off-resonance excitation, the term

$$\hat{H}_{\text{off}} = 2\pi\, \nu_{0,1H}\left(\hat{I}_{z,1} + \hat{I}_{z,2}\right) + 2\pi\, \nu_{0,15N}\hat{S}_z \tag{4.4}$$

was added to the $\hat{H}_0$ Hamiltonian. $\nu_{0,15N}$ and $\nu_{0,1H}$ are the excitation frequency offsets in Hz. To estimate relaxation losses the *PhenomenologicalRelaxationSuperoperator* function in *SpinDynamica* was used with the measured T_1 and T_2 times. An uncorrelated relaxation model was assumed. We define the proton polarization P_{1H} divided by the depleted ^{15}N polarization $(1-P_{15N})$ at the end of the transfer block as the efficiency of polarization transfer ($eff = P_{1H}/(1-P_{15N})$), which was typically >80% (Figure 4-3).

4.2.9 Polarization transfer phantom experiments

Polarization transfer experiments were performed on the 7 T scanner using the dual-tuned home-built surface coil as described in the previous chapter. A spherical phantom filled with 3 ml water was positioned in the magnet isocentre. For hyperpolarized acquisitions, 1.5 ml of water were removed and replaced with hyperpolarized [$^{15}N_2$]urea solution. Spectra were acquired with a 2 ms 90° BIR4 excitation pulse after the polarization transfer block, with TR=2 s, sweep width = 100 kHz, number of points = 4096. Images were acquired with a 2D EPI sequence after the polarization transfer block. Six water pre-saturation pulses with crusher

gradients were used prior to the polarization transfer block for both imaging and spectroscopy experiments. Images were acquired with *FOV* = 32x32x1 mm, *TR* = 1s, bandwidth = 250 kHz, matrix size = 32x32.

4.2.10 Interleaved direct and indirect detection

The SNR benefits of indirect over direct detection were determined by interleaving the two acquisition strategies. After injection of 1.5 ml hyperpolarized ^{15}N urea three direct detection ^{15}N spectra were acquired using 30° pulses followed by three indirect polarization transfer measurements (with no water pre-saturation), then three direct detection measurements followed by another three indirect detection measurements. Each spectrum was phase and baseline corrected and then normalized to the standard deviation of the noise in the first 400 points at the downfield end of the spectrum. The indirect detection ^{1}H spectra were further corrected to account for depletion of polarization due to the prior direct ^{15}N detection. This was achieved by multiplying spectra 4,5 and 6 (indirect detection) by three times the reciprocal of the average signal loss between spectra 1 and 2 and between spectra 2 and 3 (direct detection). Spectra 10,11 and 12 were corrected in a similar way, but using a factor calculated from the signal loss between spectra 7 and 8 and between spectra 8 and 9. The ^{1}H spectra were recorded with a sweep width of 10 kHz into 2048 complex points, an acquisition time of 204.8 ms and a *TR* of 500 ms. The directly detected ^{15}N spectra were acquired with a nominal 30° flip angle pulse, sweep width 10 kHz, 2048 complex points, *TR* = 500 ms, which were the same acquisition parameters as used for the indirect measurements. The SNRs were calculated by integrating a 60 point-wide region containing the peak and dividing it by the standard deviation of the noise in the 400 point-wide region at the downfield end of the spectrum.

4.3 Results

4.3.1 Simulations

Simulations of the pulse sequence showed that 21% of the ^{15}N polarization was transferred to ^{1}H and resulted in a ^{1}H z-magnetization that was 1.78 times greater than the initial ^{15}N z-magnetization. At the end of the polarization transfer step 79% of the initial ^{15}N polarization

remained (Figure 4-2b). Simulations including relaxation, using measured relaxation rates, showed that these values were reduced only slightly, from 79% to 74% for the remaining ^{15}N magnetization and from 1.78 to 1.67 for the ^{1}H magnetization. In further simulations the effect of the pulse sequence was simulated for a large range of excitation frequency offsets and pulse amplitudes (Figure 4-3). Transfer efficiency was preserved for large regions of parameter space. We did not include polarization loss due to relaxation because transfer via the strong coupling (J_{NH} = -90 Hz) is fast (~12 ms) and the simulation (Figure 4-2b) showed that this can be neglected.

4.3.2 Exchange rate

The proton exchange rate between urea and water was determined[108] by fitting the peak integrals following saturation $I(t_{sat})$ to:

$$I(t_{sat}) = c\left[1 + k\,T_1\,e^{-\left(1/T_1 + k\right)t_{sat}}\right] \tag{4.5}$$

where c is a dimensionless factor, T_1 is the urea proton relaxation time, t_{sat} are the pre-saturation times and k the exchange rate. This gave c = (1.14±0.09), k = (1.56±0.15) s^{-1} and T_1 = (2.73±0.38) s. The errors are those for the fitting. The measured lifetime for a proton in urea ($1/k$) was 0.64±0.06 s, which is similar to that measured previously for 1 M urea at pH 7 (0.55 s)[112]. The IRRUPT sequence, including the flip back pulse, takes only ~12 ms and therefore the influence of solvent exchange on the urea ^{1}H hyperpolarization was ignored.

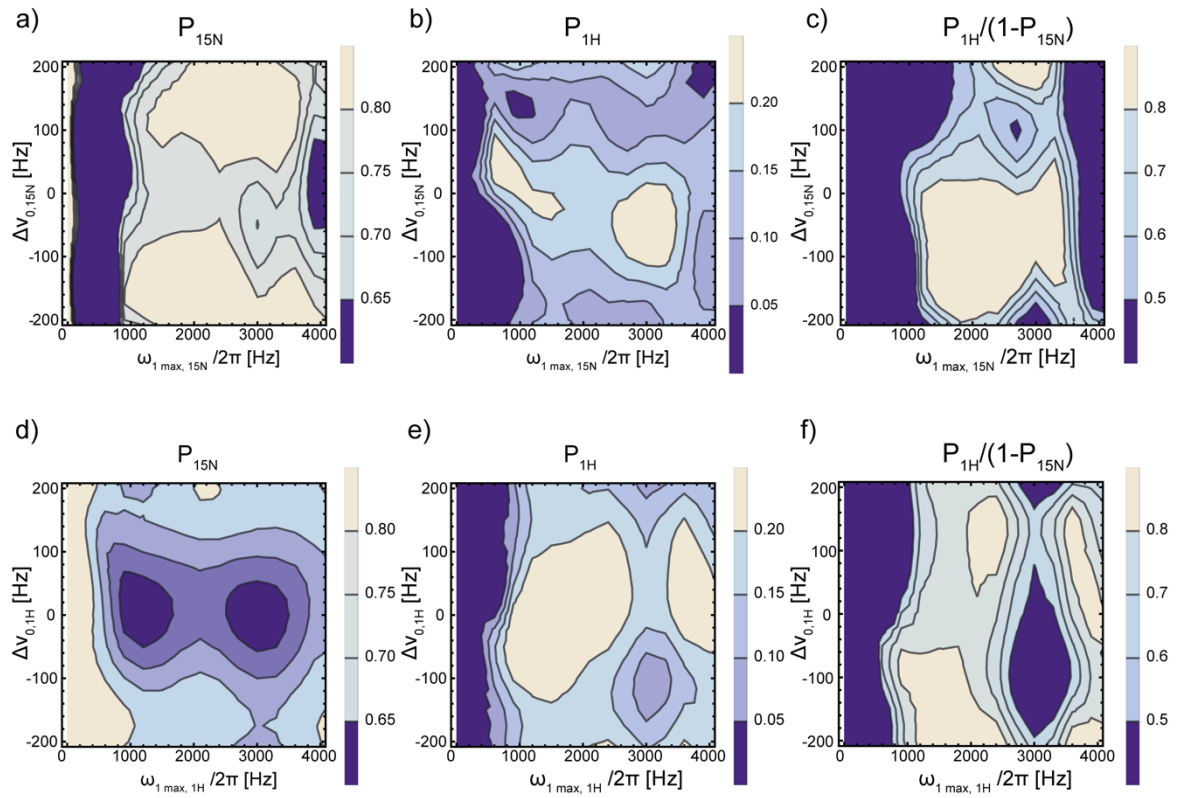

Figure 4-3. Simulations of the IRRUPT pulse sequence. Remaining ^{15}N polarization (P_{15N}) after one transfer as a function of a) ^{15}N excitation frequency offset and ^{15}N maximum pulse amplitude and d) ^{1}H excitation frequency offset and ^{1}H maximum pulse amplitude. ^{1}H polarization (P_{1H}) after one transfer as a function of b) ^{15}N excitation frequency offset and ^{15}N maximum pulse amplitude and e) ^{1}H excitation frequency offset and ^{1}H maximum pulse amplitude. Polarization transfer efficiency $P_{1H}/(1- P_{15N})$ as a function of c) ^{15}N excitation frequency offset and ^{15}N maximum pulse amplitude and f) ^{1}H excitation frequency offset and ^{1}H maximum pulse amplitude. The asymmetry in the profiles results from the use of adiabatic pulses.

4.3.3 Polarization

The measured polarization was 6.2% for [^{13}C]urea and 2.3% for [$^{15}N_2$]urea. The value for ^{15}N was lower than the 5% reported previously[103], while the value for ^{13}C was between a reported *in vivo* value of 3%[14] and a value of 10% estimated at the time of injection[113].

4.3.4 Relaxation times

Relaxation times for ^{15}N and ^{1}H in urea in PBS at 7 T are summarized in Table 4-1. The proton T_1 (2.57±0.08) was similar to a value obtained at 14.1 T from fitting saturation recovery data to Equation 4.5 (2.73±0.38 s).

Table 4-1. Relaxation times for [$^{15}N_2$]urea measured at 7 T.

[$^{15}N_2$]urea	T_1 relaxation time (s)	T_2 relaxation time (s)
^{1}H	2.57±0.08	0.060±0.003
^{15}N	24.22±1.15	1.622±0.94

1 M [$^{15}N_2$]urea in PBS containing 10% $^{2}H_2O$ at 20 °C.

4.3.5 Coil performance

The uncorrected ratio of the ^{1}H and ^{15}N SNRs was 59.9. When corrected for the number of contributing nuclei per molecule (four protons, two ^{15}N nuclei) and the different thermal polarizations calculated using Equation 4.1, this gave an effective SNR enhancement (ε) of 6.07 when detecting ^{1}H versus ^{15}N for a given level of polarization. For example, if the SNR of an ^{15}N acquisition is 10, the SNR of a ^{1}H acquisition at the same nuclear concentration and polarization will be 60.7.

4.3.6 Polarization transfer

Partial transfer of polarization from ^{15}N to ^{1}H can be used for dynamic spectral acquisition (Figure 4-4) or for imaging (Figure 4-5). The 90 Hz splitting in the ^{1}H spectra is due to the ^{1}H-^{15}N coupling[114].

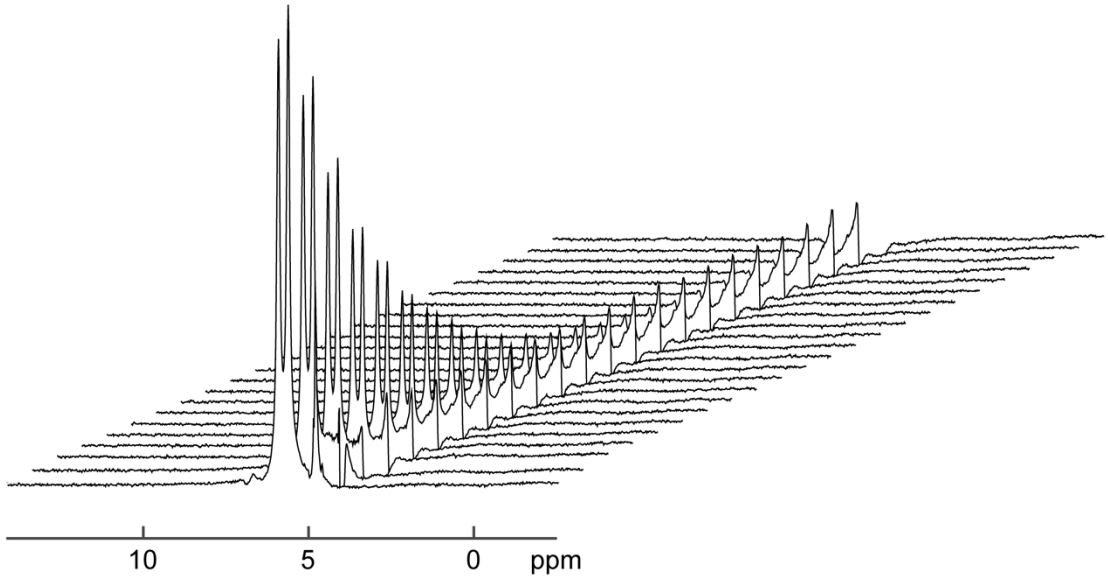

Figure 4-4. Dynamic ^{1}H spectra of hyperpolarized [$^{15}N_2$]urea. Each spectrum was acquired with an IRRUPT polarization transfer block followed by a 90° BIR4 excitation pulse. Parameters were *TR* = 2 s, sweep width = 10000 Hz, number of points = 4096.

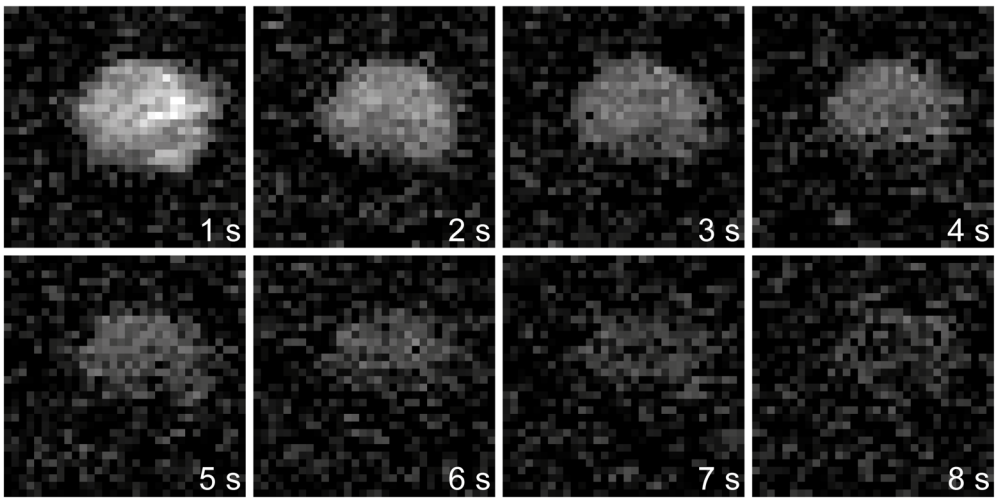

Figure 4-5. Dynamic ^{1}H images of hyperpolarized [$^{15}N_2$]urea. The images were acquired with a 2D EPI sequence after successive polarization transfer blocks. Imaging parameters were: *FOV* = 32x32x1 mm, *TR* = 1 s, bandwidth = 250 kHz, matrix size = 32x32.

4.3.7 Interleaved direct and indirect detection of ^{15}N urea

The SNR in the indirect detection spectra recorded immediately after the direct detection spectra was significantly higher (Figure 4-6a). There was an ~8 s delay in changing from one pulse sequence to the next. After correcting for depletion of polarization in the preceding direct detection experiment there was a 2.09±0.31(SD)-fold improvement in SNR in the indirect detection experiment (Figure 4-6b). Each indirect measurement led to 20% depletion of the ^{15}N polarization. Comparing spectrum 1 with 2 and 2 with 3, and similarly spectrum 7 with 8 and 8 with 9 shows that each of the direct acquisitions depleted 13±7 (SD)% of the polarization, which corresponds to a flip angle of 30° (acos(0.87) = 30°). To compare the SNR of the directly and indirectly detected spectra, we corrected the SNR improvement factor of 2.09±0.31 by sin30°/sin37°, which corrects for the fact that the indirect experiment depleted 20% of the ^{15}N polarization (cos(37°)=0.8) whereas the direct detection experiment depleted 13% of the polarization. This gives a corrected improvement in the SNR of 1.72±0.25.

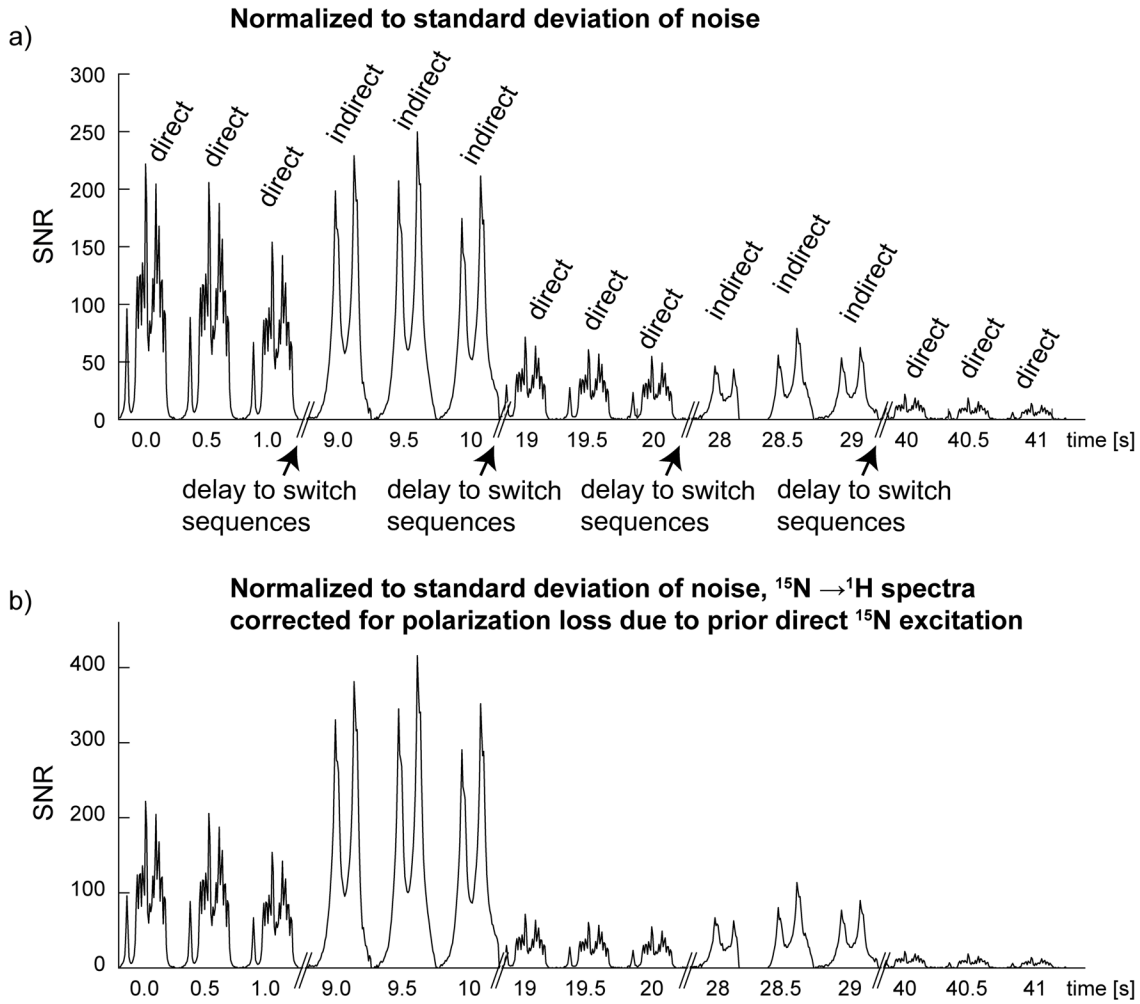

Figure 4-6. Interleaved direct ^{15}N detection and indirect ^{1}H detection of hyperpolarized ^{15}N urea. a) The spectra were scaled so that the noise was the same in all the spectra. b) Indirect detection spectra additionally corrected for depletion of polarization due to the prior direct detection experiment.

4.4 Discussion

4.4.1 Theoretically achievable SNR improvement in polarization transfer experiments

The signal in a direct detection experiment following a 90° excitation pulse, when compared to an INEPT-type experiment that transfers all the polarization, increases with the square of the detection frequency, ν^2. However, detector coil and sample noise also increase as $\nu^{1/4}$ to ν,

depending on the source of the noise. Therefore the overall increase in the SNR as a function of ν is given by[69,90]:

$$SNR \propto \frac{\nu^2}{(\alpha a^2 \nu^{1/2} + \beta \nu^2 b^5)^{1/2}} \tag{4.6}$$

where a and b are coil geometry parameters and α and β are weightings for the two sources of noise, where α represents coil noise and β sample noise.

Equation 4.6 is valid when comparing the SNR of a direct detection experiment with a 90° pulse to a measurement in which all the available polarization is transferred with perfect efficiency to a coupled high γ nucleus for detection. However, for dynamic measurements only small portions of the hyperpolarization should be used at any one time, either by using a small flip angle pulse in the direct detection experiment or by using partial polarization transfer in the indirect experiment. In this situation we also need to consider the residual polarization left following each excitation since this represents the longitudinal magnetization available for subsequent excitation[115]. The detectable transverse magnetization in a direct detection experiment depends on the flip angle (*FA*) thus:

$$\left(M_{xy}\right)_{direct\ detect} \propto \sin FA\,. \tag{4.7}$$

Expressing the detectable magnetization in terms of the z magnetization used ($(M_z^{hyp})_{\text{used}}$) then:

$$\left(M_{xy}\right)_{direct\ detect} \propto \sqrt{1 - \left[1 - \left(M_z^{hyp}\right)_{used}\right]^2}\,. \tag{4.8}$$

In an indirect detection experiment the detected transverse magnetization in the higher γ nucleus is proportional to the gain from the higher precession frequency (γ_{1H}/γ_{15N}) multiplied by the z-magnetization used $(M_z^{hyp})_{used}$ in the lower γ nucleus:

$$\left(M_{xy}\right)_{indirect\ detect} \propto \frac{\gamma_{high}}{\gamma_{low}} \left(M_z^{hyp}\right)_{used}\,. \tag{4.9}$$

Comparing equation (4.8) and (4.9) shows, that if

$$\frac{\gamma_{high}}{\gamma_{low}}\left(M_z^{hyp}\right)_{used} < \sqrt{1-\left[1-\left(M_z^{hyp}\right)_{used}\right]^2} \tag{4.10}$$

then transferring polarization to the higher γ nucleus will result in a smaller transverse magnetization than would be obtained by direct detection. The effect this has on SNR is illustrated in Figure 4-7a, where the SNR of direct ^{15}N detection with a 90° pulse is assumed to be 1. The SNR improvement for different detection strategies (^{15}N direct detection, ^{15}N→^{1}H indirect detection or ^{13}C direct detection) as a function of the magnetization used per acquisition are indicated, assuming that polarization transfer is 100% efficient.

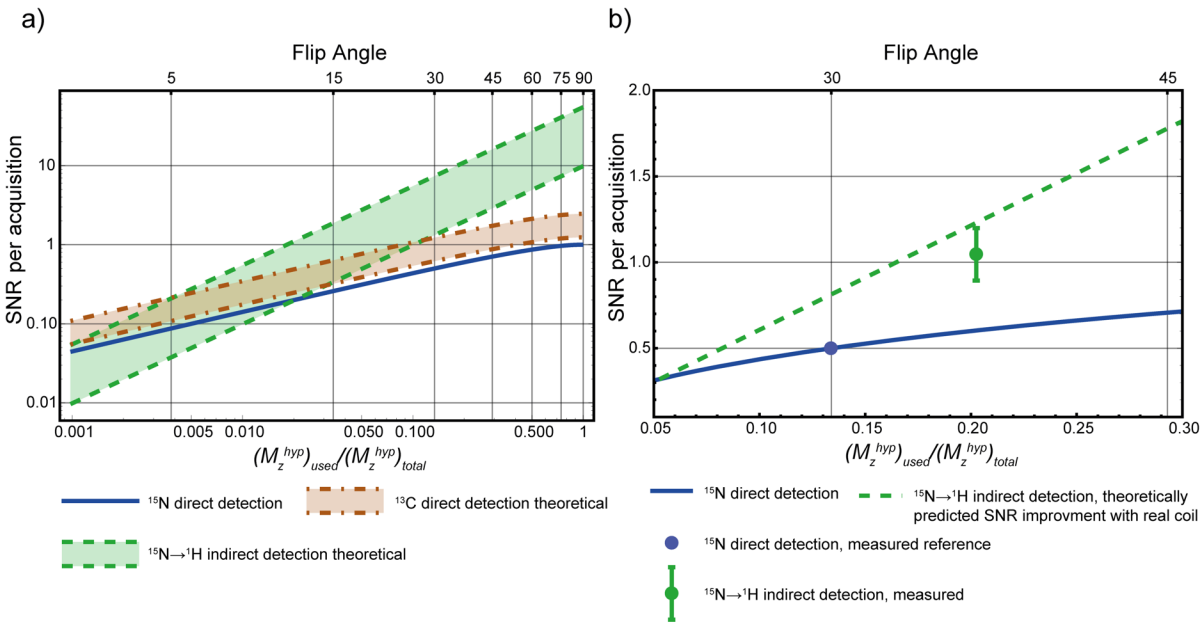

Figure 4-7. a) Theoretical SNR improvements for indirect detection as a function of flip angle and magnetization used. The upper limit of the SNR improvement band is reached when only coil noise is considered, the lower limit is reached when only sample noise is considered. In reality both, coil and sample noise contribute, and the improvement factor is in-between these two boundaries (see equation 4.6). b) Calculated and measured SNR improvement for indirect detection as a function of flip angle and magnetization used. The dashed green line is the theoretically predicted upper limit for the SNR improvement when the home build coil is used.

4.4.2 Experimental measurements of SNR

From ^{1}H and ^{15}N spectra acquired using 90° pulses from a thermally polarized urea sample we calculated that the SNR enhancement (ε) from detecting ^{1}H as opposed to ^{15}N was 6.07.

Therefore, in a polarization transfer experiment with perfect transfer efficiency we can expect an increase in SNR by a factor of:

$$\frac{SNR_{15N\rightarrow 1H}}{SNR_{15N}} = \frac{\varepsilon \left(M_z^{hyp}\right)_{used}}{\sqrt{1-\left[1-\left(M_z^{hyp}\right)_{used}\right]^2}} \tag{4.11}$$

The measured SNRs for direct and indirect ^{15}N detection and the values expected theoretically are shown in Figure 4-7b.

4.4.3 Effect of polarization levels

The ^{13}C polarizations achievable with our *HyperSense* polarizer were 2.7-fold higher than the ^{15}N polarization (6.2% vs 2.3%), in agreement with levels reported previously for labelled urea (5% ^{15}N polarization[103] and 3%[14] to 10%[113] ^{13}C polarization). Therefore, ^{15}N as a nucleus for hyperpolarization has two disadvantages when compared to ^{13}C; the polarization is lower, and the lower gyromagnetic ratio makes it harder to detect. Some of the sensitivity disadvantage can be recovered by indirect detection with INEPT sequences or, if dynamic acquisition is required, using the IRRUPT pulse sequence described here. If [^{15}N]urea could be polarized to levels similar to those of [^{13}C] then the SNR advantages of our detection method would be even greater (see Figure 4-7a). Indirect detection of [^{13}C]urea is not feasible because the coupling constant with the protons, which are in exchange with solvent protons where the exchange rate is fast compared to the coupling constant, is weak and not observed.

4.5 Conclusion

It was shown that partial polarization transfer from ^{15}N to ^{1}H using a modified BINEPT[109] sequence can be used for dynamic imaging of hyperpolarized [^{15}N]urea. If more than 10% of the ^{15}N polarization is used in each acquisition then the sequence can give better sensitivity than direct ^{13}C detection of [^{13}C]urea.

Chapter 5 Partial hyperpolarization transfer in [2-^{13}C]pyruvate

As described in chapters 2 and 4, there are advantages in detecting nuclear hyperpolarization in a low γ nucleus via spin coupled protons, including a significant increase in SNR compared to direct detection. To examine the scope of proton detection as a tool for observation of low γ hyperpolarized nuclei and to demonstrate the versatility and utility of the IRRUPT sequence, partial polarization transfer is demonstrated in this chapter with [2-^{13}C]pyruvate. Because the principles of the pulse sequence have been introduced in the previous text, this chapter focuses on issues that are specific to [2-^{13}C]pyruvate.

This molecule, in its hyperpolarized state, has been used in several studies, mostly to investigate TCA cycle activity[116–119] but also to probe glycolysis[119,120]. In healthy rat brain it was shown, that dichloroacetate (DCA) enhances the production of [5-^{13}C]glutamate from hyperpolarized [2-^{13}C]pyruvate[118]. Another study compared the spectra acquired following the administration of hyperpolarized [1-^{13}C]pyruvate to spectra acquired following the administration of hyperpolarized [2-^{13}C]pyruvate in rat brain. As expected, injection of [1-^{13}C]pyruvate resulted in observable [1-^{13}C]lactate and [^{13}C]bicarbonate in the brain. Injection of [2-^{13}C]pyruvate led to the appearance of [2-^{13}C]lactate in the spectra, but, against the expectations, no [5-^{13}C]glutamate was observed[116]. Another study, using non-localized spectroscopy of the whole body of a rat, showed that DCA administration increased labelled bicarbonate production following hyperpolarized [1-^{13}C]pyruvate injection and increased the levels of [5-^{13}C]glutamate, [1-^{13}C]acetoacetate and [1-^{13}C]acetylcarnitine following hyperpolarized [2-^{13}C]pyruvate injection[117]. In a ^{13}C imaging study with C6 glioma-bearing rats, hyperpolarized [2-^{13}C]pyruvate could be used to produce maps of the substrate itself, [5-^{13}C]glutamate and [2-^{13}C]lactate[119]. Recently the use of hyperpolarized [2-^{13}C]pyruvate in humans has been reported for the first time[120]. In a feasibility study in human brain, [2-^{13}C]pyruvate, [5-^{13}C]glutamate and [2-^{13}C]lactate were observed. Pyruvate and glutamate

maps were generated and it was shown that the rates for pyruvate-lactate exchange calculated from fits of the [2-^{13}C]labelled and [1-^{13}C]labelled metabolites to a simple exchange model give the same rate constant[120].

As shown in chapter 2 and in our publications[90,121] dynamic hyperpolarized ^{1}H lactate spectra and images can be generated from hyperpolarized [1-^{13}C]lactate produced *in vivo* from injected hyperpolarized [1-^{13}C]pyruvate. However, in [1-^{13}C]pyruvate polarization cannot be efficiently transferred to the methyl protons due to the weak ^{13}C to ^{1}H coupling (~1 Hz [116]). To gather dynamic information from proton detection of hyperpolarized pyruvate, it was decided therefore to explore the use [2-^{13}C]pyruvate instead, where the ^{13}C - ^{1}H coupling is 6.2 Hz [116] (Figure 5-1). This coupling offers the possibility of controlled and efficient transfer of polarization.

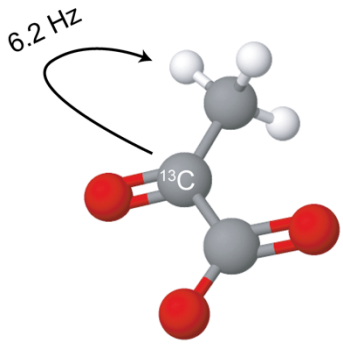

Figure 5-1. Structure of [2-^{13}C]pyruvate. The coupling constant between ^{13}C and the directly bonded protons is 6.2 Hz.

5.1 Methods

5.1.1 Adjustments to the IRRUPT sequence

To accommodate partial polarization transfer in [2-^{13}C]pyruvate the inter-pulse delays and the phase of the second pulse on the low y spins had to be modified. The delays between the pulses ($\tau_{1\text{-}4}$,defined in chapter 4) and the additional phase offset δ (also defined in chapter 4) in the segmented BIR4 pulse on the ^{13}C spins were chosen as described for the HINDER sequence when aiming to transfer 10% of polarization in an I_3S system[110]. For three protons coupled with

a 6.2 Hz coupling constant to one low γ nucleus: $\tau_1 + \tau_2 = 0.358/(2\,\pi\,J) = 9.19$ ms, $\tau_3 + \tau_4 = 1/(2\,J) = 80.65$ ms, $\delta = 17.980°$. The delays were not corrected for the fact that adiabatic pulses were used instead of hard pulses. The pulse length in this experiment is still relatively short when compared to the duration of the delays between the pulses, because the 6.2 Hz coupling leads to long delays, especially when compared to the short delays required by the 90 Hz coupling in [$^{15}N_2$]urea.

Evolution of the ^{13}C and ^{1}H magnetizations were simulated with *SpinDynamica*[68]. Relaxation was neglected in all the simulations. The Hamiltonian describing the relevant carbon-13 to methyl proton coupling in [2-^{13}C]pyruvate is:

$$\hat{H}_0 = 2\pi\, J_{CH}\left(\hat{S}_z\hat{I}_{z,1} + \hat{S}_z\hat{I}_{z,2} + \hat{S}_z\hat{I}_{z,3}\right)$$

where J_{CH} is the heteronuclear coupling constant, $\hat{S}$ is the product operator for the ^{13}C spin and $\hat{I}_1$, $\hat{I}_2$ and $\hat{I}_3$ the operators for the three equivalent protons. To simulate the effect of off-resonance excitation, the term

$$\hat{H}_{\text{off}} = 2\pi\, \nu_{0,1H}\left(\hat{I}_{z,1} + \hat{I}_{z,2} + \hat{I}_{z,3}\right) + 2\pi\, \nu_{0,13C}\hat{S}_z$$

was added to the $\hat{H}_0$ Hamiltonian. $\nu_{0,13C}$ and $\nu_{0,1H}$ are the excitation frequency offsets in Hz. As in the previous chapter we define the proton polarization P_{1H} divided by the depleted ^{13}C polarization $(1-P_{13C})$ at the end of the transfer block as the efficiency of polarization transfer ($eff = P_{1H}/(1-P_{13C})$)

5.1.2 Dynamic nuclear polarization

To 1 g of [2-^{13}C]pyruvic acid, 16.7 mg of the radical OX063 were added. For each hyperpolarization a 44 mg (~36 µl), sample was prepared from the stock solution by adding 1 µl of 1:10 Dotarem. To find the optimal microwave frequency for polarization, a measurement of the frequency dependency of the solid-state polarization (frequency sweep) was performed from 94.100 GHz to 94.140 GHz using a step size of 2 MHz, measuring the solid state ^{13}C signal after 200 s of irradiation at each step using the *HyperSense* polarizer (Oxford Instruments). A maximum was found at 94.110 GHz. For further experiments, [2-^{13}C]pyruvate

was polarized at this frequency for 45 min or longer. For dissolution 6 ml of a buffer (pH 7.2) containing 40 mM Hepes, 94 mM NaOH, 30 mM NaCl and 100 mg/L EDTA was used.

5.1.3 Polarization transfer phantom experiments

For the spectroscopic measurements no water suppression was used. Acquisition parameters for spectroscopy were: *TR* = 2 s; sweep width = 10000 Hz; number of points = 2048. For imaging, a preinstalled VAPOR saturation sequence[122] was applied to suppress the water signal. A 2D EPI sequence was used with a *FOV* of 20 mm x 20 mm and nominal resolution of 1.25 mm x 1.25 mm. The signal was acquired directly after polarization transfer from the transverse magnetization. Therefore, in z direction only the RF excitation profile locates the signal. The sweep width was 125000 Hz. The k-space was undersampled (12x16 instead of 16x16) and the missing lines were zero filled before reconstruction. *TR* was 1 s. Unlike in the previous chapter, where transverse proton magnetization was flipped onto the z-axis and then excited with a 90° ^{1}H pulse, the data presented here was acquired directly from the transverse magnetization. Polarization transfer experiments were performed on a 7 T scanner (Agilent) using the ^{13}C/^{1}H dual-tuned home-built surface coil that was built as described by Wetterling *et al.*[101] and that was presented in chapter 4. A spherical phantom filled with 4 ml water was positioned in the magnet isocentre. 1 ml of hyperpolarized [2-^{13}C]pyruvate solution was injected immediately before starting the acquisition.

5.2 Results and Discussion

5.2.1 Simulations

With adiabatic pulses in the simulations the IRRUPT sequence transferred typically 15% to 20% of the ^{13}C hyperpolarization to coupled (J_{CH} = 6.2 Hz) protons with an efficiency of 80% or more (Figure 5-2). Transfer efficiency was preserved for large regions of parameter space.

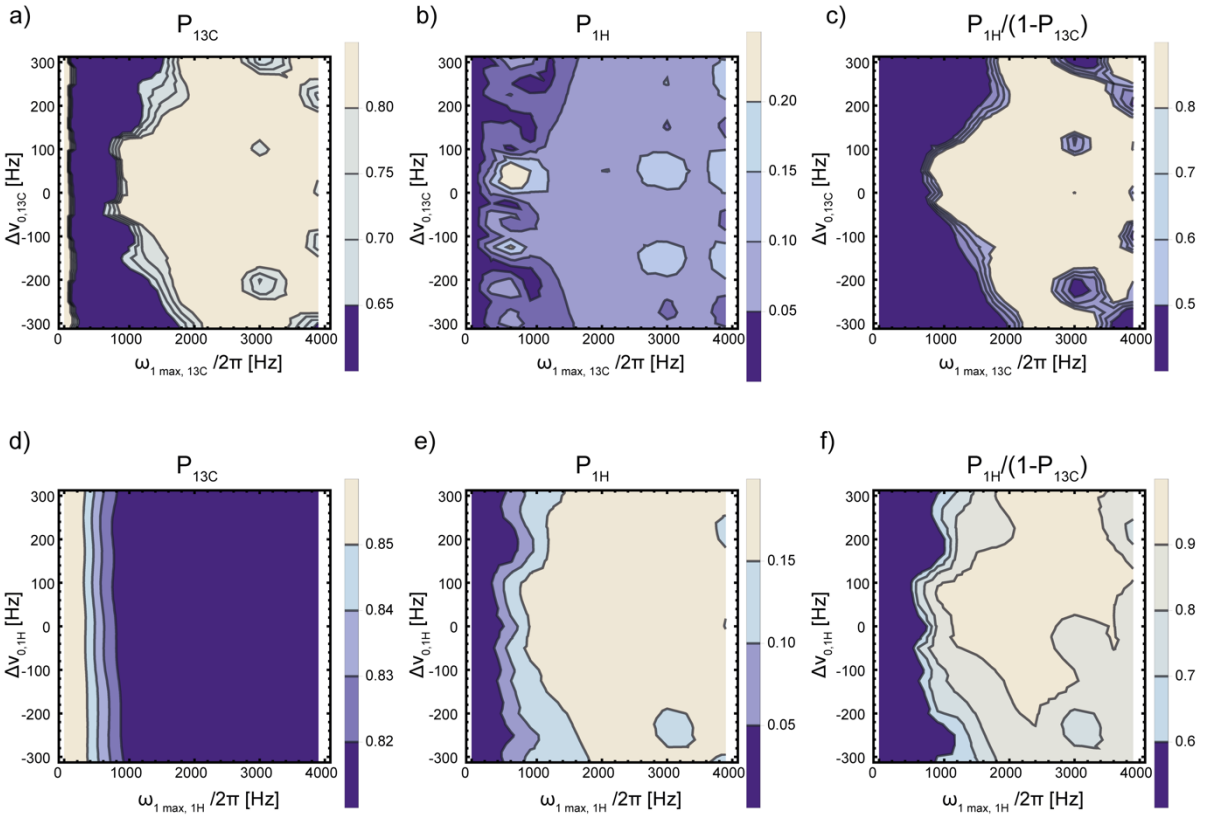

Figure 5-2. Simulations of the IRRUPT pulse sequence. Remaining ^{13}C polarization (P_{13C}) after one transfer as a function of a) ^{13}C excitation frequency offset and ^{13}C maximum pulse amplitude and d) ^{1}H excitation frequency offset and ^{1}H maximum pulse amplitude. ^{1}H polarization (P_{1H}) after one transfer as a function of b) ^{13}C excitation frequency offset and ^{13}C maximum pulse amplitude and e) ^{1}H excitation frequency offset and ^{1}H maximum pulse amplitude. Polarization transfer efficiency $P_{1H}/(1- P_{13C})$ as a function of c) ^{13}C excitation frequency offset and ^{13}C maximum pulse amplitude and f) ^{1}H excitation frequency offset and ^{1}H maximum pulse amplitude. The asymmetry in the profiles results from the use of adiabatic pulses.

5.2.2 Experimental results

Partial transfer of polarization from ^{13}C to ^{1}H could be used for dynamic spectral acquisition (Figure 5-3). The unusual shape of the water peak in the spectra can be explained by off resonant excitation induced by the adiabatic pulses. No water suppression was used prior to the IRRUPT sequence in the spectral measurements, but the [3,3,3-^{1}H]pyruvate resonance nevertheless is relatively unobstructed due to the large chemical shift difference from the water resonance (>600 Hz at 7 T). From spectrum to spectrum a 20-30% reduction of the pyruvate

resonance was observed. This value shows a decrease in the polarization following each measurement that is larger than the simulated decrease of 15-20%. This can be explained by T_2 losses during the polarization transfer, which were not included in the simulations. Furthermore, T_1 losses during the subsequent measurements result in a decrease of the signal intensity.

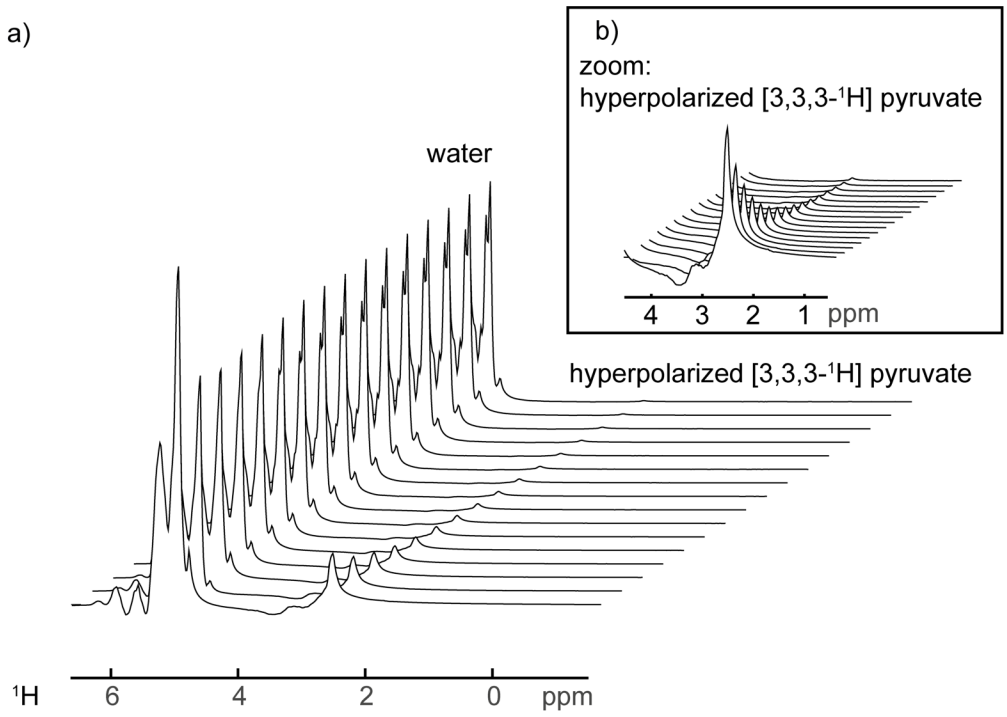

Figure 5-3. Dynamic ^{1}H spectra of hyperpolarized [2-^{13}C]pyruvate. Each spectrum was acquired with an IRRUPT polarization transfer sequence. Parameters were TR = 2 s, sweep width = 10000 Hz, number of points = 2048. The acquisition was started after injection of 1 ml hyperpolarized [2-^{13}C]pyruvate solution onto a phantom containing 4 ml PBS. The pyruvate signal decayed by 20-30% between spectra. No water suppression was used.

The IRRUPT partial transfer was also used to generate proton images from hyperpolarized [2-^{13}C]pyruvate (Figure 5-4). Here VAPOR water suppression[122] successfully removed residual water signal, and the average intensity of the images reconstructed from repetitively transferred signal decreased with a simple exponential decay (Figure 5-4b). The signal was reduced by 30% between measurements. This signal loss per measurement was stable over the course of the experiment, which means that it could be, once it was quantified, integrated in a kinetic model of enzyme activity in future experiments.

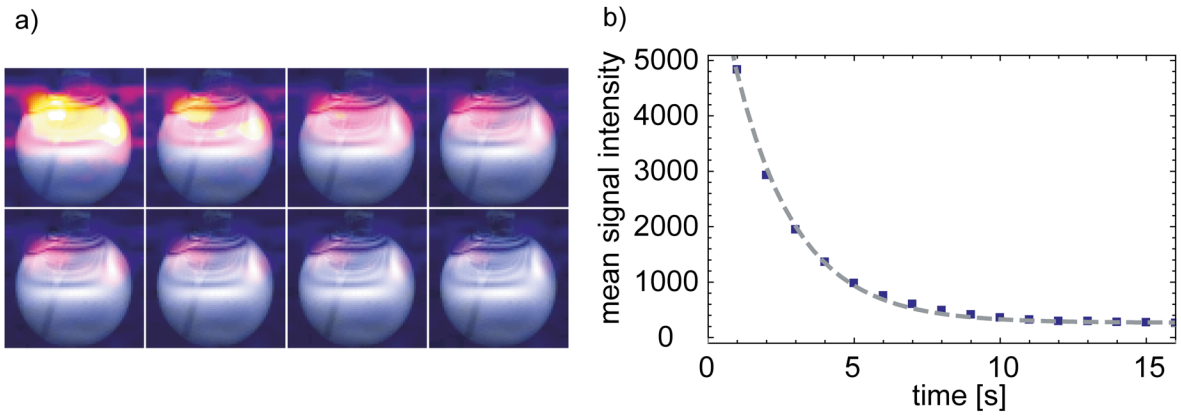

Figure 5-4. a) False colour: Dynamic ^{1}H images of hyperpolarized [2-^{13}C]pyruvate. The images were acquired with an EPI sequence after successive polarization transfers. Imaging parameters were: *FOV* = 20x20 mm, *TR* = 1 s, bandwidth = 125 kHz, matrix size = 16x16. The images were interpolated to a matrix size of 64 x 64 to match the reference image. The nonuniformity of the pyruvate images is probably due to the problematic EPI distortion correction. The reference for the EPI distortion correction was acquired before the injection of the hyperpolarized pyruvate and could therefore only provide limited correction for B_0 and susceptibility inhomogeneities in the images with hyperpolarized pyruvate. The greyscale ^{1}H reference image was acquired with a gradient echo sequence. *TR* = 0.5 s, 5 mm slice thickness, *FOV* = 20x20 mm, matrix size = 64 x 64. b) The transferred signal was reduced by 30% between measurements.

5.3 Conclusion

The IRRUPT sequence was used to transfer hyperpolarization piecemeal from the ^{13}C nucleus in [2-^{13}C]pyruvate to the spin-coupled methyl protons. Polarization transfer in this molecule was stable over an even larger parameter range (Figure 5-2) when compared to the transfer in [$^{15}N_2$]urea (chapter 4). This is because in the latter case, the adiabatic pulses are long compared to the timescale of the evolution of the *J*-coupling. In [2-^{13}C]pyruvate the coupling is weaker and the evolution is slower and therefore has a negligible influence during the pulses.

In principle, hyperpolarized [1-^{13}C]pyruvate and hyperpolarized [2-^{13}C]pyruvate could be injected simultaneously. In such an experiment, application of the IRRUPT sequence to [2-^{13}C]pyruvate could be interleaved with a sequence that transfers all the polarization in the [1-^{13}C]lactate produced from the [1-^{13}C]pyruvate, for example using a spectrally selective reverse INEPT sequence[90] or a BINEPT sequence[109] sequence. This experiment could give a fuller picture of the reaction catalysed by lactate dehydrogenase (LDH). The labelling time courses

generated would have the same information as direct ^{13}C measurements acquired with the saturation recovery method described by Schulte *et al.*[87] and could be used to map metabolic exchange rates. While this sounds promising in theory, in practise this experiment might be difficult to implement. When both hyperpolarized [1-^{13}C]pyruvate and [2-^{13}C]pyruvate are present, a sequence that transfers polarization in [2-^{13}C]pyruvate must have a negligible effect on the [1-^{13}C]pyruvate resonance, which is 35 ppm (2626 Hz at 7 T) away (Figure 5-5). Likewise, a sequence that transfers polarization in [1-^{13}C]lactate must have a negligible effect on the [1-^{13}C]pyruvate resonance (relative offset to [1-^{13}C]lactate: 12.2 ppm or 919 Hz at 7 T) and the [2-^{13}C]pyruvate resonance (relative offset to [1-^{13}C]lactate: 22.8 ppm or 1707 Hz at 7 T). Spectrally selective methods would be well within these specifications, however the IRRUPT or BINEPT sequences, which use adiabatic pulses that act on a much wider spectral region, would possibly lead to destruction of the hyperpolarization stored in [1-^{13}C]pyruvate and/or [2-^{13}C]pyruvate.

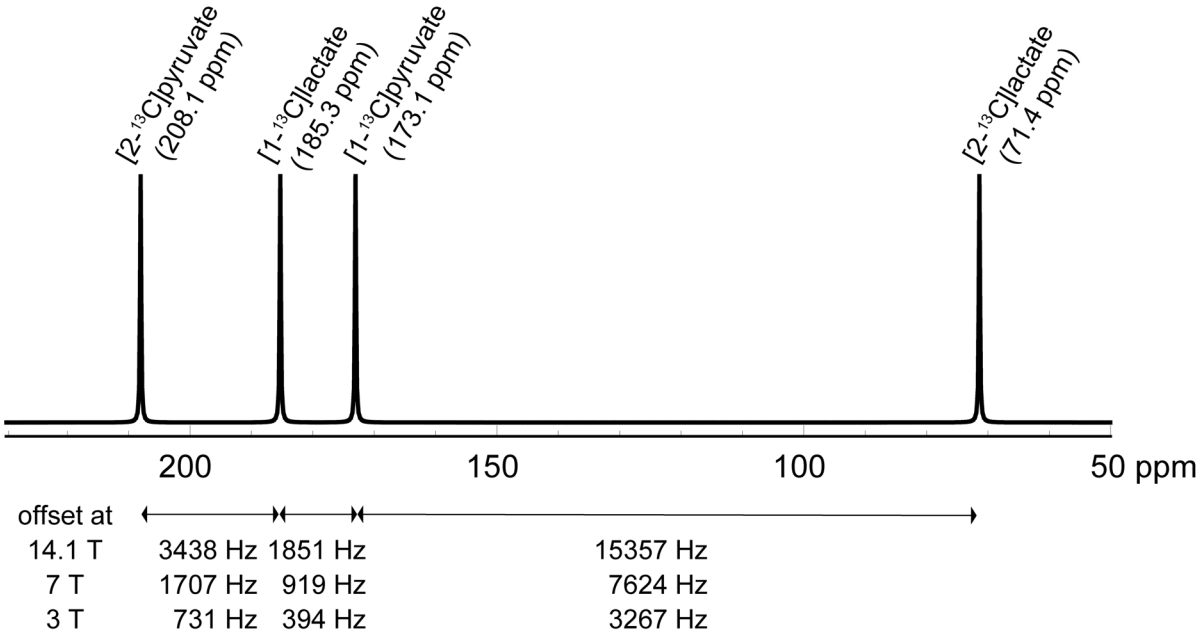

Figure 5-5. Simulated ^{13}C NMR spectrum of [2-^{13}C]pyruvate, [2-^{13}C]lactate, [1-^{13}C]pyruvate and [1-^{13}C]lactate with indicated chemical shift differences in Hz at different field strengths. If adiabatic sequences like IRRUPT or BINEPT are used to transfer polarization in an experiment where hyperpolarized [2-^{13}C]pyruvate and [1-^{13}C]pyruvate were coinjected, problems may arise due to off resonance effects of the pulse sequence which could destroy hyperpolarization.

It is conceivable that two IRRUPT sequences could be implemented that probe [2-^{13}C]lactate and [2-^{13}C]pyruvate in an interleaved fashion, which would give full control of the amount of transferred polarization in each metabolite and would correspond to a direct detection experiment with different flip angles on the two metabolites. Such experiments could be evaluated with model free approaches like the area under the curve method[88]. But again, it would have to be determined whether the IRRUPT sequence applied to [2-^{13}C]lactate affects the polarization stored in [2-^{13}C]pyruvate when used to transfer polarization in [2-^{13}C]lactate (Figure 5-5). However, in this experiment, the resonances are very far apart (136.7 ppm or 10250 Hz at 7 T) and the sequences would not have to be quite as spectrally selective as for an experiment where hyperpolarized [1-^{13}C]pyruvate and [2-^{13}C]pyruvate are coinjected (Figure 5-5). Another problem would be, that the strong coupling (~146 Hz [116]) in [2-^{13}C]lactate leads to an evolution of the *J*-coupling that is too fast to be used for polarization transfer with the proposed sequences.

Chapter 6 Measuring tumour glycolytic flux *in vivo* using fast deuterium magnetic resonance imaging

---

The text and figures in this chapter have been submitted for publication in similar or identical form in

Kreis F, Wright AJ, Hesse F, Fala M, Hu D, Brindle KM. Measuring tumor glycolytic flux in vivo using fast deuterium magnetic resonance imaging. *Radiology,* under review.

My contribution to this publication was the development of the pulse sequence, cultivating the cells, building the coil, performing the experiments and analysing the data. Dr De-en Hu prepared the mice. Dr Alan Wright and Prof Kevin Brindle and me designed the study. Maria Fala and Friederike Hesse helped with cell cultivation. Dr Alan Wright contributed to the pulse sequence development and image reconstruction.

Recently a new imaging modality[23,123] has emerged which allows mapping metabolite concentrations *in vivo* without the use of hyperpolarization. This technique relies on the administration of deuterated substrates and subsequent ^{2}H MR acquisition. The signal intensities can be normalized to the endogenous semi-heavy water, which makes this method quantitative. In the following chapter it is shown how this technique, which has been termed deuterium metabolic imaging (DMI), can be used to map glycolytic fluxes *in vivo*.

6.1 Introduction

Tumour cells frequently show high rates of aerobic glycolysis, which provides the glycolytic intermediates needed for the increased biosynthetic demands of rapid cell growth and proliferation[8,10]. High rates of glycolysis have enabled disease detection and treatment response monitoring using Positron Emission Tomography, where tumours frequently show high levels of uptake of the glucose analog 2-([^{18}F]fluoro)-2-deoxy-D-glucose (FDG-PET) when compared with surrounding tissues, with tumours responding to treatment showing decreased uptake[4,124–126]. High levels of tumour lactate resulting from this increased glycolytic flux have also enabled monitoring of disease grade, progression and response to treatment using ^{13}C magnetic resonance spectroscopic imaging of hyperpolarized [1-^{13}C]pyruvate metabolism[17,18,22,127]. In this technique the massive gain in sensitivity afforded by ^{13}C nuclear spin hyperpolarization (10^4 – 10^5x)[13] has allowed imaging of the exchange of the hyperpolarized ^{13}C label between injected [1-^{13}C]pyruvate and the endogenous tumour lactate pool, where disease progression is often accompanied by an increase in lactate labelling and a positive response to treatment by a decrease. However, both FDG-PET and hyperpolarized [1-^{13}C]pyruvate interrogate only limited aspects of the glycolytic phenotype of tumours. FDG-PET reports on tumour perfusion, FDG uptake on the glucose transporters, and phosphorylation and trapping in the reaction catalysed by hexokinase. The hyperpolarized [1-^{13}C]pyruvate experiment reports on perfusion, pyruvate uptake on the monocarboxylate transporters (MCTs) and exchange of ^{13}C label in the reaction catalysed by lactate dehydrogenase (LDH)[44]. As label exchange between pyruvate and lactate is dependent on lactate pool size the technique effectively assesses more of the glycolytic pathway than FDG-PET[128] but nevertheless cannot monitor glycolytic flux directly.

^{13}C magnetic resonance spectroscopic imaging (MRSI) has been used with hyperpolarized[12] and non-hyperpolarized[31] [U-^{13}C]glucose to image glycolysis in murine tumour models, in the latter case tensor decomposition was essential for denoising the resulting glucose and lactate images. However, neither study produced maps of glycolytic flux. Recently, ^{2}H MRSI has been introduced as a tool for clinical imaging of tumour metabolism *in vivo*[23]. The relatively low sensitivity of ^{2}H to magnetic resonance detection is compensated for by the fast T_1 relaxation of this nucleus, which permits very fast signal acquisition without signal saturation.

A limitation is the relatively small chemical shift range, which is ~70 times smaller than that of ^{13}C and can result in poorly resolved spectra[129]. ^{2}H spectroscopic images were acquired from glioma-bearing rats between 60 - 90 minutes after the start of [6,6′-$^{2}H_2$]glucose infusion and showed signals from labelled lactate and glutamate in the tumour, although the glutamate signal was not resolved from that of glutamine and since only single images were acquired there was no rate information. Glutamate is labelled by rapid exchange of deuterium label with the TCA cycle intermediate, α-ketoglutarate, and therefore the deuterated lactate/glutamate ratio provides a direct measure of the partitioning of glucose carbon between glycolysis and the TCA cycle. In glioma patients, oral administration of [6,6′-$^{2}H_2$]glucose also resulted in signals from deuterated lactate and glutamate in tumour images, demonstrating the clinical applicability of the technique, although again there was no quantitative measurement of metabolic flux.

We describe here a fast 3D ^{2}H imaging sequence that allowed us to follow in a murine lymphoma model, with a time resolution of 10 minutes, the kinetics of [6,6'-$^{2}H_2$]glucose conversion to [3,3'-$^{2}H_2$]lactate following a bolus injection of labelled glucose. Referencing the glucose and lactate ^{2}H signals to the natural abundance signal from water allowed us to produce maps of tumour glycolytic flux, which showed a significant decrease within 48 h of drug treatment, demonstrating the potential of this method for assessing early tumour responses to treatment in the clinic.

6.2 Methods

6.2.1 Cell culture and tumour induction

EL4 murine lymphoma cells were grown in RPMI medium with 2 mM L-glutamine and 10% non-treated fetal calf serum (Gibco/Thermo Fisher Scientific). Cell numbers and viability were measured using a Cell counter (Vi-Cell XR, Beckman Coulter). Tumours were induced by subcutaneous injection of $5x10^{6}$ viable EL4 cells in 0.2 mL PBS into the flank of female C57BL/6 mice (Charles River). Tumours were allowed to grow for 7 to 10 days until they reached a diameter of ~14 mm. All procedures were carried out under the authority of project

and personal licenses issued by the Home Office, UK and were approved by local Animal Welfare and Ethical Review Bodies.

6.2.2 Magnetic resonance spectroscopy and imaging

For ^{2}H experiments *in vivo* the home-built surface transmit/receive coil, introduced in chapter 3, with an inner diameter of 14 mm was used. Anatomical ^{1}H reference images were acquired with a volume transmit/receive coil (Rapid Biomedical). Experiments were performed using a 9.4 T 20 cm bore scanner (Agilent). Animals were anesthetized by inhalation of 1–3% isoflurane (Isoflo; Abbotts Laboratories) in 75% air, 25% O2 (2 L per min) and body temperature was maintained by blowing warm air through the magnet bore. Breathing rate (~80 b.p.m.) and body temperature (37 °C) were monitored during experiments.

Prior to injection of 2g/kg D-[6,6′-$^{2}H_2$]glucose, the ^{2}H channel pulse power was calibrated to give, with a *TR* of 260 ms, a maximum steady state natural abundance HDO signal. With this *TR* and using a literature value for the T_1 of HDO of 320 ms[23] the effective flip angle (*FA*) of this pulse was 64° ($FA = \arccos(-TR/T_{1,water}) \cong 64°$ (Ernst angle)). For spectroscopic measurements a 7 ms 64° sinc pulse was used in the presence of a gradient to give a 10 mm slice-selective excitation. Each spectrum consisted of 512 complex points, acquired with 256 averages, a *TR* of 260 ms, and a sweep width of 2 kHz. Eighty spectra were acquired over 88 min. D-[6,6′-$^{2}H_2$]glucose (2 g/kg) (Sigma Aldrich) was injected approximately 10 s after the acquisition of the first spectrum had finished (1:06 min into the 88 min experiment). The HDO, glucose and lactate resonances were fitted using a MATLAB tool box[130] using prior knowledge of the relative chemical shifts and linewidths and the fitted peak amplitudes were multiplied by a factor that corrected for their different degrees of saturation, assuming the following T_1 times ($T_{1,water}$ = 320 ms, $T_{1,glucose}$= 64 ms, $T_{1,lactate}$ = 297 ms) [23].These were then normalized to the HDO signal from the first (pre-injection) spectrum, which was assumed to correspond to a concentration of 10.12 mM HDO [23]. Finally, a correction for the numbers of deuterons per molecule was performed to give absolute concentrations (two labels in lactate and glucose and one label in water).

For dynamic imaging a ^{2}H 3D Chemical Shift Imaging (CSI) sequence (Figure 6-1a) was developed, where an adiabatic 50° flip angle 2 ms BIR4 excitation pulse[47] was followed by

phase encoding gradients encoding a 9x9x3 k-space. Signal was acquired into 256 complex points with a bandwidth of 2 kHz and a field-of-view (*FOV*) of 27x27x27 mm^3. The k-space was sampled over 4328 transients with a repetition time (*TR*) of 140 ms in a total acquisition time of 10 min. The centre of k-space was sampled with 128 averages, with all other k-space positions sampled with fewer averages according to a Hamming window function[131] (Figure 6-1b). The order of sampling was randomized in order to avoid sampling the centre of k-space during transient metabolite concentration changes. Five images were acquired after i.v. injection of 2g/kg [6,6'-$^2H_2$]glucose into tumour-bearing mice. The five-dimensional (three spatial, one spectral and one temporal) datasets were denoised using a Tucker decomposition with a rank reduction from 9x9x3x256x5 to 5x5x2x16x3 using a MATLAB tool box[132,133]. A similar denoising algorithm has been suggested previously[31]. Rank reduction in the spectral and spatial dimensions was confirmed by phantom experiments to produce minimal blurring while still removing noise (Figure 6-2). The spectra in each voxel were analysed as described above.

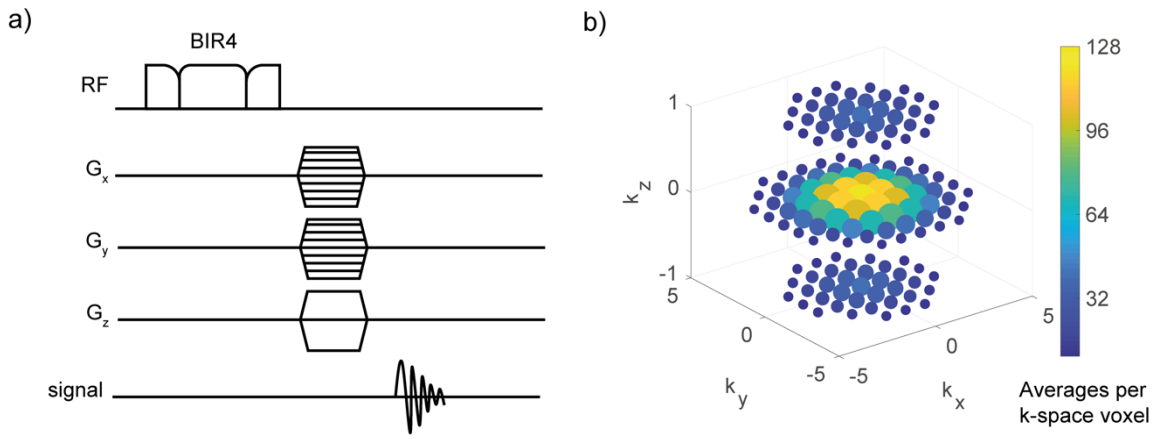

Figure 6-1. a) The ^2H 3D CSI pulse sequence used for dynamic imaging. An adiabatic excitation pulse was followed by three orthogonal phase encoding gradients. b) A 3D Hamming window weighting was used for the number of averages per k-space position. The centre of k-space was sampled with 128 averages, all other k-space positions were sampled with less averages, as shown. The order in which these k-space positions were sampled was randomized.

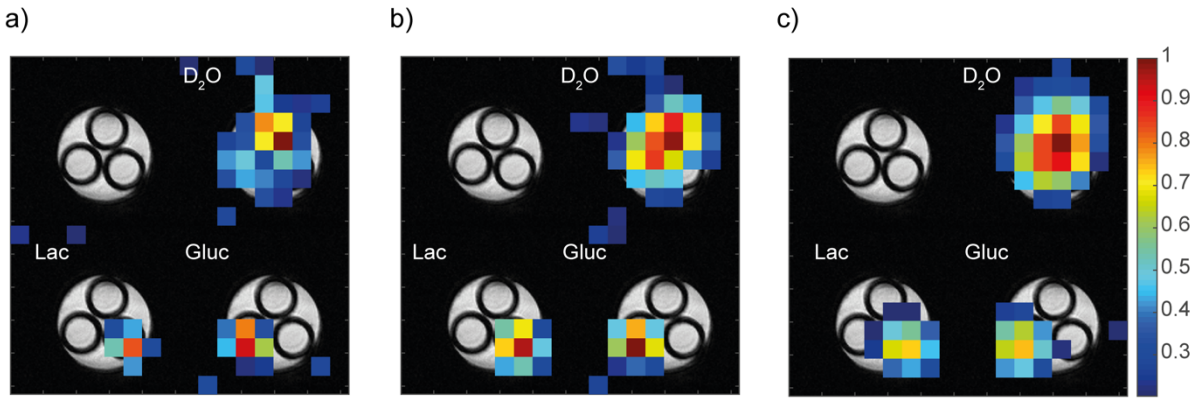

Figure 6-2. 3D ^{2}H chemical shift images of a phantom with three compartments. The compartments were filled with 20 mM $^{2}H_2O$ (upper compartment), 20 mM [6,6'-$^{2}H_2$]glucose (right compartment) and 20 mM [3,3'-$^{2}H_2$]lactate (left compartment). The space between compartments was filled with water. The top left image shows a ^{1}H reference image, the top right shows an HDO image, the bottom left a [6,6'-$^{2}H_2$]glucose image and the bottom right a [3,3'-$^{2}H_2$]lactate image. a) Reconstructed metabolite maps without denoising, b) with denoising using a Tucker decomposition with rank reduction from (9,9,3,256) to (5,5,2,16) and c) with denoising using a Tucker decomposition with a rank reduction from (9,9,3,256) to (3,3,2,8).

6.2.3 Kinetic analysis of spectroscopic and image data

The kinetics of glucose and lactate labelling from the spectroscopic data were fit to the following model:

$$\frac{\mathrm{d}[G^*]}{\mathrm{dt}} = k_g\left(a_1\, e^{-k_p t} - \frac{[G^*]}{v}\right) - fV_{max}\frac{[G^*]}{f\,v(K_M + [G^*]/f\,v)} \qquad (6.1)$$

$$\frac{\mathrm{d}[L^*]}{\mathrm{dt}} = \mathrm{f\,V_{max}}\frac{[\mathrm{G}^*]}{\mathrm{f\,v(K_M + [G^*]/f\,v)}} - \mathrm{k_l[L^*]} \qquad (6.2)$$

where *[G*]* and *[L*]* are concentrations of labelled glucose and lactate respectively, a_1, is the labelled glucose concentration immediately after the bolus injection, k_g is the apparent rate constant describing transfer of glucose between blood and tumour, k_p is the effective rate constant describing tissue uptake of labelled glucose, v is the extracellular volume fraction, V_{max} is the maximum rate of tumour glucose consumption and k_l the apparent rate constant describing labelled lactate transfer into the blood. The fractional labelling of glucose (f=0.6) was calculated from the ^{1}H and ^{2}H NMR spectra of blood samples taken during the labelling

time course as explained later (Results, Table 6-1). The model is identical to that described by Rivenzon-Segal et al[134] with the exception of the second and first terms in equations 6.1 and 6.2 respectively, which take account of the substantial depletion of labelled glucose in the study described here, which was not observed in the earlier study. The K_M in this expression is that for glucose uptake (2.8 mM)[135], which we have assumed is limiting for glycolytic flux.

Analysis of [6,6'-$^2H_2$]glucose utilization was based on a kinetic model described previously[134] that took into account changes in plasma [6,6'-$^2H_2$]glucose concentration $\left[G_p^*\right]$, which was considered to decay exponentially:

$$\left[G_p^*\right] = a_1\, e^{-k_p t} \tag{6.3}$$

where a_1 is the initial [6,6'-$^2H_2$]glucose concentration immediately after completion of the glucose injection and k_p is an effective rate constant describing loss of [6,6'-$^2H_2$]glucose from the plasma.

In the tumour, glucose is distributed between extra- and intracellular compartments, whereas the detected MR signal relates to the average concentration in the measured volume. Changes in the measured [6,6'-$^2H_2$]glucose concentration in the tumour tissue, [G*], are influenced by reversible transfer of [6,6'-$^2H_2$]glucose from the plasma, with an apparent rate constant k_g, and by the rate of glucose disappearance due to tumour metabolism V_{glc}:

$$\frac{\mathrm{d}[G^*]}{\mathrm{dt}} = k_g\left(\left[G_p^*\right] - [G_e^*]\right) - fV_{glc} \tag{6.4}$$

where $[G_e^*]$ is the concentration of [6,6'-$^2H_2$]glucose in the extracellular volume and f is the fractional deuterium enrichment of the total glucose pool. From NMR measurements of blood samples, summarized in Table 6-1, the fractional enrichment was estimated to be 0.6. The deuterated glucose that we observe is assumed to be predominantly extracellular[134]. $\left[G_p^*\right]$ is given by equation 6.3 and V_{glc} by equation 6.5.

$$V_{glc} = V_{max}\frac{[G_e]}{(K_m + [G_e])} \tag{6.5}$$

where $[G_e] = [G^*]/(f\ v)$ and is the total glucose concentration in the extracellular compartment, K_m is the K_m for glucose transport and v is the extracellular volume fraction.

This assumes that glucose transport limits the rate of glucose metabolism, which was based on the observation that glucose uptake is a rate limiting factor for glucose utilization in general[136]. Our model is different to the model used previously[134] where it was assumed that the glucose concentration was always much larger than the K_m. Glycolytic conversion of [6,6'-$^2H_2$]glucose to lactate results in the production of [3,3'-$^2H_2$]lactate and one unlabelled lactate molecule. Therefore, the rate of labelled lactate production is equal to V_{glc}, the rate of glucose disappearance due to tumour metabolism, assuming that all the glucose is converted to lactate (i.e. $V_{gly} = V_{glc}$). The change in concentration of observable ^{2}H-labeled lactate in the tumour volume, [L*], is given by:

$$\frac{\mathrm{d}[L^*]}{\mathrm{dt}} = f\,V_{gly} - k_l[L^*] \tag{6.6}$$

where k_l describes the clearance of [3,3'-$^2H_2$]lactate from the tumour. Observable lactate was assumed to be in both the intra- and extracellular tumour compartments. We neglected contributions from ^{2}H-labelled lactate in the blood as this was found to be negligible (Table 6-1). Combining equations 6.3 – 6.6 gives the coupled differential equations:

$$\frac{\mathrm{d}[G^*]}{\mathrm{dt}} = \mathrm{k_g}\left(\mathrm{a_1}\,\mathrm{e}^{-\mathrm{k_p t}} - \frac{[\mathrm{G}^*]}{\mathrm{v}}\right) - \mathrm{f\,V_{max}}\frac{[\mathrm{G}^*]}{\mathrm{f\,v}(\mathrm{K_M} + [\mathrm{G}^*]/\mathrm{f\,v})} \tag{6.7}$$

$$\frac{\mathrm{d}[L^*]}{\mathrm{dt}} = \mathrm{f\,V_{max}}\frac{[\mathrm{G}^*]}{\mathrm{f\,v}(\mathrm{K_M} + [\mathrm{G}^*]/\mathrm{f\,v})} - \mathrm{k_l}[\mathrm{L}^*]\,. \tag{6.8}$$

The experimental data were fit to these equations using the following as freely varying parameters: the plasma pharmacokinetic parameters (a_1, k_p), the rates of tissue glucose uptake from the plasma and tumour lactate clearance (k_g, k_l), the extracellular volume fraction of the tumour accessible to glucose (v) and the maximum rate of glucose consumption V_{max} (half the maximum rate of lactate synthesis).

6.2.4 Glycolytic flux maps

To calculate rate maps from the dynamic images equations 6.7 and 6.8 were simplified by replacing the term $V_{max}\frac{[G^*]}{f\,v(K_M+[G^*]/f\,v)}$ with a parameter, $V_{max}^{apparent}$, and fitting the

simplified equations to the concentration changes over time for each voxel. The number of free parameters was reduced by fixing the parameters k_p, v, k_g and k_l to the values shown in Table 6-2, which were derived from the spectroscopic time course measurements (Figure 6-3c). $V_{max}^{apparent}$ was only calculated for those voxels where the HDO signal in the first image (the concentration reference) was more than 40% of the maximum HDO signal in any one of the 9 x 9 x 3 voxels that make up the image. This prevented the introduction of errors when dividing by very noisy HDO reference data.

6.2.5 Treatment response

Thirty spectra (total acquisition time 33 min) were acquired before and another 30 at 48 h after treatment. After the first MRS measurements, and having recovered from the isoflurane anaesthesia, the animals received 67 mg/kg etoposide by i.p. injection. Peak amplitude ratios from the summed spectra acquired before and after treatment were compared using a one-sided paired t-test.

6.2.6 ^{2}H NMR of cell media

EL4 cells were seeded at a concentration of 0.5×10^6 viable cells per ml in glucose-free RPMI 1640 media (Sigma Aldrich). Supernatants were collected from five cultures and stored at -80 °C. To the remaining 15 cultures 2g/l D-[6,6′^{2}H$_2$]glucose were added and to five of these 4 mM DCA (Sigma Aldrich) and to another five flasks 10 nM rotenone (Sigma Aldrich). Twenty-four hours later the supernatants were collected and stored at -80 °C. ^{2}H NMR spectra of the supernatants were acquired at 300 K using the ^{2}H coil of a 5-mm ^{1}H/broadband inverse detection probe (Bruker Spectrospin Ltd.) on a 14.1 T high-resolution NMR spectrometer (Bruker Spectrospin Ltd., Coventry, United Kingdom). Spectra were acquired with a flip angle of 90° into 1024 data points, a spectral width of 2000 Hz and a *TR* of 2 s and were the sum of 1024 transients. After baseline correction in Topspin (Bruker Spectrospin Ltd.) the spectra were analysed in MATLAB. One sided unpaired t-tests were used to compare concentration ratios.

6.2.7 NMR of blood samples

EL4 tumour-bearing mice (n = 11) were injected with 2 g/kg D-[6,6′$^2H_2$]glucose under isoflurane anaesthesia. Blood was taken via cardiac puncture at 20, 40 and 60 min after glucose injection (n = 3). Blood from two mice was taken without prior injection of glucose. After 30 min, when the blood had clotted, the samples were centrifuged at 1500 g and to 100 µl of the supernatant was added 400 µl water and a d6-DMSO standard to a final concentration of 1.4 mM. ^{2}H NMR of the blood samples was performed using the same protocol as used for the media samples, but with a TR of 3 s. After the ^{2}H NMR experiments, a standard for proton NMR measurements (3-(trimethylsilyl)-2,2,3,3-tetradeuteropropionic acid at a final concentration of 1 mM) and 50 µl D_2O were added to the samples and ^{1}H spectra were acquired with water pre-saturation and a flip angle of 90° into 16384 data points, with a spectral width of 7788 Hz and a repetition time of 8 s.

6.3 Results

6.3.1 Dynamic ^{2}H MR spectroscopy measurements of glycolytic flux

Typical time courses of tumour glucose, lactate and water labelling following intravenous injection of a tumour-bearing mouse with 2 g/kg d-[6,6'-$^2H_2$]glucose are shown in Figure 6-3. Signal was acquired predominantly from the tumour and immediately adjacent tissue by using a slice-selective excitation pulse and because of the sensitivity profile of the surface coil, which was placed over the tumour and acquired signal largely from within a coil radius (~1 cm). Individual fitted peak amplitudes were corrected for partial signal saturation using published T_1 relaxation times and then converted into concentrations by referencing to the initial natural abundance HDO peak, which was assumed to represent a concentration of 10.12 mM[23], and by correcting for the number of deuterons per molecule.

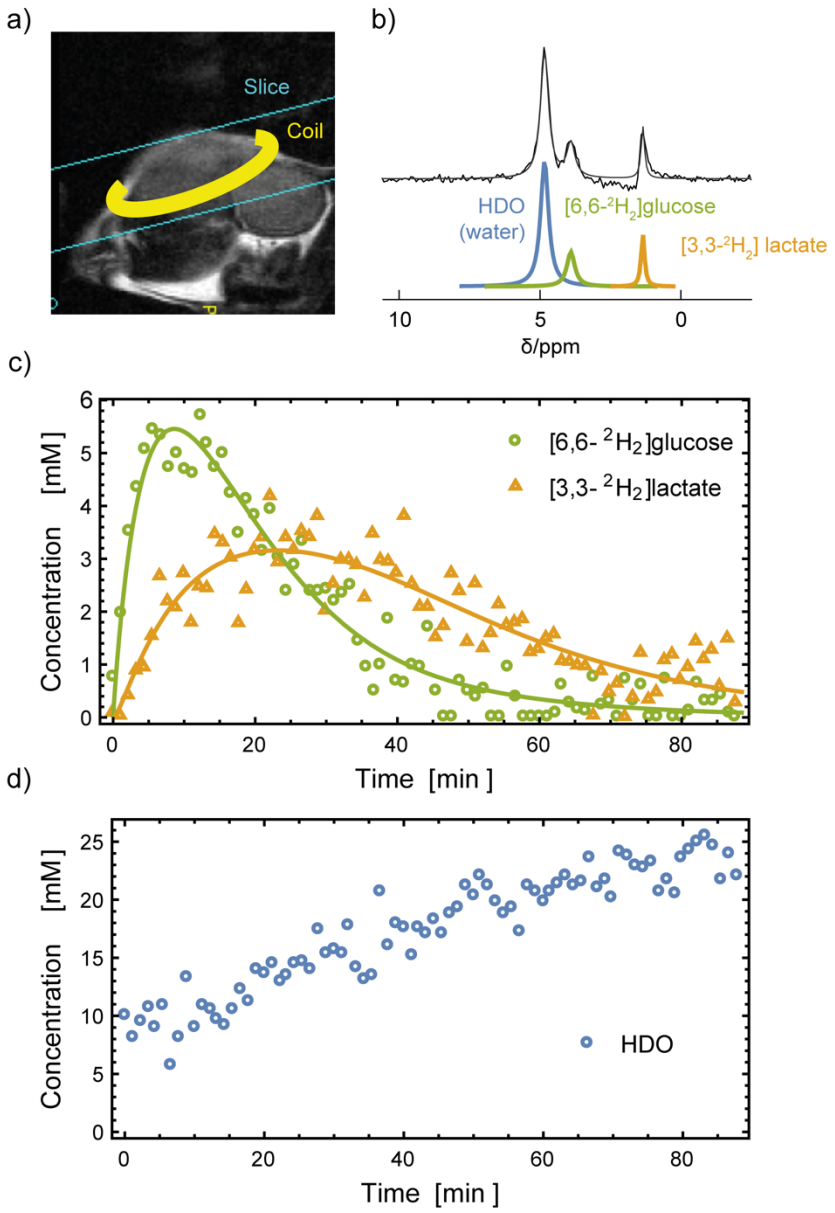

Figure 6-3. a) Sagittal ^{1}H reference image showing the position of the 10 mm slice used for dynamic ^{2}H NMR spectroscopy. The surface coil was positioned over a subcutaneous EL4 tumour. b) Sum of 80 spectra recorded in 88 min following injection of 2 g/kg [6,6'-$^{2}H_2$]glucose 10 s after acquisition of the first spectrum. The peaks were fitted individually using prior knowledge. c) Time course of labelled glucose and lactate concentrations and lines showing the best fit to the kinetic model. d) Time course of labelled water (HDO).

Glucose was observed to wash into the tumour, with the concentration peaking at ~10 min, followed by an increase in the labelled lactate concentration, which peaked at ~20 min, and then both the glucose and lactate signals declined. The labelled water signal (HDO) increased

after an initial delay of ~15 min and appeared to plateau after ~70 minutes. Deuterium can be lost from [6,6′$^2H_2$]glucose to solvent water in the pyruvate kinase-catalysed enolization of pyruvate[137] in the glycolytic pathway and in several enzyme-catalysed reactions in the TCA cycle[23,123,138]. Modulation of TCA cycle flux in the tumour cells in culture showed that at least some of the labelled water observed in the tumour could have been labelled via flux in the tumour cell TCA cycle. Cells were incubated for 24 h with 11 mM [6,6′$^2H_2$]glucose and either dichloroacetate (DCA), which increases flux into the TCA cycle[139], or rotenone, which decreases TCA cycle flux[140]. The concentrations of ^{2}H-labelled glucose, lactate and water were then determined by ^{2}H NMR (Figure 6-4). At the concentrations used DCA and rotenone had little effect on cell proliferation or viability. Viable cell counts (and viability) were 0.52±0.04x10^6 /ml (92.2±0.77 %) at t=0 and 1.08±0.11x10^6 /ml (93.96±1.06 %) in control cultures, 1.15±0.24x10^6 /ml (95.39±0.59 %) in DCA-treated cultures and 1.12±0.11x10^6 /ml (92.49±0.78%) in rotenone-treated cultures after 24 h. The errors are standard deviations with five biological replicates used for each group. DCA decreased the glucose consumption and lactate production rates, whereas rotenone had the reciprocal effect, consistent with their expected effects on TCA cycle flux. The ratio of the water labelling and glucose consumption rates (Figure 6-4g) showed that in control cells there was 6.9±1.8 (S.E.M.) % of the glucose label lost to water, which is similar to previous estimates of 8.1±2.3% [23] and 6-14% [137] for ^{2}H label loss in glycolysis estimated from an analysis of lactate labelling in brain tumour cells incubated with [6-^{13}C,6,6′-$^2H_2$]glucose. DCA increased the ratio to 8.6±1.5% whereas rotenone decreased it to 2.9±2.0%, such that there was a significant ($p<0.05$) difference in the ratios obtained following DCA or rotenone treatment, implying that at least some of the deuterium label was lost to water in the tumour cell TCA cycle. A similar conclusion could be reached by comparing the water labelling and lactate production rates (Figure 6-4h). However, measurements of labelled lactate and water concentrations in blood samples taken from tumour-bearing mice before and at 20, 40 and 60 min after injection of 2 g/kg [6,6′$^2H_2$]glucose (Table 6-1) showed that the much of the labelled water in the tumours, but not lactate, must have washed into the tumour from other tissues in the body rather than being generated endogenously. HDO in the blood reached a concentration of 34±1 mM at 60 min, as compared to 23±1 mM in the tumour.

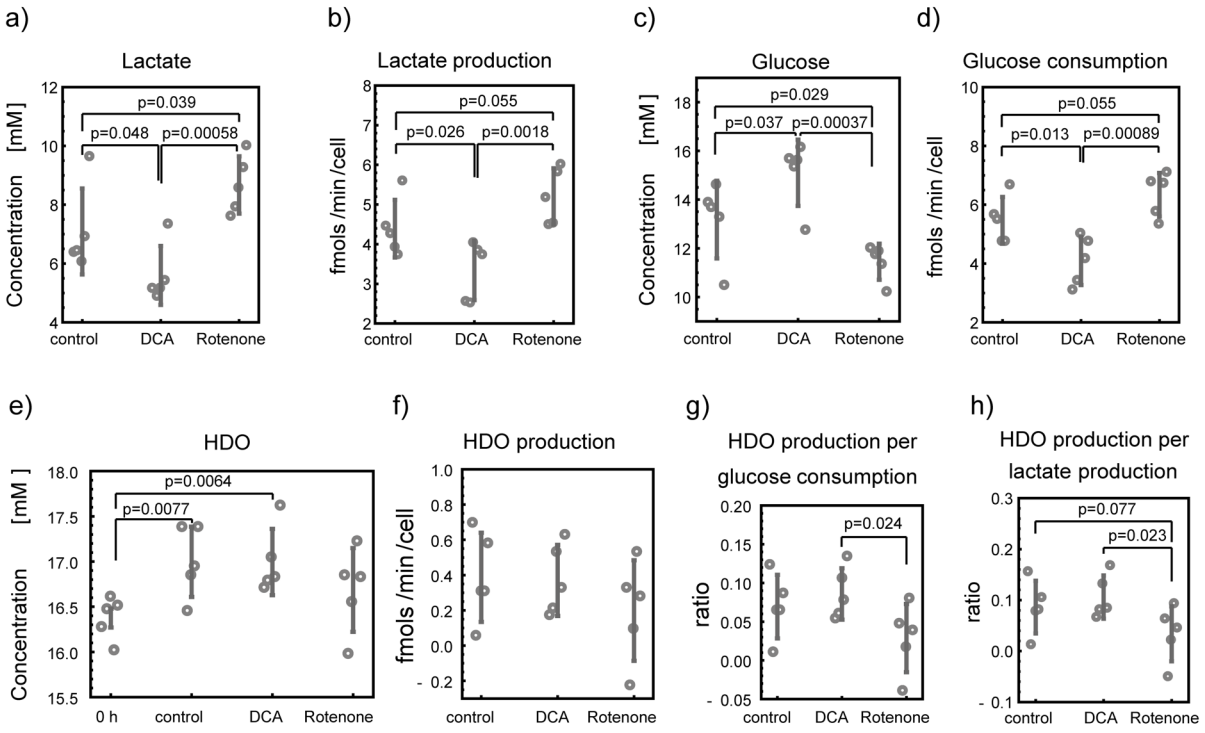

Figure 6-4. Concentrations of deuterium label in glucose, lactate and water in EL4 cell suspensions that had been incubated with 11 mM [6,6′2H2]glucose and 4 mM dichloroacetate (DCA) or 10 nM rotenone. a) Lactate deuterium concentration after 24 h. b) Lactate deuterium production rate. c) Glucose deuterium concentration after 24 h. d) Glucose deuterium consumption rate. e) HDO concentration, initially and after 24 h, f) HDO production rate. g) Ratio of HDO production and glucose consumption rates. h) Ratio of HDO and lactate production rates.

Wash in from the rest of the body could also explain the delay in its appearance in the tumour (Figure 6-3). Wash in of labelled lactate, however, cannot explain the lactate labelling observed in the tumour. Labelled lactate concentrations in the blood reached a maximum of 0.4±0.3 mM at 20 min (Table 6-1), which is only ~10% of the labelled lactate concentration observed in the tumour (Figure 6-3), indicating that the bulk of labelled lactate in the tumour came from tumour glycolysis.

Table 6-1. Metabolite labelling in blood

Metabolite	Concentrations at the specified times following injection of [6,6′$^2H_2$]glucose (mM)		
	20 min	40 min	60 min
[6,6′-$^2H_2$]glucose	10.9±6.6	2.5±1.6	1.9±0.2
Total glucose	13.8±4.3	6.9±1.0	3.2±1.7
[3,3′-$^2H_2$]lactate	0.4±0.3	0.4±0.2	n.d.
Total lactate	16.9±1.4	12.4±1.9	9.5±1.5
HDO	25±4.1	35.4±2.7	33.9±0.7

Labelled concentrations were measured using ^2H NMR. Total glucose concentration was measured using ^1H NMR. Blood was collected by cardiac puncture at the specified times after i.v. injection of 2g/kg [6,6′$^2H_2$]glucose into EL4 tumour-bearing mice. Data are expressed as mean ± S.E.M. (n = 3, except for lactate concentration at 60 min where n = 2). n.d., not detected.

The glucose and lactate deuterium signals in the tumour could be fit to a kinetic model of glycolysis that was similar to a model described previously[134] (Table 6-2). The maximum rate of tumour glucose consumption in glycolysis (V_{max}) was estimated to be 0.88±0.09 mM/min, which is comparable to a value of 1.57 μmol/g/min (1.43 mM/min assuming 1 ml tissue weighs 1.1 g) measured in breast cancer xenografts[141]. Assuming a cell density in the tumours of 5 x 10^8 /ml[142] this maximum rate of tumour glucose consumption measured *in vivo* corresponds to a rate of 1.77±0.18 fmol/min/cell, which is similar to the rates of labelled lactate production (2.16±0.16 fmol/min/cell) and glucose consumption (2.7±0.18 fmol/min/cell) determined for the cells *in vitro* (Figure 6-4b & d) and also to published values for human leukemic cells of 2.10 – 3.57 fmol/min/cell[143].

Table 6-2. Parameter estimates derived from measurements of tumour glucose and lactate labelling following injection of [6,6′-$^{2}H_2$]glucose.

	Description	Estimate	Standard Error
a_l	Labelled glucose concentration immediately after the bolus injection (mM).	17.0	6.5
k_p	Effective rate constant of labelled glucose transfer to tissue (min^{-1}).	0.0416	0.0030
V	Extracellular volume fraction.	0.65	0.24
k_g	Apparent rate constant describing transfer of glucose between blood and tumour (min^{-1}).	0.127	0.048
V_{max}	Maximum rate of glucose consumption (mM min^{-1})	0.883	0.089
k_l	Apparent rate constant describing labelled lactate transfer to the blood (min^{-1}).	0.124	0.021

6.3.2 Dynamic ^{2}H imaging of glucose metabolism

The spectroscopic data (Figure 6-3) demonstrated that an imaging sequence would need a temporal resolution of ~10 min in order to observe the transient changes in labelled metabolite concentrations. We therefore developed a 3D ^{2}H CSI pulse sequence which was a compromise between temporal and spatial resolution; with a matrix size of 9x9x3 and a field-of-view of 27x27x27mm this gave a nominal spatial resolution of 3x3x9 mm and a temporal resolution of 10 min. Sampling of k-space was randomized in order to minimize bias introduced by metabolite concentration changes taking place during sampling of the centre of k-space and a 3D Hamming window weighting was used for the number of averages per k-space position (Figure 6-1). Application of tensor decomposition, which has been used recently for denoising non-hyperpolarized ^{13}C images[31], improved the image signal-to-noise ratio (Figure 6-2 and Figure 6-6). The spectra in each voxel were fitted using prior knowledge of the relative chemical shifts and linewidths[130] and peak amplitudes were converted into concentrations using the intensity of the HDO signal in the first HDO image as a reference[23]. A series of images acquired following the injection of labelled glucose, overlaid on the corresponding ^{1}H image, are shown in Figure 6-5. Glucose appeared rapidly in the tumour and throughout the body of

the animal, concentrating in a region that included the bladder whereas labelled water and lactate, which showed a similar distribution, also appeared throughout the body of the animal but concentrated subsequently in the tumour. The relative uniformity of the early water and lactate images demonstrates the effectiveness of normalizing to the initial HDO signal in compensating for the B_1 field gradient of the surface coil.

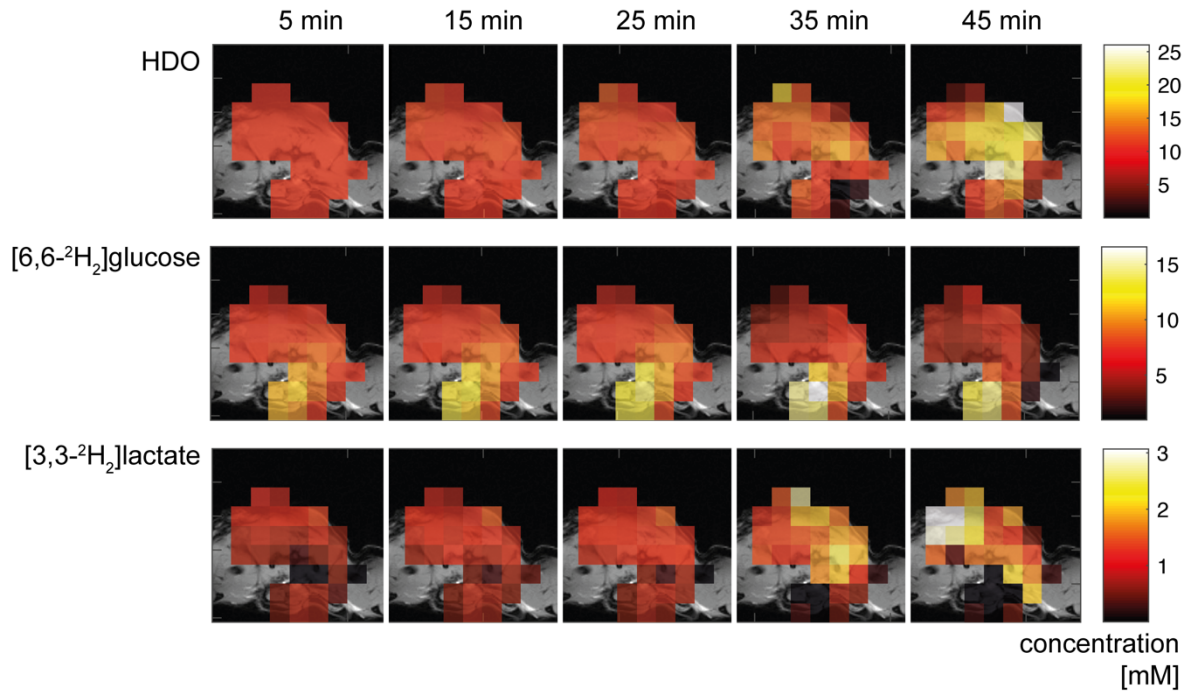

Figure 6-5 Metabolite concentration maps calculated from 3D CSI images acquired at the specified times following injection of 2g/kg [6,6'-$^2H_2$]glucose into an EL4 tumour-bearing mouse. The colour coding represents concentrations (in mM) derived from the ratios of the peak amplitudes to the initial HDO map and corrected for the number of ^2H labels per molecule and for signal saturation. a) HDO, b) glucose and c) lactate concentration maps.

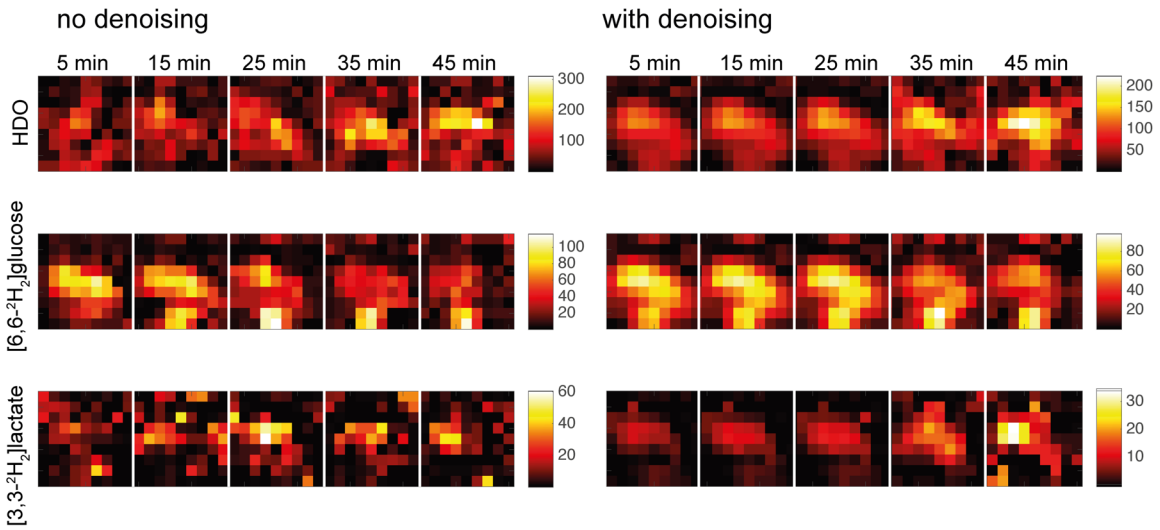

Figure 6-6. Reconstructed metabolite images before referencing to HDO, acquired *in vivo* without denoising (left) and with denoising using a Tucker decomposition with rank reduction from (9,9,3,256,5) to (5,5,2,16,3) (right).

6.3.3 Treatment response

Treatment of tumour-bearing animals with 67 mg/kg etoposide resulted in significant decreases in the tumour lactate/HDO and tumour lactate/glucose signal ratios in spectra acquired at 48 h after treatment ($n = 5$, $p < 0.05$, pairwise one-sided t-test) (Figure 6-7). Fitting a series of dynamically acquired images, on a voxel-by-voxel basis, to the kinetic model was used to create a rate map, which showed that the rate of lactate labelling was heterogeneous across the tumour (Figure 6-8). Following treatment there was a decrease in the rate of lactate labelling, mirroring the decrease in lactate labelling observed in the spectroscopic data (Figure 6-7).

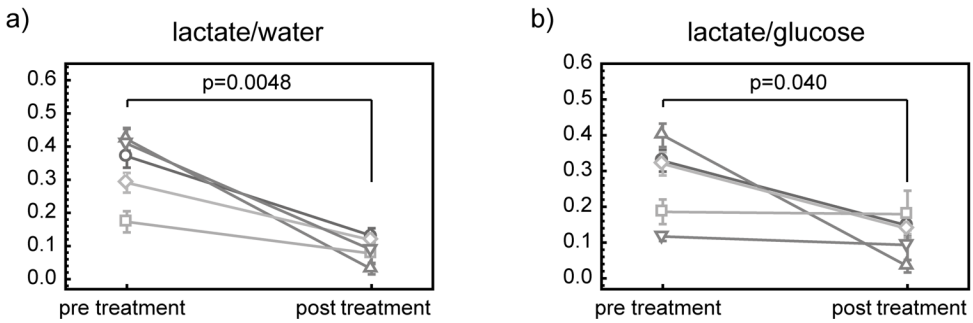

Figure 6-7. Response of EL4 tumours to treatment with etoposide. Spectra were acquired before and 48 h after treatment and were the sum of 7680 averages acquired with a *TR* of 260 ms in 33 min. There were significant decreases (one-sided paired t-test) in a) the [3,3'-$^2H_2$]lactate /HDO ratio and b) [3,3'-$^2H_2$]lactate/[6,6'-$^2H_2$]glucose ratio at two days after treatment.

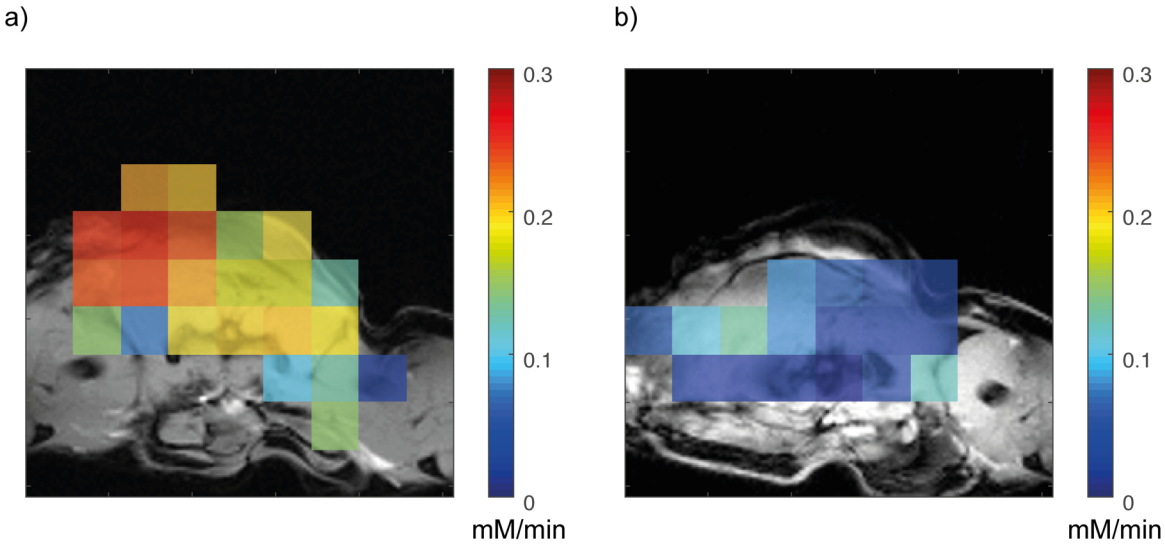

Figure 6-8. Glucose consumption rate maps ($V_{max}^{apparent}$) a) before and b) after etoposide treatment.

6.3.4 Discussion

Several studies have used MRS measurements of isotopically labelled glucose to investigate glycolytic metabolism *in vivo*. Rivenzon-Segal *et al.*[134] infused [1-^{13}C]glucose over a period of 10 min and at a similar concentration to that used here to investigate glycolytic flux in an orthotopic breast cancer model. Acquisition of 5 min ^{13}C MR spectra from the tumour for up to 80 minutes showed much higher tumour glucose concentrations and much lower lactate production rates than were observed here. Consistent with these observations, estimation of glycolytic flux from the spectroscopic data acquired here, using a similar kinetic model to that used by Rivenzon-Segal *et al.*[134], gave a V_{max} of 0.88±0.09 mM/min, which is much higher than that measured by Rivenzon-Segal *et al.*(0.045 mM/min) but comparable to a value of 1.43 mM/min measured in another breast cancer model[141]. This higher value is also comparable to the rates of lactate production and glucose consumption that we measured here in EL4 cells *in vitro* and to values reported previously for human leukemic cells[143]. Infusion of hyperpolarized [U-^{2}H,U-^{13}C]glucose at 0.3 g/kg, which is approximately one sixth the glucose concentration used here, into the same EL4 tumours, resulted in observation of hyperpolarized [1-^{13}C]lactate *in vivo* and a measured labelled lactate concentration in tumour extracts at 20 and 150 s after glucose injection of 0.49±10 and 1.9±0.4 mM[12]. This is similar to the average concentration of ^{2}H labelled lactate measured here in tumours *in vivo* between 1 and 3 minutes after glucose injection (0.4±0.2 mM; Figure 6-3). Borowiak *et al.*[144] injected mice with glucose labelled with ^{17}O on position C6, which is released into solvent water in the reaction catalysed by the glycolytic enzyme enolase, and used ^{17}O MRS measurements of water labelling to estimate the apparent cerebral metabolic rate of glucose in mouse brain. In a similar study Lu *et al.*[123] measured cerebral glucose consumption rate in rat brain by infusing animals with [6,6'-$^{2}H_2$]glucose and measuring the kinetics of brain glucose, lactate and water labelling using ^{2}H MRS. Their value for glucose consumption of 0.28±0.13umol/g/min or 0.25±0.12 mM/min (assuming 1 ml tissue weighs 1.1 g) is much lower than that measured here, reflecting the predominantly oxidative metabolism of brain and other non-neoplastic tissues. Recently intravenous [6,6'-$^{2}H_2$]glucose infusion in a rat glioma model and oral administration in glioma patients has been combined with ^{2}H imaging to investigate glycolytic and TCA cycle activities in glioma[23]. This study showed increased lactate labelling and decreased glutamate/glutamine labelling in the tumour, when compared to normal brain, demonstrating the expected increased

glycolytic activity and decreased oxidative metabolism in the tumour. Similar observations had been made previously using mass spectrometry measurements of lactate and glutamate labelling in excised tumours from glioma patients that had been infused with ^{13}C-labelled glucose immediately prior to surgery[145] and in similar studies in patient-derived xenograft models of glioma[146]. The failure to observe glutamate labelling in the lymphomas used here can be explained by their much lower oxygen consumption rates and TCA cycle activities when compared to healthy brain and glioma cells. The EL4 cell oxygen consumption rate has been measured at 7.7 amol/cell /s[147] as compared 30 to 130 amol/cell/s in glioma cells[148].

Deuterons can be lost from [6,6'-$^{2}H_2$]glucose to water in the glycolytic pathway[137] and in the TCA cycle[23,123,138]. Therefore, in principle, tumour TCA cycle activity could also be assessed by measuring the rate of water labelling. Although we found some evidence for TCA cycle-dependent labelling of water in EL4 cells in culture, *in vivo* the labelled water in the tumour appeared to arise predominantly from wash in from other tissues in the body. This was not the case for lactate and, in agreement with the work of De Feyter *et al.*[23], the blood lactate concentration was much lower than that in the tumour and therefore the kinetics of tumour lactate labelling can provide a measure of glycolytic flux.

Injection of hyperpolarized [U-^{2}H,U-^{13}C]glucose allowed imaging of tumour glycolysis, although not an estimate of glycolytic rate[149]. More recently, Brender *et al.*[31] showed that dynamic images of tumour glucose consumption and lactate production could be acquired with non-hyperpolarized ^{13}C-labeled glucose by using tensor decomposition, which effectively used all of the signal collected during 90 minutes of acquisition to generate a time series of individual images. Application of a similar denoising technique to the individual ^{2}H images acquired here improved their signal-to-noise (Figure 6-2 and Figure 6-6) but was not essential, which was the case for the non-hyperpolarized ^{13}C images[31]. Furthermore, referencing the ^{2}H signals from glucose and lactate to the internal concentration standard provided by the HDO resonance allowed us to compensate for the inhomogeneous B_1 field of the surface coil used for data acquisition and, more importantly, to quantify the concentrations of labelled glucose and lactate (Figure 6-5).

6.3.5 Conclusion

In summary, we have shown that by administering ^{2}H labelled glucose as a bolus and by using a rapid 3D spectroscopic imaging sequence that we can acquire dynamic images of glucose metabolism with a time resolution of 10 min and derive quantitative maps of glycolytic flux (Figure 6-8). We have also shown that measurements of [6,6′-$^{2}H_2$]glucose metabolism can provide early evidence of treatment response. The work of De Feyter *et al.*[23] in glioma patients has shown that assessing treatment response with [6,6′-$^{2}H_2$]glucose in this way could readily translate to the clinic.

Chapter 7 Summary

The aim of this thesis was to develop and test novel methods for probing metabolism *in vivo* with isotopically labelled metabolites and MR detection. Two very different methodologies were presented. The first used substrates where a low gamma nucleus (^{13}C or ^{15}N) was hyperpolarized using dDNP and a pulse sequence transferred the hyperpolarization to spin coupled protons shortly before detection (chapter 2, 4 and 5). The second used a bolus injection of ^{2}H-labelled thermally polarized glucose and subsequent fast ^{2}H MRSI to map tumour glycolytic flux *in vivo* (chapter 4). In summary the following was reported.

7.1 Measurement of LDH activity with ^{1}H detected ^{13}C hyperpolarization

An effective way to repetitively transfer hyperpolarization via indirect spin-spin coupling between [1-^{13}C] and [3,3,3-$^{1}H_3$] in [1-^{13}C]lactate, which is formed enzymatically from hyperpolarized [1-^{13}C]pyruvate, was demonstrated theoretically, in simulations and by NMR spectroscopic experiments. Because of the stronger coupling and the bigger chemical shift difference with water, polarization was transferred into the three magnetically equivalent methyl protons in lactate (J_{CH} = 4.1 Hz and σ = 1.32 ppm) rather than the C2 proton (J_{CH} = 3.2 Hz and σ = 4.125 ppm). In experiments with thermally polarized [1-^{13}C]lactate, the efficiency was determined to be ~70%. By injecting hyperpolarized [1-^{13}C]pyruvate into a solution containing known amounts of LDH, the enzyme that catalyses interconversion of pyruvate and lactate, and repeated application of a lactate resonance-selective reverse INEPT sequence, dynamic proton detection of hyperpolarized [3,3,3-$^{1}H_3$]lactate was achieved. The time course of changes in the [3,3,3-$^{1}H_3$]lactate resonance intensity was fitted to a kinetic model. Reducing the amount of enzyme was mirrored by a decrease of the slope of the decay of the log of the lactate signal. Proton detection of [1-^{13}C]lactate therefore has the potential to investigate LDH

activity. The method set the stage for dynamic hyperpolarized ^{1}H imaging, which was later implemented by Jiazheng Wang[90]. The method was furthermore picked up by the MR community and adapted for use on a clinical scanner[91].

7.2 Development of RF coils

Three different RF coils were built: One for ^{13}C to ^{1}H hyperpolarization transfer at 7 T, one for ^{15}N to ^{1}H hyperpolarization transfer at 7 T and one for deuterium metabolic imaging at 9.4 T. The double-resonant coils followed the design proposed by Wetterling *et al.*[101] and the ^{2}H coil was a single loop surface coil with balanced[94] matching. The double-resonant coils were both used successfully for polarization transfer pulse sequences with simultaneous pulsing on the two frequencies (chapter 4 and 5). Measurement of the Q-ratio (chapter 3) for the ^{2}H coil showed that, as expected[96], the coil noise is dominant at the relatively low frequency (61.44 MHz at 9.4 T). Here the use of cryogenically cooled coils[150] would contribute a lot to further noise reduction. Sanchez *et al.* report for ^{13}C at 3 T a 1.6-fold increase in SNR (corresponding to an acceleration factor of two) with a coil at 105 K [151] . Unfortunately such cold probes are only available at very high initial purchase and maintenance costs[150].

7.3 Partial hyperpolarization transfer in [$^{15}N_2$]urea

A B_1 insensitive nuclear enhancement through polarization transfer (BINEPT) pulse sequence[109] was modified for partial transfer of polarization, as is required for dynamic measurements. It was shown that this new ImpeRfection RobUst Partial Transfer (IRRUPT) sequence is stable over a range of B_1 field inhomogeneity, which will facilitate translation to *in vivo* applications. With this sequence, both the long T_1 offered by storing polarization in the ^{15}N nucleus and the higher sensitivity of ^{1}H detection can be exploited. The sequence was demonstrated with dynamic spectroscopic and imaging measurements of hyperpolarized [$^{15}N_2$]urea. When compared to direct ^{15}N detection, the sequence increased the signal-to-noise ratio (SNR) by a factor of 1.72±0.25, where both experiments depleted ~20% of the available hyperpolarization. The SNR improvement is even larger when larger amounts of the hyperpolarization are used per acquisition (>10-fold when 100% of the available

hyperpolarization is used). Measuring the SNR efficiency of the home-built coil with a thermally polarized [$^{15}N_2$]urea phantom allowed estimation of the maximal achievable SNR improvement using indirect detection with this coil. This theoretical limit was compared to the SNR improvement measured with interleaved direct and indirect measurements of a single hyperpolarized [$^{15}N_2$]urea dissolution. The comparison showed that the measured improvement was close to the maximal achievable improvement for this coil. With higher levels of ^{15}N polarization the sequence will also give a significant SNR benefit when compared to direct ^{13}C detection.

7.4 Partial hyperpolarization transfer in [2-^{13}C]pyruvate

The IRRUPT sequence was adapted for partial polarization transfer to the methyl protons in [2-^{13}C]pyruvate. In this substrate spin-spin coupling is much weaker than in [$^{15}N_2$]urea (6.1 Hz vs 90 Hz). This had the disadvantage of longer delays in the sequence, which inevitably lead to more relaxation losses during the transfer. On the other hand, polarization transfer in this molecule is stable over an even larger parameter range when compared to transfer in [$^{15}N_2$]urea. This is because in the latter case, the adiabatic pulses are long compared to the timescale of the evolution of the *J*-coupling. In [2-^{13}C]pyruvate the evolution is slower and therefore has a negligble influence during the adiabatic pulses.

Dynamic proton images and spectra of [2-^{13}C]pyruvate were acquired successfully using the IRRUPT sequence with the home-built ^{1}H/^{13}C transmit/receive surface coil.

Recently hyperpolarized [2-^{13}C]pyruvate has been used for the first time in humans[120]. A pulse sequence that transfers 100% of the hyperpolarization in [2-^{13}C]lactate produced *in vivo* from hyperpolarized [2-^{13}C]pyruvate has furthermore been demonstrated *in vivo* in a rat on a clinical scanner[91]. The evidence from those two studies strongly suggests that the IRRUPT sequence for partial transfer in hyperpolarized [2-^{13}C]pyruvate can be adapted for use in patients on clinical scanners.

7.5 Measurement of glycolytic flux with deuterium magnetic resonance imaging

A fast 3D deuterium MRSI pulse sequence, with a time resolution of 10 minutes, was developed. The sequence was used to image glycolytic flux in a murine tumour model following a bolus injection of D-[6,6'-$^{2}H_2$]glucose. I believe this to be the first demonstration of quantitative mapping of glycolytic flux *in vivo*. Neither FDG-PET nor ^{13}C MRSI of hyperpolarized [1-^{13}C]pyruvate metabolism can give the kind of information necessary to extract quantitative fluxes because they cannot be referenced to known concentrations (hyperpolarized [1-^{13}C]pyruvate) or don't report on downstream metabolites (FDG-PET).

The deuterium spectroscopic images showed heterogeneity in glycolytic flux across the tumour and a decrease 48 h after treatment. Spectroscopic measurements showed a significant decrease in lactate labelling. As shown by the work of De Feyter *et al.*[23] in glioma patients these type of sequences can be rapidly adapted to a clinical setting.

7.6 General conclusion

Both methods, proton detection of hyperpolarized low gamma nuclei as well as the deuterium magnetic resonance imaging-based mapping of glycolytic flux are ready for clinical translation.

Recently polarization transfer has been demonstrated on a clinical scanner[91]. With the introduction (chapter 4 and 5) of the ImpeRfection Robust Partial Transfer sequence (IRRUPT) and experimental proof that the SNR can be enhanced by indirect detection (chapter 4), I believe that this could add momentum to clinical translation.

The DMI based imaging of glycolytic flux (chapter 6) is easy to implement on clinical MR scanners. DMI has already been shown to work on cancer patients[23] and the number of cancer patients undergoing DMI has been increasing since this first study[152]. The main problem with this method is the still low sensitivity. However, there are several ways that this may be overcome. Improving the magnetic field homogeneity or going to higher field strengths[153] are the obvious approaches. A further brute force step would be the use of cryogenic coils, which should further improve sensitivity, especially because detection at relatively low frequencies

benefits disproportionately from the removal of coil noise[96,150,151]. On the post processing side, denoising algorithms, as we have used, can be implemented more radically to help recovering sparse signal from the noise. This has been demonstrated by Brender *et al.*[31] and Kishimoto *et al.*[154] with MRSI of thermally polarized ^{13}C labelled metabolites.

When ours and related DMI methods are developed to their full potential they could replace some FDG-PET imaging of cancer patients if spatial resolution is not a top priority and a quantitative assessment of glycolytic flux is required, or if a region needs to be examined where FDG-PET doesn't work well, such as in the prostate[4,127] or brain[155,156]. This will benefit the patient because of the absence of ionizing radiation. Currently (July 2019), 50 g of [6,6′-$^{2}H_2$]glucose, which is the amount needed for DMI of a 70 kg patient,[23] cost between £4000 (Cambridge Isotopes, 10 g for $670) and £5500 (Sigma Aldrich, 1 g for £105) which makes DMI expensive compared to FDG-PET, where the tracer costs between £400 and £1000 [157]. However, if [6,6′-$^{2}H_2$]glucose was produced in larger batches, then the price will likely decrease. The amount needed per patient might also be reduced by i.v. injection instead of oral administration. Furthermore, the high initial costs of installing a PET scanner (~$1,770,000 [158]) will make DMI attractive for those hospitals where a MRI scanner but not a PET scanner is installed. In the future, clinical translation of DMI may therefore also benefit the healthcare system due to lower initial costs and potentially lower tracer costs.

References

1. Eisenhauer, E. A. *et al.* New response evaluation criteria in solid tumours: Revised RECIST guideline (version 1.1). *Eur. J. Cancer* **45**, 228–247 (2009).

2. Stroobants, S. *et al.* 18FDG-Positron emission tomography for the early prediction of response in advanced soft tissue sarcoma treated with imatinib mesylate (Glivec®). *Eur. J. Cancer* **39**, 2012–2020 (2003).

3. Campbell, A., Davis, L. M., Wilkinson, S. K. & Hesketh, R. L. Emerging Functional Imaging Biomarkers of Tumour Responses to Radiotherapy. *Cancers (Basel).* **11**, 131 (2019).

4. Brindle, K. New approaches for imaging tumour responses to treatment. *Nat. Rev. Cancer* **8**, 94–107 (2008).

5. Marusyk, A. & Polyak, K. Tumor heterogeneity: Causes and consequences. *Biochim. Biophys. Acta - Rev. Cancer* **1805**, 105–117 (2010).

6. Sotiriou, C. & Piccart, M. J. Taking gene-expression profiling to the clinic: when will molecular signatures become relevant to patient care? *Nat. Rev. Cancer* **7**, 545–553 (2007).

7. Warburg, O., Wind, F. & Negelein, E. The Metabolism of Tumors in the Body. *J. Gen. Physiol.* **8**, 519–530 (1927).

8. Heiden MGV, Cantley LC & Thompson CB. Understanding the Warburg Effect: The Metabolic Requirements of Cell Proliferation. *Science (80-.).* **324**, 1029–1033 (2010).

9. Koppenol, W. H., Bounds, P. L. & Dang, C. V. Otto Warburg's contributions to current concepts of cancer metabolism. *Nat. Rev. Cancer* **11**, 325–337 (2011).

10. Pavlova, N. N. & Thompson, C. B. The Emerging Hallmarks of Cancer Metabolism.

Cell Metab. **23**, 27–47 (2016).

11. Van De Wiele, C., Kruse, V., Smeets, P., Sathekge, M. & Maes, A. Predictive and prognostic value of metabolic tumour volume and total lesion glycolysis in solid tumours. *Eur. J. Nucl. Med. Mol. Imaging* **40**, 290–301 (2013).

12. Rodrigues, T. B. *et al.* Magnetic resonance imaging of tumor glycolysis using hyperpolarized 13C-labeled glucose. *Nat. Med.* **20**, 93–7 (2014).

13. Ardenkjaer-Larsen, J. H. *et al.* Increase in signal-to-noise ratio of >10,000 times in liquid-state NMR. *Proc. Natl. Acad. Sci.* **100**, 10158–10163 (2003).

14. Von Morze, C. *et al.* Imaging of blood flow using hyperpolarized [13C]urea in preclinical cancer models. *J. Magn. Reson. Imaging* **33**, 692–697 (2011).

15. Golman, K., Zandt, R. I. t., Lerche, M., Pehrson, R. & Ardenkjaer-Larsen, J. H. Metabolic imaging by hyperpolarized 13C magnetic resonance imaging for in vivo tumor diagnosis. *Cancer Res.* **66**, 10855–10860 (2006).

16. Golman, K., in 't Zandt, R. & Thaning, M. Real-time metabolic imaging. *Proc. Natl. Acad. Sci.* **103**, 11270–11275 (2006).

17. Nelson, S. J. *et al.* Metabolic imaging of patients with prostate cancer using hyperpolarized [1-^{13}C]pyruvate. *Sci. Transl. Med.* **5**, 198ra108 (2013).

18. Day, S. E. *et al.* Detecting tumor response to treatment using hyperpolarized 13C magnetic resonance imaging and spectroscopy. *Nat. Med.* **13**, 1382–1387 (2007).

19. Day, S. E. *et al.* Detecting Response of Rat C6 Glioma Tumors to Radiotherapy Using Hyperpolarized [1-13C]Pyruvate and 13C Magnetic Resonance Spectroscopic Imaging. *Magn. Reson. Med.* **65**, 557–563 (2011).

20. Gallagher, F. a *et al.* Production of hyperpolarized [1,4-13C2]malate from [1,4-13C2]fumarate is a marker of cell necrosis and treatment response in tumors. *Proc. Natl. Acad. Sci. U. S. A.* **106**, 19801–19806 (2009).

21. Düwel, S. *et al.* Multiparametric human hepatocellular carcinoma characterization and therapy response evaluation by hyperpolarized 13C MRSI. *NMR Biomed.* **29**, 952–960 (2016).

22. Aggarwal, R., Vigneron, D. B. & Kurhanewicz, J. Hyperpolarized 1-[13C]-Pyruvate Magnetic Resonance Imaging Detects an Early Metabolic Response to Androgen Ablation Therapy in Prostate Cancer. *Eur. Urol.* **72**, 1028–1029 (2017).

23. De Feyter, H. M. *et al.* Deuterium metabolic imaging (DMI) for MRI-based 3D mapping of metabolism in vivo. *Sci. Adv.* **4**, eaat7314 (2018).

24. Kuo, D. J. & Rose, I. A. Aconitase, source of catalytic protons. *Biochemistry* **26**, 7589–7596 (1987).

25. Ceccarelli, C., Grodsky, N. B., Ariyaratne, N., Colman, R. F. & Bahnson, B. J. Crystal structure of porcine mitochondrial NADP +-dependent isocitrate dehydrogenase complexed with Mn 2+ and isocitrate: Insights into the enzyme mechanism. *J. Biol. Chem.* **277**, 43454–43462 (2002).

26. Horsefield, R. *et al.* Structural and Computational Analysis of the Quinone-binding Site of Complex II (Succinate-Ubiquinone Oxidoreductase). *J. Biol. Chem.* **281**, 7309–7316 (2006).

27. Bernstein, L. H. & Everse, J. Studies on the mechanism of the malate dehydrogenase reaction. *J. Biol. Chem.* **253**, 8702–8707 (1978).

28. Hurd, R. E., Yen, Y.-F., Chen, A. & Ardenkjaer-Larsen, J. H. Hyperpolarized ^{13} C metabolic imaging using dissolution dynamic nuclear polarization. *J. Magn. Reson. Imaging* **36**, 1314–1328 (2012).

29. Wan, J. C. M. *et al.* Liquid biopsies come of age: Towards implementation of circulating tumour DNA. *Nat. Rev. Cancer* **17**, 223–238 (2017).

30. Diaz, L. A. & Bardelli, A. Liquid biopsies: Genotyping circulating tumor DNA. *J. Clin. Oncol.* **32**, 579–586 (2014).

31. Brender, J. R. *et al.* Dynamic Imaging of Glucose and Lactate Metabolism by 13 C-MRS without Hyperpolarization. *Sci. Rep.* **9**, 1–14 (2019).

32. Wenkebach, T. *Essentials of Dynamic Nuclear Polarization*. (Spindrift Publications, 2016).

33. Overhauser, A. W. Polarization of Nuclei in Metals. *Phys. Rev.* **92**, 411–415 (1953).

34. Carver, T. R. & Slichter, C. P. Polarization of nuclear spins in metals. *Phys. Rev.* **92**, 212–213 (1953).

35. Comment, A. *et al.* Design and performance of a DNP prepolarizer coupled to a rodent MRI scanner. *Concepts Magn. Reson. Part B Magn. Reson. Eng.* **31**, 255–269 (2007).

36. Bornet, A. *et al.* Boosting dissolution dynamic nuclear polarization by cross polarization. *J. Phys. Chem. Lett.* **4**, 111–114 (2013).

37. Marco-Rius, I. *et al.* Photogenerated Radical in Phenylglyoxylic Acid for in Vivo Hyperpolarized 13C MR with Photosensitive Metabolic Substrates. *Journal of the American Chemical Society* **140**, 14455–14463 (2018).

38. Hovav, Y., Feintuch, A. & Vega, S. Theoretical aspects of dynamic nuclear polarization in the solid state - The cross effect. *J. Magn. Reson.* **214**, 29–41 (2012).

39. Hovav, Y. *et al.* Effects of the electron polarization on Dynamic Nuclear Polarization in Solids. *Phys. Chem. Chem. Phys.* **17**, 6053–6065 (2015).

40. Karabanov, A. *et al.* Dynamic nuclear polarisation by thermal mixing: Quantum theory and macroscopic simulations. *Phys. Chem. Chem. Phys.* **18**, 30093–30104 (2016).

41. Hovav, Y., Feintuch, A. & Vega, S. Theoretical aspects of dynamic nuclear polarization in the solid state - The solid effect. *J. Magn. Reson.* **207**, 176–189 (2010).

42. Tan, K. O., Mardini, M., Yang, C., Ardenkjær-Larsen, J. H. & Griffin, R. G. Three-spin solid effect and the spin diffusion barrier in amorphous solids. *Sci. Adv.* **5**, eaax2743 (2019).

43. Ardenkjær-Larsen, J. H. *et al.* Cryogen-free dissolution dynamic nuclear polarization polarizer operating at 3.35 T, 6.70 T, and 10.1 T. *Magn. Reson. Med.* **81**, 2184–2194 (2019).

44. Brindle, K. M. Imaging Metabolism with Hyperpolarized 13C-Labeled Cell Substrates. *J. Am. Chem. Soc.* **137**, 6418–6427 (2015).

45. Tannús, A. & Garwood, M. Adiabatic pulses. *NMR Biomed.* **10**, 423–434 (1997).

46. Garwood, M. & DelaBarre, L. The return of the frequency sweep: designing adiabatic pulses for contemporary NMR. *J. Magn. Reson.* **153**, 155–177 (2001).

47. Garwood, M. & Ke, Y. Symmetric pulses to induce arbitrary flip angles with compensation for rf inhomogeneity and resonance offsets. *J. Magn. Reson.* **94**, 511–525 (1991).

48. Bernstein, M., King, K. & Zhou, X. *Handbook of MRI pulse sequences*. (Elsevier Academic Press, 2004).

49. Meyer, C. H., Pauly, J. M., Macovski, A. & Nishimura, D. G. Simultaneous Spatial and Spectral Selective Excitation. *Magn. Reson. Med.* **15**, 287–304 (1990).

50. Larson, P. E. Z. *et al.* Multiband excitation pulses for hyperpolarized 13C dynamic chemical-shift imaging. *J. Magn. Reson.* **194**, 121–127 (2008).

51. Marco-Rius, I. *et al.* Multiband spectral-spatial RF excitation for hyperpolarized [2-13C]dihydroxyacetone 13C-MR metabolism studies. *Magn. Reson. Med.* **77**, 1419–1428 (2017).

52. Hahn, E. Spin Echoes. *Phys. Rev.* **80**, 580–594 (1950).

53. Keeler, J. *Understanding NMR spectroscopy*. (John Wiley & Sons, 2002).

54. Barklie, R., Collins, M. & Silva, S. EPR linewidth variation, spin relaxation times, and exchange in amorphous hydrogenated carbon. *Phys. Rev. B - Condens. Matter Mater. Phys.* **61**, 3546–3554 (2000).

55. Bloch, F. Nuclear Induction. *Phys. Rev.* **70**, 460–474 (1946).

56. Brown, R. W., Cheng, Y.-C. N., Haacke, E. M., Thompson, M. R. & Venkatesan, R. *Magnetic Resonance Imaging - Physical Principles and Sequence Design*. (Willey, 2014).

57. Ernst, R. R. & Anderson, W. A. Application of fourier transform spectroscopy to magnetic resonance. *Rev. Sci. Instrum.* **37**, 93–102 (1966).

58. Callaghan, P. T. *Principles of Nuclear Magnetic Resonance Microscopy*. (Oxford University Press, 1993).

59. Chen, A. P. *et al.* Feasibility of using hyperpolarized [1-13C]lactate as a substrate for in vivo metabolic 13C MRSI studies. *Magn. Reson. Imaging* **26**, 721–726 (2008).

60. Frahm, J. *et al.* Localized proton NMR spectroscopy in different regions of the human brain in vivo. Relaxation times and concentrations of cerebral metabolites. *Magn. Reson. Med.* **11**, 47–63 (1989).

61. Wang, J. F., Falke, J. J. & Chan, S. I. A proton NMR study of the mechanism of the erythrocyte glucose transporter. *Proc. Natl. Acad. Sci.* **83**, 3277–3281 (1986).

62. Levitt, M. H. *Spin Dynamics: Basics of Nuclear Magnetic Resonance*. (Wiley, 2001).

63. Spielman, D. In Vivo MR: Relaxation Theory and Contrast Mechanisms. (2019). Available at: https://web.stanford.edu/class/rad226b/index.html.

64. Gerlach, W. & Stern, O. Der experimentelle Nachweis der Richtungsquantelung im Magnetfeld. *Zeitschrift für Phys.* **9**, 349–352 (1922).

65. Smith, S., Palke, W. & Gerig, J. The Hamiltonians of NMR: Part II. *Concepts Magn. Reson.* **4**, 181–204 (1992).

66. Redfield, A. On the Theory of Relaxation Processes. *IBM J. Res. Dev.* **1**, 19–31 (1957).

67. Goldman, M. Formal Theory of Spin-Lattice Relaxation. *J. Magn. Reson.* **149**, 160–87 (2001).

68. Bengs, C. & Levitt, M. H. SpinDynamica: Symbolic and numerical magnetic resonance in a Mathematica environment. *Magn. Reson. Chem.* **56**, 374–414 (2018).

69. Hoult, D. I. & Lauterbur, P. C. The sensitivity of the zeugmatographic experiment involving human samples. *J. Magn. Reson.* **34**, 425–433 (1979).

70. Pfeuffer, J., Tkác, I., Provencher, S. W. & Gruetter, R. Toward an in vivo neurochemical profile: quantification of 18 metabolites in short-echo-time (1)H NMR spectra of the rat brain. *J. Magn. Reson.* **141**, 104–120 (1999).

71. Howe, F. a *et al.* Metabolic profiles of human brain tumors using quantitative in vivo 1H magnetic resonance spectroscopy. *Magn. Reson. Med.* **49**, 223–232 (2003).

72. McCarney, E. R., Armstrong, B. D., Lingwood, M. D. & Han, S. Hyperpolarized water as an authentic magnetic resonance imaging contrast agent. *Proc. Natl. Acad. Sci.* **104**, 1754–1759 (2007).

73. Lingwood, M. D. *et al.* Hyperpolarized Water as an MR Imaging Contrast Agent: Feasibility of in Vivo Imaging in a Rat Model. *Radiology* **265**, 418–425 (2012).

74. de Graaf, R. A. *et al.* High magnetic field water and metabolite proton T1 and T2 relaxation in rat brain in vivo. *Magn. Reson. Med.* **56**, 386–394 (2006).

75. Morris, G. A. & Freeman, R. Enhancement of Nuclear Magnetic Resonance Signals by Polarization Transfer. *J. Am. Chem. Soc.* **233**, 760–762 (1979).

76. Mishkovsky, M., Cheng, T., Comment, A. & Gruetter, R. Localized in vivo hyperpolarization transfer sequences. *Magn. Reson. Med.* **68**, 349–352 (2012).

77. Harris, T., Giraudeau, P. & Frydman, L. Kinetics from indirectly detected hyperpolarized NMR spectroscopy by using spatially selective coherence transfers. *Chem. - A Eur. J.* **17**, 697–703 (2011).

78. Sarkar, R. *et al.* Proton NMR of 15N-Choline Metabolites Enhanced by Dynamic Nuclear Polarization. *J. Am. Chem. Soc.* **131**, 16014–16015 (2009).

79. Chekmenev, E. Y., Norton, V. A., Weitekamp, D. P. & Bhattacharya, P. Hyperpolarized 1H NMR employing low γ nucleus for spin polarization storage. *J. Am. Chem. Soc.* **131**, 3164–3165 (2009).

80. Bowers, C. R. & Weitekamp, D. P. Parahydrogen and synthesis allow dramatically enhanced nuclear alignment. *J. Am. Chem. Soc.* **109**, 5541–5542 (1987).

81. Bowers, C. R. & Weitekamp, D. P. Transformation of symmetrization order to nuclear-spin magnetization by chemical reaction and nuclear magnetic resonance. *Phys. Rev. Lett.* **57**, 2645–2648 (1986).

82. Dzien, P. *et al.* Following Metabolism in Living Microorganisms by Hyperpolarized 1 H NMR. *J. Am. Chem. Soc.* **138**, 12278–12286 (2016).

83. Kettunen, M. I., Kennedy, B. W. C., Hu, D.-E. & Brindle, K. M. Spin echo measurements of the extravasation and tumor cell uptake of hyperpolarized [1-(13) C]lactate and [1-(13) C]pyruvate. *Magn. Reson. Med.* **70**, 1200–9 (2013).

84. Wijnen, J. P. *et al.* Detection of lactate in the striatum without contamination of macromolecules by J-difference editing MRS at 7T. *NMR Biomed.* **28**, 514–522 (2015).

85. Madan, A. *et al.* Proton T2 measurement and quantification of lactate in brain tumors by MRS at 3 Tesla in vivo. *Magn. Reson. Med.* **73**, 2094–2099 (2015).

86. Luo, Y. *et al.* In vivo observation of lactate methyl proton magnetization transfer in rat C6 glioma. *Magn. Reson. Med.* **41**, 676–685 (1999).

87. Schulte, R. F. *et al.* Saturation-recovery metabolic-exchange rate imaging with hyperpolarized [1-13C] pyruvate using spectral-spatial excitation. *Magn. Reson. Med.* **69**, 1209–1216 (2013).

88. Hill, D. K. *et al.* Model Free Approach to Kinetic Analysis of Real-Time Hyperpolarized 13C Magnetic Resonance Spectroscopy Data. *PLoS One* **8**, 1–9 (2013).

89. Daniels, C. J. *et al.* A comparison of quantitative methods for clinical imaging with hyperpolarized 13C-pyruvate. *NMR Biomed.* **29**, 387–399 (2016).

90. Wang, J. *et al.* Dynamic 1H imaging of hyperpolarized [1-13C]lactate in vivo using a reverse INEPT experiment. *Magn. Reson. Med.* **70**, 741–747 (2018).

91. von Morze, C. *et al.* In vivo hyperpolarization transfer in a clinical MRI scanner. *Magn. Reson. Med.* **80**, 480–487 (2018).

92. Mispelter, J., Lupu, M. & Briguet, A. *NMR Probeheads for Biophysical and Biomedical Experiments: Theoretical Principles & Practical Guidelines*. (Imperial College Press, 2015).

93. Gruber, B., Froeling, M., Leiner, T. & Klomp, D. W. J. RF coils: A practical guide for nonphysicists. *J. Magn. Reson. Imaging* **48**, 590–604 (2018).

94. Murphy-Boesch, J. & Koretsky, A. P. An in Vivo NMR probe circuit for improved sensitivity. *J. Magn. Reson.* **54**, 526–532 (1983).

95. Fujita, H., Zheng, T., Yang, X., Finnerty, M. J. & Handa, S. RF surface receive array coils: The art of an LC circuit. *J. Magn. Reson. Imaging* **38**, 12–25 (2013).

96. Kumar, A., Edelstein, W. A. & Bottomley, P. A. Noise figure limits for circular loop MR coils. *Magn. Reson. Med.* **61**, 1201–1209 (2009).

97. Adriany, G. & Gruetter, R. A half-volume coil for efficient proton decoupling in humans at 4 tesla. *J. Magn. Reson.* **125**, 178–84 (1997).

98. Shen, J. *et al.* Determination of the rate of the glutamate/glutamine cycle in the human brain by in vivo 13C NMR. *Proc. Natl. Acad. Sci. U. S. A.* **96**, 8235–40 (1999).

99. Ross, B., Lin, A., Harris, K., Bhattacharya, P. & Schweinsburg, B. Clinical experience with 13C MRSi n vivo. *NMR Biomed.* **16**, 358–369 (2003).

100. Gruetter, R., Seaquist, E. R., Kim, S. & Uğurbil, K. Localized in vivo 13C-NMR of Glutamate Metabolism in the Human Brain: Initial Results at 4 Tesla. *Dev. Neurosci.* **20**, 380–388 (1998).

101. Wetterling, F. *et al.* The design of a double-tuned two-port surface resonator and its application to in vivo Hydrogen- and Sodium-MRI. *J. Magn. Reson.* **217**, 10–18 (2012).

102. Hesketh, R. L. & Brindle, K. M. Magnetic resonance imaging of cancer metabolism with hyperpolarized 13C-labeled cell metabolites. *Curr. Opin. Chem. Biol.* **45**, 187–194 (2018).

103. Harris, T. *et al.* Long-lived 15N Hyperpolarization and Rapid Relaxation as a Potential Basis for Repeated First Pass Perfusion Imaging - Marked Effects of Deuteration and Temperature. *ChemPhysChem* **32**, 60–73 (2018).

104. Durst, M. *et al.* α-trideuteromethyl[15N]glutamine: A long-lived hyperpolarized perfusion marker. *Magn. Reson. Med.* **76**, 1900–1904 (2016).

105. Jiang, W. *et al.* Hyperpolarized15N-pyridine Derivatives as pH-Sensitive MRI Agents. *Sci. Rep.* **5**, 1–6 (2015).

106. Truong, M. L., Coffey, A. M., Shchepin, R. V., Waddell, K. W. & Chekmenev, E. Y. Sub-second proton imaging of 13C hyperpolarized contrast agents in water. *Contrast Media Mol. Imaging* **9**, 333–341 (2014).

107. Barb, A. W., Hekmatyar, S. K., Glushka, J. N. & Prestegard, J. H. Exchange facilitated indirect detection of hyperpolarized 15ND 2-amido-glutamine. *J. Magn. Reson.* **212**, 304–310 (2011).

108. Horská, A. & Spencer, G. S. Correctly accounting for radiofrequency spillover in saturation transfer experiments: application to measurement of the creatine kinase reaction rate in human forearm muscle. *MAGMA* **5**, 159–63 (1997).

109. Merkle, H., Wei, H., Garwood, M. & Uğurbil, K. B1-insensitive heteronuclear adiabatic polarization transfer for signal enhancement. *J. Magn. Reson.* **99**, 480–494 (1992).

110. Norton, V. A. & Weitekamp, D. P. Communication: Partial polarization transfer for single-scan spectroscopy and imaging. *J. Chem. Phys.* **135**, (2011).

111. Levitt, M. H. The Signs of Frequencies and Phases in NMR. *J. Magn. Reson.* **126**, 164–182 (1997).

112. Vold, R. L., Daniel, E. S. & Chan, S. O. Magnetic Resonance Measurements of Proton Exchange in Aqueous Urea. *J. Am. Chem. Soc.* **92**, 6771–6776 (1970).

113. Golman, K., Ardenkjaer-Larsen, J. H., Petersson, J. S., Mansson, S. & Leunbach, I. Molecular imaging with endogenous substances. *Proc. Natl. Acad. Sci.* **100**, 10435–10439 (2003).

114. Zeng, H. *et al.* 15N Heteronuclear Chemical Exchange Saturation Transfer MRI. *J. Am. Chem. Soc.* **138**, 11136–11139 (2016).

115. Haase, A., Frahm, J., Matthaei, D., Hanicke, W. & Merboldt, K. D. FLASH imaging. Rapid NMR imaging using low flip-angle pulses. *J. Magn. Reson.* **67**, 258–266 (1986).

116. Marjańska, M. *et al.* In vivo 13C spectroscopy in the rat brain using hyperpolarized [1-13C]pyruvate and [2-13C]pyruvate. *J. Magn. Reson.* **206**, 210–218 (2010).

117. Hu, S. *et al.* Use of hyperpolarized [1-13C]pyruvate and [2-13C]pyruvate to probe the effects of the anticancer agent dichloroacetate on mitochondrial metabolism in vivo in the normal rat. *Magn. Reson. Imaging* **30**, 1367–1372 (2012).

118. Park, J. M. *et al.* Measuring mitochondrial metabolism in rat brain in vivo using MR Spectroscopy of hyperpolarized [2-13C]pyruvate. *NMR Biomed.* **26**, 1197–1203 (2013).

119. Park, J. M. *et al.* Volumetric spiral chemical shift imaging of hyperpolarized [2-13C]pyruvate in a rat C6 glioma model. *Magn. Reson. Med.* **75**, 973–984 (2016).

120. Chung, B. T. *et al.* First Hyperpolarized [2-13C]Pyruvate MR Studies of Human Brain Metabolism. in *Proceedings of the 27th Annual Meeting of ISMRM* #0724 (2019).

121. Kreis, F., Wang, J., Wright, A. & Brindle, K. Measuring lactate dehydrogenase activity with proton detected 13C hyperpolarization. in *Proceedings of the 25th Annual Meeting*

of ISMRM #2941 (2017).

122. Tkáč, I., Starčuk, Z., Choi, I. Y. & Gruetter, R. In Vivo 1H NMR Spectroscopy of Rat Brain at 1 ms Echo Time. *Magn. Reson. Med.* **41**, 649–656 (1999).

123. Lu, M., Zhu, X.-H., Zhang, Y., Mateescu, G. & Chen, W. Quantitative assessment of brain glucose metabolic rates using in vivo deuterium magnetic resonance spectroscopy. *J. Cereb. Blood Flow Metab.* **37**, 3518–3530 (2017).

124. Gambhir, S. S. Molecular imaging of cancer with positron emission tomography. *Nat. Rev. Cancer* **2**, 683–693 (2002).

125. James, M. L. & Gambhir, S. S. A Molecular Imaging Primer: Modalities, Imaging Agents, and Applications. *Physiol. Rev.* **92**, 897–965 (2012).

126. Wahl, R. L., Jacene, H., Kasamon, Y. & Lodge, M. A. From RECIST to PERCIST: Evolving Considerations for PET Response Criteria in Solid Tumors. *J. Nucl. Med.* **50**, 122S-150S (2009).

127. Albers, M. J. *et al.* Hyperpolarized 13C lactate, pyruvate, and alanine: Noninvasive biomarkers for prostate cancer detection and grading. *Cancer Res.* **68**, 8607–8615 (2008).

128. Witney, T. H., Kettunen, M. I. & Brindle, K. M. Kinetic modeling of hyperpolarized 13C label exchange between pyruvate and lactate in tumor cells. *J. Biol. Chem.* **286**, 24572–24580 (2011).

129. Choi, I.-Y. & Gruetter, R. *Neural metabolism in vivo*. (Springer New York Dordrecht Heidelberg London, 2012).

130. Purvis, L. A. B. *et al.* OXSA: An open-source magnetic resonance spectroscopy analysis toolbox in MATLAB. *PLoS One* **12**, 1–10 (2017).

131. Stobbe, R. & Beaulieu, C. Advantage of sampling density weighted apodization over postacquisition filtering apodization for sodium MRI of the human brain. *Magn. Reson. Med.* **60**, 981–986 (2008).

132. Bader, B. W. & Kolda, T. G. Efficient MATLAB Computations with Sparse and Factored Tensors. *SIAM J. Sci. Comput.* **30**, 205–231 (2007).

133. Bader, B. W. & Kolda, T. G. MATLAB Tensor Toolbox Version 3.0-dev. (2017).

134. Rivenzon-Segal, D., Margalit, R. & Degani, H. Glycolysis as a metabolic marker in orthotopic breast cancer, monitored by in vivo 13 C MRS. *Am. J. Physiol. - Endocrinol. Metab.* **283**, E623–E630 (2002).

135. Rees, W. D. & Gliemann, J. A kinetic analysis of hexose transport in cultured human lymphocytes (IM-9). *BBA - Biomembr.* **812**, 98–106 (1985).

136. Fink, R. I., Wallace, P., Brechtel, G. & Olefsky, J. M. Evidence that glucose transport is rate-limiting for in vivo glucose uptake. *Metabolism* **41**, 897–902 (1992).

137. Ben-Yoseph, O., Kingsley, P. B. & Ross, B. D. Metabolic loss of deuterium from isotopically labeled glucose. *Magn. Reson. Med.* **32**, 405–409 (1994).

138. Aguayo, J. B., McLennan, I. J., Graham, C. & Cheng, H. M. Dynamic monitoring of corneal carbohydrate metabolism using high-resolution deuterium NMR spectroscopy. *Exp. Eye Res.* **47**, 337–343 (1988).

139. Michelakis, E. D., Webster, L. & Mackey, J. R. Dichloroacetate (DCA) as a potential metabolic-targeting therapy for cancer. *Br. J. Cancer* **99**, 989–994 (2008).

140. Hull, F. E. & Whereat, A. F. The effect of rotenone on the regulation of fatty acid synthesis in heart mitochondria. *J. Biol. Chem.* **242**, 4023–4028 (1967).

141. Kallinowski, F. *et al.* Glucose uptake, lactate release, ketone body turnover, metabolic micromilieu, and pH distributions in human breast cancer xenografts in nude rats. *Cancer Res* **48**, 7264–7272 (1988).

142. Reitzer, L. J., Wice, B. M. & Kennel, D. Evidence that glutamine, Not Sugar, Is the Major Energy Source for Cultured HeLa Cells. *J. Biol. Chem.* **254**, 2669–2676 (1979).

143. Post, J. F. M., Baum, E. & Ezell, E. L. 13C NMR studies of glucose metabolism in human leukemic CEM-C7 and CEM-C1 cells. *Magn. Reson. Med.* **23**, 356–366 (1992).

144. Borowiak, R. *et al.* Initial investigation of glucose metabolism in mouse brain using enriched 17O-glucose and dynamic 17O-MRS. *NMR Biomed.* **30**, 1–10 (2017).

145. Maher, E. A. *et al.* Metabolism of [U-13C]glucose in human brain tumors in vivo. *NMR Biomed.* **25**, 1234–1244 (2012).

146. Marin-Valencia, I. *et al.* Analysis of tumor metabolism reveals mitochondrial glucose oxidation in genetically diverse human glioblastomas in the mouse brain in vivo. *Cell Metab.* **15**, 827–837 (2012).

147. Herst, P. M. & Berridge, M. V. Cell surface oxygen consumption: A major contributor to cellular oxygen consumption in glycolytic cancer cell lines. *Biochim. Biophys. Acta - Bioenerg.* **1767**, 170–177 (2007).

148. Vlashi, E. *et al.* Metabolic state of glioma stem cells and nontumorigenic cells. *Proc. Natl. Acad. Sci.* **108**, 16062–16067 (2011).

149. Timm, K. N. *et al.* Hyperpolarized [U-2H, U-13C]Glucose reports on glycolytic and pentose phosphate pathway activity in EL4 tumors and glycolytic activity in yeast cells. *Magn. Reson. Med.* **1547**, 1543–1547 (2015).

150. Darrasse, L. & Ginefri, J. C. Perspectives with cryogenic RF probes in biomedical MRI. *Biochimie* **85**, 915–937 (2003).

151. Sanchez-Heredia, J. D. *et al.* Low-Noise Active Decoupling Circuit and its Application to 13 C Cryogenic RF Coils at 3 T. *Tomography* **3**, 60–66 (2017).

152. De Feyter, H. M. *et al.* Deuterium Metabolic Imaging (DMI) of glucose metabolism in patients with brain tumors. in *Proceedings of the 27th Annual Meeting of ISMRM* #0859 (2019).

153. de Graaf, R. A. *et al.* On the magnetic field dependence of deuterium metabolic imaging (DMI). in *Proceedings of the 27th Annual Meeting of ISMRM* #0492 (2019).

154. Kishimoto, S. *et al.* Distinguishing Closely Related Pancreatic Cancer Subtypes In Vivo by 13C Glucose MRI without Hyperpolarization. *bioRxiv [Preprint]* (2019). doi:http://dx.doi.org/10.1101/511543

155. Kato, T. *et al.* Metabolic assessment of gliomas using 11C-methionine, [18F] fluorodeoxyglucose, and 11C-choline positron-emission tomography. *Am. J. Neuroradiol.* **29**, 1176–1182 (2008).

156. Pauleit, D. *et al.* Comparison of 18F-FET and 18F-FDG PET in brain tumors. *Nucl. Med. Biol.* **36**, 779–787 (2009).

157. Medical Research Council. *MRC Review of Positron Emission Tomography (PET) within The Medical Imaging Research Landscape*. (2017).

158. Saha, G. B. Design and Cost of PET Center. in *Basics of PET Imaging* 227–239 (Springer, 2015).